8-2019

Effect of Microstructure on Corrosion of Structural and Advanced Alloys

Seyedhamidreza Torbatisarraf
Clemson University

EFFECT OF MICROSTRUCTURE ON CORROSION OF STRUCTURAL AND ADVANCED ALLOYS

A Dissertation
Presented to
the Graduate School of
Clemson University

In Partial Fulfillment
of the Requirements for the Degree
Doctor of Philosophy
Civil Engineering

---

by
Seyedhamidreza Torbatisarraf
August 2019

Accepted by:
Prof. Amir Poursaee, Committee Chair
Prof. Prasad Rangaraju
Prof. Marian S. Kennedy
Prof. Brandon Ross

ABSTRACT

Corrosion science combines the ability to characterize the composition and structure in atomic scale with the experimental and/or computational modeling to enable technological solutions and service life predictions. However, lack of observations restricts the simulation and service life estimations for all alloys. This dissertation work aims to provide literature, observations and discussion on the influence of microstructure on corrosion of both structural (carbon steel) and advanced alloys (ZK60, a Mg based alloy, and AA6061, a Al based alloy) in range of saline solutions. The solutions were chosen to simulate actual envinment of alloys application.

Based on the relevant research area in department of civil enginieering on degradation of cementitious material and embded steel in concrete, the main focus was the corrosion and passivation of reinforcing carbon steel bars in alkaline solution simulating concrete environment. Scanning electrochemical microscopy was exploited to characterize the kinetics of formation of a passive film and the electrochemical activity of the carbon steel in simulated concrete pore solution. The effect of coupling this carbon steel was also studied and probability of galvanic corrosion was examined. The microstructure and distrobutiona of ferrite and pearlite in the carbon steel was altered, using different heat-treatment procedures, and then the susceptibility to corrosion and chloride threshold values of these steels were evaluated. Post corrosion and electrochemical data revealed that restricting and refining pearlite phase improved corrosion performance of regular reinforcing steel bars in chloride contaminated concrete environment. In addition, the surface microstructure of steel was refined through surface

mechanical attrition, i.e. sand blasting. It was found that the dissolution rate of the refined surface was highly dependent on the pH of the environment. Grain refinement provided high defective and energetic zones which preferentially oxidized. Consequently, depending on the environment, the corrosion resistance was improved or exacerbated if the formed oxide component was protective or defective, respectively.

Furthermore, the influence of manufacturing process, and subsequently the microstructure on the corrosion activity of two different alloys, i.e. ZK60 (Mg based alloy) and AA6061 (Al based alloy) were also investigated. Results indicated that uniform microstructure reduced corrosion rate due to formation of integrated and uniform protective oxide film and decreasing galvanic corrosion along the surface.

DEDICATION

To my parents and my brother

for their unconditional love.

ACKNOWLEDGMENTS

Technical guidance came from many people during my Ph.D. program. First, I wish to sincerely thank to my advisor, Dr. Amir Poursaee, for his excellent support, invaluable scientific feedback and insights, and constructive guidance. In addition, I would also like to thank my committee members, Dr. Marian Kennedy, Dr. Prasad Rangaraju and Dr. Brandon Ross, for their time to review my work and their critiques that helped improved my research results. Finally, I need to also express my deepest gratitude for collaboration with Professor Terence G. Langdon and my brother Dr. Alireza Torbatisarraf from University of Southern California.

In addition to faculty, I need to highlight support from staff and colleagues. Danny Metz, a staff member at the Clemson Glenn Department of Civil Engineering, provided technical technical support in my experimental research. In addition, I need to thank my my friends, Ling Ding, Mitra Shabani, Iman Khakpour, Saeid Kieh and Younes Moghanlou who were always kind and helped me during my program.

The major part of this dissertation was based upon work supported by the National Science Foundation (NSF) under Grant No. 1552794, entitled: EAGER: Corrosion Reduction in Reinforcing Steel of Concrete Structures through Grain Size Alteration. I would like to acknowledge mentioned foundation and all corresponded committee who supported us financially.

TABLE OF CONTENTS

Page

Table of Contents (Continued) Page

Table of Contents (Continued) Page

LIST OF TABLES

Table Page

LIST OF FIGURES

Figure Page

CHAPTER 1

INTRODUCTION

Corrosion is a complex and broad subject that is defined as “environmentally induced degradation of a material that involves a chemical reactions” [1]. Published literature currently encompasses a wide spectrum of environments, temperature, metals, alloys, composites and ceramics [2–4]. However, as the complexity and diversity of materials systems continues to increase, there is a need for additional research and sharing data[5].

Premature material degradation due to corrosion in industrialized economies costs approximately 3% of their gross domestic product (GDP) [6]. Figure 1-1, as an example, shows a comparison of the corrosion costs the healthcare direct costs and the costs due to weather and climate disasters [7]. While healthcare and weather disasters are well recognized as major societal challenges and frequently appear in the media, the tremendous economic impact by corrosion receives little attention. In addition, the continuous aging of infrastructures, will exacerbate this situation in the upcoming years. For instance, the age profile of reinforced concrete infrastructures in U.S. shows a peak in construction activities around 1960–1980. Thus, most of the bridges have are 40 or more years old and they were designed for a service life of 50 years. Consequently, in the upcoming decades corrosion costs will be steeply increased resulting from number of bridges beyond their designed life [8].

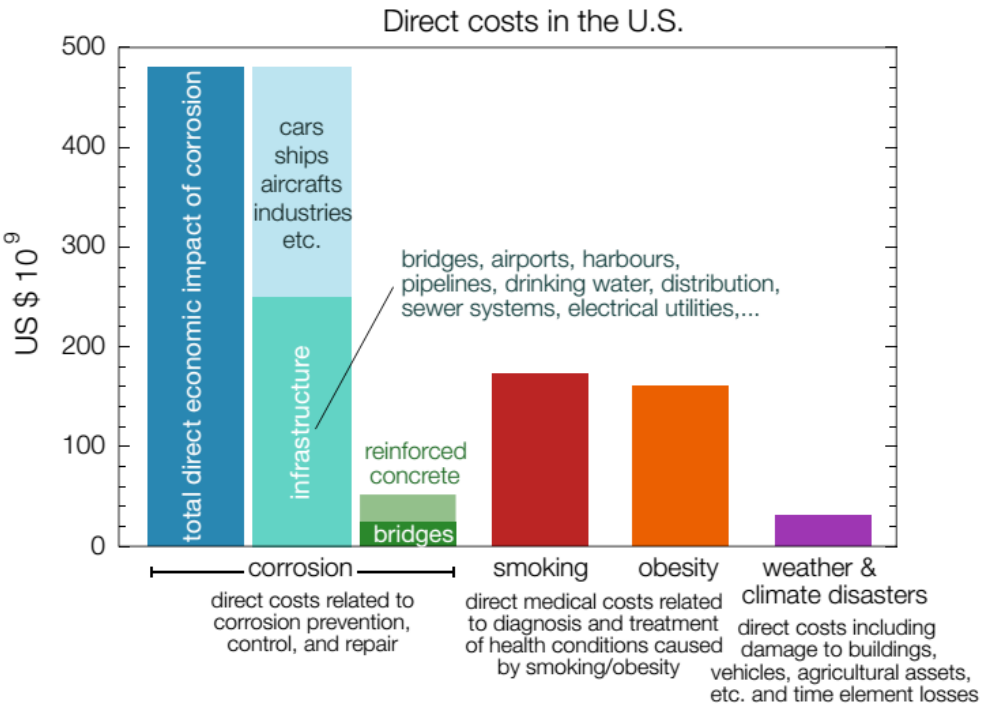

Figure 1-1. Economic impact of corrosion compared to direct medical costs and health issues in the U.S. [7]. *Reprinted without permission.*

However, the real cost of corrosion is even more pervasive for society. National Research Council (NRC) report described less measurable impacts on corrosion such as loss of readiness, that is, the ability of a system to respond to emergencies or situations involving national security [9]. For example, while the costs of replacing deteriorating bridges, as an infrastructure, can be estimated, but the impacts of corrosion on national productivity and security due to failures and traffic congestion during repairs is not well-estimated.

The influence of corrosion on environment, public health, and global sustainability cannot be quantified simply in terms GDP [1]. Figure 1-2 shows the NRC

assessment of the impact of corrosion on many aspects of society. Some examples, leaching of corrosion products and seeping of contaminant due to dissolution of metals or leakage of reservoir into the environment, deterioration of medical devices and implants due to interactions with human body environment, and the weakening of the nation's energy and transportation infrastructures.

Figure 1-2. Impact of corrosion on aspect of society. In many of these areas [9]. *Reprinted without permission.*

Hierarchy of corrosion challenges

Materials design for corrosion resistance relies on knowledge and improvements of well-stablishd compositions and structures. Furthermore, progress in atomic scale science and the ability to synthesize and control precise atomic structures, create new opportunities and challenges for corrosion scientists. The most effective way to reduce

corrosion is to find underlying corrosion mechanisms. For example, passivation and depassivation due to pH changes or ingress of chloride ion [10–12], formation of mirco [13] or macro galvanic cell [14]. This alone would justify increased attention to the science base of corrosion research. While some forms of corrosion are well understood at the macro level, complex interactions among the different forms are yet needed to be fully investigated. There is relatively poor understanding on corrosion mechanisms, at the micro/nano level. Lack of fundamental knowledge in this field of study is directly reflected in the high cost of corrosion.

NRC report prioritized the future challenges for corrosion science as being [1]:

I: “Development of cost-effective, environment-friendly, corrosion resistant materials or coatings”;

II: “High-fidelity modeling for the prediction of corrosion degradation in actual service environments”;

III: “Accelerated corrosion testing under controlled laboratory conditions that quantitatively correlates with the long-term behavior observed in service environments”; and

IV: “Accurate forecasting of remaining service time until major repair, replacement, or overhaul becomes necessary”.

These hierarchies are deemed to be the drivers and guiding principles of the framework for prioritizing efforts in corrosion science in decades to come. To address these challenges, the mechanism of corrosion, and the detailed influence of the

metal/alloy microstructure on corrosion should be understand and defined. Corrosion science is an interdisciplinary field of study including different aspects of physics, materials science, surface science, electrochemistry and fracture mechanics. As shown on Figure 1-3, many corrosion processes are now known to be controlled by molecular, sub micrometer, and micrometer-scale phenomena.

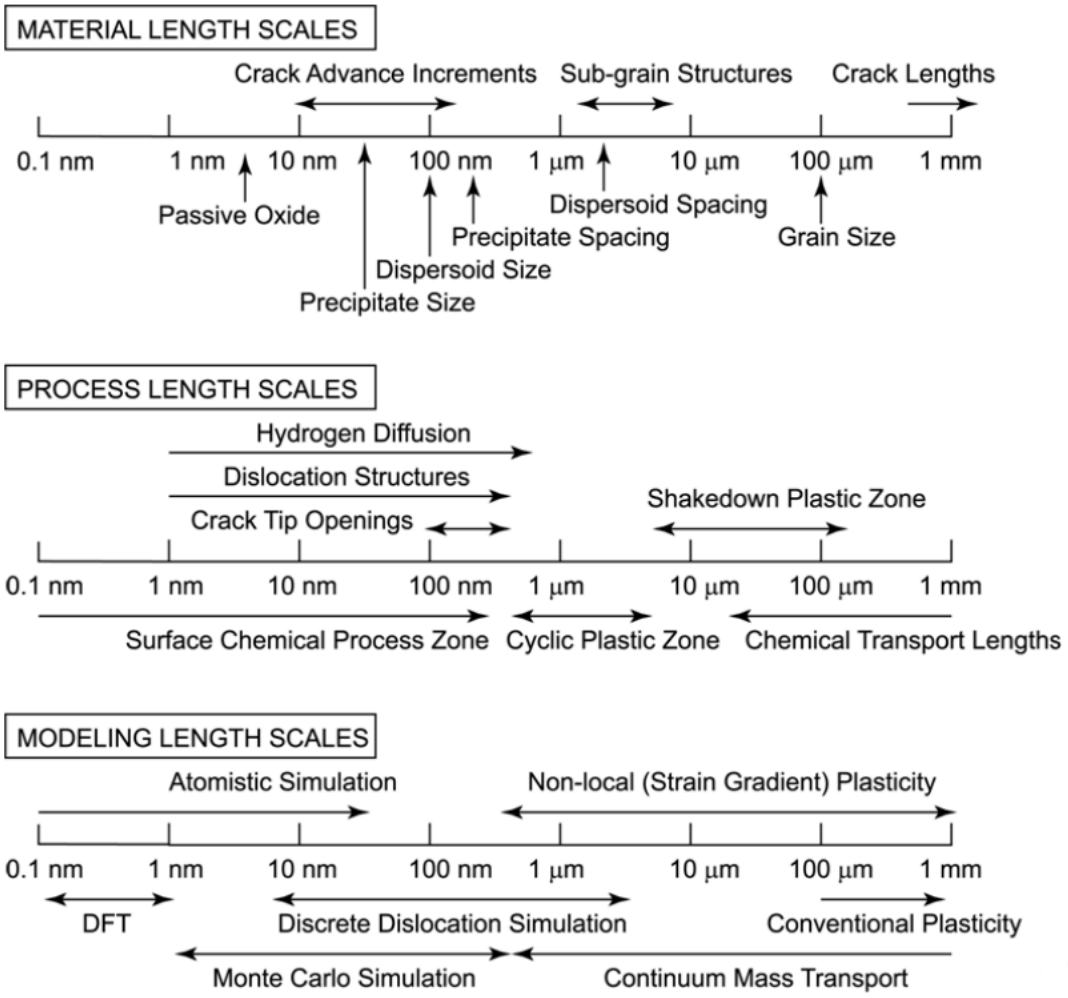

Figure 1-3. The wide span of different length scales of material, the processes, and the models needed to correctly predict corrosion degradation [1]. Reprinted without permission.

Accordingly, progress in this field, requires multi-scale studies to understand how

networks of boundaries and arrays of defects behave under corrosive conditions [1]. Nonetheless, there is a lack of micrometric-scale understanding of the role of various specific chemical species, phases, defects, grain boundaries, etc. in the initiation and propagation of corrosion processes.

Objectives and Organization of the Dissertation

The main objective of all experiements carried out in this disseration to investigate the influence of microstructure on the corrosion activity of alloys. The focus, however, was the corrosion and passivation of reinforcement carbon steel in alkaline solution to simulate concrete environment. In Chapter 2, a criterion for passivation time of steel in simulated concrete pore solution were determined using a novel micro electrochemical technique. This technique provides a novel practical method to study corrosion and related electrochemical phenomena in micro-scale and leads further investigations in future. In Chapter 3, microstructures were changed through heat treatment, and surface nanocrystalization and the consequent corrosion performance were studied. Furthermore, the influence of manufacturing process, and subsequently the microstructure on the corrosion activity of three different systems, i.e. thermomechanically treated (TMT) reinforcement steel, ZK60 (Mg based alloy) and AA6061 (Al based alloy) were also investigated. Literature review of each alloy system, details of the experimental procedures and results are provided and discussed in these chapters.

References

[1] D. Duquette, R. Schafrik, A. Asphahani, G. Bierwagen, D. Butt, G. Grankel, R. Newman, L. Schwartz, J. Scully, P. Tortorreli, D. Trejo, D. Untereker, M. U-Macdonald, Research Opportunities in Corrosion Science and Engineering, The National Academies Press, Washington, DC, 2011.

[2] E. McCafferty, Introduction to corrosion science, 2010.

[3] S. Rashidi, J.P. Choi, J.W. Stevenson, A. Pandey, Effect of Aluminizing on the High-Temperature Oxidation Behavior of an Alumina-Forming Austenitic Stainless Steel, JOM. (2018).

[4] A. Keyvani, M. Saremi, M.H. Sohi, An investigation on oxidation, hot corrosion and mechanical properties of plasma-sprayed conventional and nanostructured YSZ coatings, Surf. Coatings Technol. 206 (2011) 208–216.

[5] X. Li, D. Zhang, Z. Liu, C. Du, C. Dong, Share corrosion data, (2015) 6–7.

[6] H.K. Gerhardus, M.P.H. Brongers, N.G. Thompson, Y.P. Virmani, J.H. Payer, Corrosion costs and preventive strategies in the United States, 2001.

[7] U.M. Angst, Challenges and opportunities in corrosion of steel in concrete, Mater. Struct. 51 (2018) 1–20.

[8] Corrosion Control Plan for Bridges, Houston, 2012.

[9] N.R. Council, Assessment of Corrosion education, The National Academies Press, 2009.

[10] H. Torbati-Sarraf, A. Poursaee, Study of the Passivation of Carbon Steel in Simulated Concrete Pore Solution Using Scanning Electrochemical Microscope (SECM), Materialia. (2018).

[11] L. Ding, H. Torbati-Sarraf, A. Poursaee, The influence of the sandblasting as a surface mechanical attrition treatment on the electrochemical behavior of carbon steel in different pH solutions, Surf. Coatings Technol. 352 (2018) 112–119.

[12] H. Torbati-Sarraf, S.A. Torbati-Sarraf, A. Poursaee, T.G. Langdon, Electrochemical behavior of a magnesium ZK60 alloy processed by high-pressure torsion, Corros. Sci. 154 (2019) 90–100.

[13] D. Ahmadkhaniha, M. Fedel, M. Heydarzadeh Sohi, A. Zarei Hanzaki, F. Deflorian, Corrosion behavior of magnesium and magnesium-hydroxyapatite composite fabricated by friction stir processing in Dulbecco's phosphate buffered saline, Corros. Sci. 104 (2016) 319–329.

[14] H. Torbati-Sarraf, A. Poursaee, Corrosion of coupled steels with different microstructures in concrete environment, Constr. Build. Mater. 167 (2018) 680–687.

[15] A. Poursaee, C.M. Hansson, Reinforcing steel passivation in mortar and pore solution, Cem. Concr. Res. 37 (2007) 1127–1133.

[16] D.D. Macdonald, M. Urquidi-Macdonald, Theory of Steady-State Passive Films, J. Electrochem. Soc. 137 (1990) 2395–2402.

[17] Y. Li, Y.F. Cheng, Passive film growth on carbon steel and its nanoscale features at various passivating potentials, Appl. Surf. Sci. 396 (2017) 144–153.

[18] S.J. Ahn, H.S. Kwon, Diffusivity of point defects in the passive film on Fe, Passiv.

Met. Semicond. Prop. Thin Oxide Layers. 579 (2006) 311–316..

[19] F.R. Foulkes, P. McGrath, Rapid cyclic voltammetric method for studying cement factors affecting the corrosion of reinforced concrete, Cem. Concr. Res. 29 (1999) 873–883.

[20] Y. Chen, M.E. Orazem, Impedance analysis of ASTM A416 tendon steel corrosion in alkaline simulated pore solutions, 104 (2016) 26–35.

[21] S. Joiret, M. Keddam, X.R. Nóvoa, M.C. Pérez, C. Rangel, H. Takenouti, Use of EIS, ring-disk electrode, EQCM and Raman spectroscopy to study the film of oxides formed on iron in 1 M NaOH, Cem. Concr. Compos. 24 (2002) 7–15.

[22] M.F. Hurley, J.R. Scully, Threshold chloride concentrations of selected corrosion-resistant rebar materials compared to carbon steel, Corrosion. 62 (2006) 892–904.

CHAPTER 2

Study of the passivation of carbon steel in simulated concrete pore solution using a scanning electrochemical microscope[1]

Introduction

Conventional electrochemical techniques provide valuable information about the passivation and breakdown of the passive layer of the reinforcing steel in concrete environment [1]. However, these are integral methods, and thus, they lack spatial resolution, which is a disadvantage, especially in studying the early stages of the passivation and depassivation processes. In fact, dynamic sequence of corrosion starts at the nano/microscopic level and macroscopic indication of corrosion is only an expression of the final stages of this complex system [2,3]. To fundamentally study this system, it is imperative to conduct the electrochemical tests at the micro-scale [4,5]. The small-scale electrochemical tests also eliminate many issues associated to the electrochemical reactions such as ohmic drop and charging current. In addition, electron transfer and ion transfer can be distinguished using these methods [6–8].

The scanning electrochemical microscopy (SECM) can be used to collect local measurements and is increasingly being used to study corrosion processes. It consists of

[1] H. Torbati-Sarraf, A. Poursaee, Study of the Passivation of Carbon Steel in Simulated Concrete Pore Solution Using Scanning Electrochemical Microscope (SECM), Materialia. (2018).

an ultra-micro-electrode (UME) immersed in a synthetic solution, which is scanned in close proximity to the surface of the specimens to characterize the activity or topography of the solid/liquid interface. Therefore, the SECM can be used to quantitatively detect the reactants and products participating in the corrosion reactions and was used in different application such as corrosion inhibitors, localized corrosion studies [9–15]. Nonetheless, to the best of the authors' knowledge, there is no study on the passivation of carbon steel in concrete environment that utilizes SECM.

The kinetics of the surface reactions that lead to passivation is not well-understood. The aim of this chapter was to investigate the formation of the passive layer on the carbon steel in alkaline environment of concrete as well as to study the kinetics of the passivation process using SECM. Z-approach curves (feedback mode) were recorded at different times over the surface of steel specimen using a potassium ferrocyanide ($K_3Fe(CN)_6$) as the redox mediator in a simulated concrete pore solution. The magnitude of the feedback response depends upon the rate at substrate regenerates the bulk form of the mediator. When the substrate shows high rates of electron transfer, the SECM current will demonstrate a positive feedback response. An overall negative feedback response will result from a slow or hindered reaction that ultimately could be a pure insulator [6,16].

Then, the effective heterogeneous electron transfer rate, k_{eff}, was calculated using the approach curves and Wittstock's method [17]. k_{eff} represents the rate of an electron moves between a chemical species and a solid-state electrode [18]. The value of this

parameter with respect to time was used to obtain information about kinetics and the strength of the passive layer formed on the surface of steel. However, using macroscopic techniques such as voltammetry and impedance to calculate this parameter is time consuming and ohmic drop and polarization may perturb estimation [16,19–22].

Materials and Experimental Procedures

Materials

A reinforcing steel bar, No 4 (φ = ~13 mm), with the chemical composition of 0.39wt.% C, 1.3wt.% Mn, 0.15wt.% Si, 0.03wt.% P and 0.011wt.% S and Fe for balance, was used in this study. A specimen with the length of approximately 10 mm was cut from the bar and mounted with two-part cold epoxy. Then, the exposed surface was abraded continuously to finer grades and then polished with 1 μm alumina powder. A small hole was drilled at the bottom of the mounted specimen and a wire was connected to the specimen for electrical connection. A buffered simulated concrete pore solution with the composition shown in Table 2-1 [23], was used (pH=13.6) in experiments.

Table 2-1. Chemical composition of the material used in other literatures and this study.

Compound	Mol/L
NaOH	0.1
KOH	0.3
$Ca(OH)_2$	0.03
$CaSO_4.H_2O$	0.002
$KCl+K_3Fe(CN)_6$(Mediator)	0.0005

SECM preparation

An M370-dc-SECM, was used to conduct this study. The specimen was placed horizontally, facing upward, in the cell. Scanning probe was a 25 μm diameter platinum wire inside a capillary glass (RG~10). Ag/AgCl and platinized platinum were used as reference and counter electrodes, respectively. To collect the Z-approach curves, after assembling all components, the probe was slowly lowered until it slightly touched the specimen surface; then pulled back for 10 μm, allowing free traveling in the x-y plane. This distance was set as the point with Z = 0.

The UME was positioned at Z = +250 μm above the surface of the specimen and the feedback mode was started on that point, immediately after addition of the solution. The approach started with the speed of 1 μm/s and stopped at Z = 0 (~10 μm above the steel surface). The UME tip was polarized to +550 mV vs Ag/AgCl and recorded current, whilst the steel specimen was kept unbiased. In order to ensure of reproducibility of obtained approach curves, the experiment was repeated for three times on different similar specimens and each time all the preparation procedure was duplicated.

Electron transfer rate calculation

At potentials and pH levels normally measured in the concrete, a protective passive layer forms on the surface of the carbon steel that decreases the anodic

dissolution rate to negligible levels [24–26]. The kinetics of the surface reactions that lead to passivation, however, is not well-understood. This information can be obtained by calculating the effective rate coefficient, k_{eff}, of the regeneration reaction [15, 17]. k_{eff} can be calculated by fitting the experimentally measured Z-approach curves to the numerical/theoretical curves [16,27–29].

In summary, as the UME approaches to the surface, the current is influenced by the normalized distance value of L (the distance/tip diameter). The dimensionless current $I_T(L)$, which is the current at L distance, for the first-order reactions of the mediator can be calculated using Eq. 1:

$$I_T(L) = I_T^{ins}(L) + I_S(L,\kappa)(1 - \frac{I_T^{ins}(L)}{I_T^{con}(L)}) \quad (1)$$

where $I_S(L,\kappa)$ is the kinetically controlled substrate current, and $I_T^{con}(L)$ and $I_T^{ins}(L)$ represent the tip currents for diffusion-controlled regeneration of a redox mediator and for the insulating substrate, respectively. For RG~10, the $I_T^{con}(L)$ and $I_T^{ins}(L)$ can be written as:

$$I_T^{con}(L) = \frac{0.78377}{L} + 0.3315e^{\left(\frac{-1.0672}{L}\right)} + 0.68 \quad (2)$$

$$I_T^{ins}(L) = \frac{1}{(0.15+\frac{1.5358}{L}+0.58e^{(-1.14L)}} + 0.0908e^{(\frac{L-0.63}{1.017L})} \quad (3)$$

$I_S(L,\kappa)$ can be expressed in terms of L using equation 4:

$$I_S(L,\kappa) = \frac{0.78377}{L(1+\frac{1}{\kappa L})} + \frac{[0.68+0.3315e^{(\frac{-1.0672}{L})}}{1+\frac{(\frac{11}{\kappa L})+7.3}{110-40L}} \quad (4)$$

where κ is dimensionless first-order rate constant. The ration $\frac{I_T^{ins}(L)}{I_T^{con}(L)}$ can be obtained for different values of L from Eq. 2 and 3. Similarly, $I_S(L,\kappa)$ can be calculated for different L and κ values using Eq. 4. The, k_{eff} can be calculated using Eq. 5:

$$k_{eff} = \kappa * \frac{D}{r} \quad (5)$$

where r is the radius of the Pt UME, and D is the diffusion coefficient of the mediator in the solution being tested. The k_{eff} is estimated by fitting curves from Eq. 1 to real values, with more than 93% certainty, using least square method.

To obtain the k_{eff}, the value of the diffusion coefficient of potassium ferrocyanide in simulated pore solution was needed. However, this information was not available; thus, this value was calculated through the Randles-Sevcik equation [30,31] which uses the peak current, i_p, obtained from the voltammograms, conducted with different sweep rates as followings:

$$i_p = 0.446nFCA\sqrt{\frac{nF\nu D}{RT}} \quad (6)$$

where, n is the number of electrons involved in the reaction (for $Fe(CN)_6^{3-}+1e^- \leftrightarrow Fe(CN)_6^{4-}$ it is 1), F is the Faraday constant, C is the concentration of the electroactive species (0.5 Mm for potassium ferrocyanide), A is the surface area of the working electrode, T is the temperature (ambient temperature, i.e. 23°C), ν is the sweep rate, R is the gas constant and D is the diffusion coefficient of species.

Several cyclic voltammetry tests were conducted using the 25 μm UME in the pore solution with 0.5 mM potassium ferrocyanide mediator with the scan rates of 1000, 750, 500, 250, 100, 75, 50 and 20 mV/s. The anodic peaks from each voltammogram were obtained, then the value of D was calculated using the slope of the plot of the peak currents, i_p, versus the square root of the scan rate (Figure 2-1). The calculated diffusion coefficient of the oxidation potassium ferrocyanide in the simulated concrete pore solution was $D=8.1\times10^{-7}$ $cm^2.s^{-1}$.

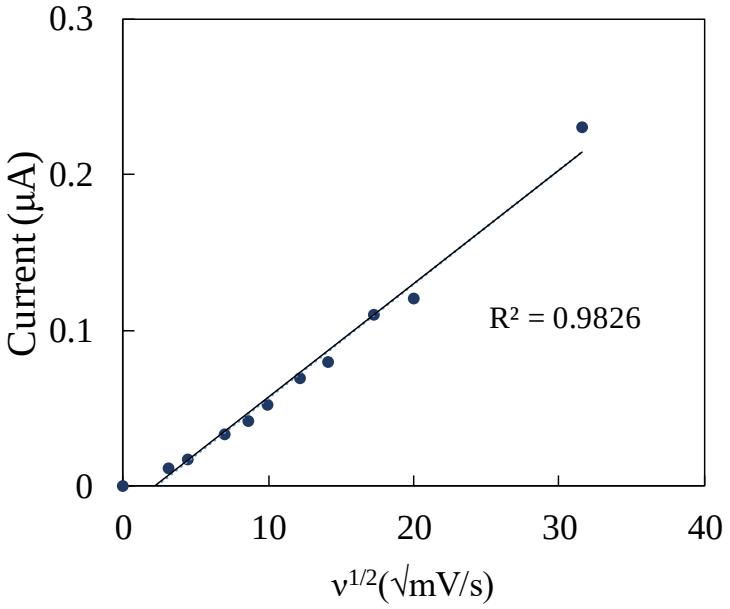

Figure 2-1. The anodic peaks of 0.5 mM potassium ferrocyanide obtained from 25μm UME in simulated concrete pore solution as a function of the square root of the scan rate.

Results and Discussion

Figure 2-2 shows series of Z-approach curves at different times after exposure of freshly polished cross-section of reinforcement carbon steel to the simulated concrete pore solution, which was kept at open circuit potential. In high alkalinity, it is well known that $Fe(OH)_2$, FeOOH and $FeCO_3$ forms on the surface that can effectively inactive the surface of steel [32,33]. Therefore, a negative feedback character was predicted; but obtained curves Figure 2-2 implies that the formation of a passive oxide film on a carbon steel surface is a relatively long process as the initial positive feedback curves fade to negative feedback with the passage of time.

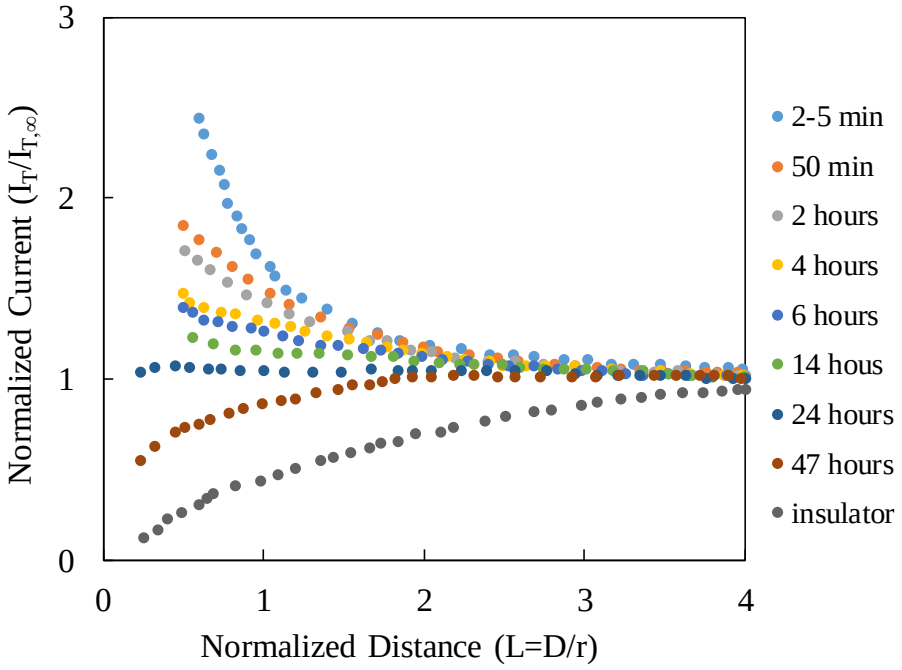

Figure 2-2. Experimental Z-approach feedback curves recorded for carbon steel specimen at different periods of exposure in simulated concrete pore solution with 0.5 mM potassium ferrocyanide

Figure 2-3 presents the calculated k_{eff} (using Eq. 1 through 5) of the potassium ferrocyanide regeneration reaction on the surface of steel in concrete pore solution versus the time of exposure. k_{eff} is a potential dependent parameter [16], but since each feedback curve was acquired in less than 3 min, after 50 min. immersion (second obtained approach curve in Figure2) free potential was almost constant during this short period, thus it can be assumed k_{eff} value is constant for each measurement.

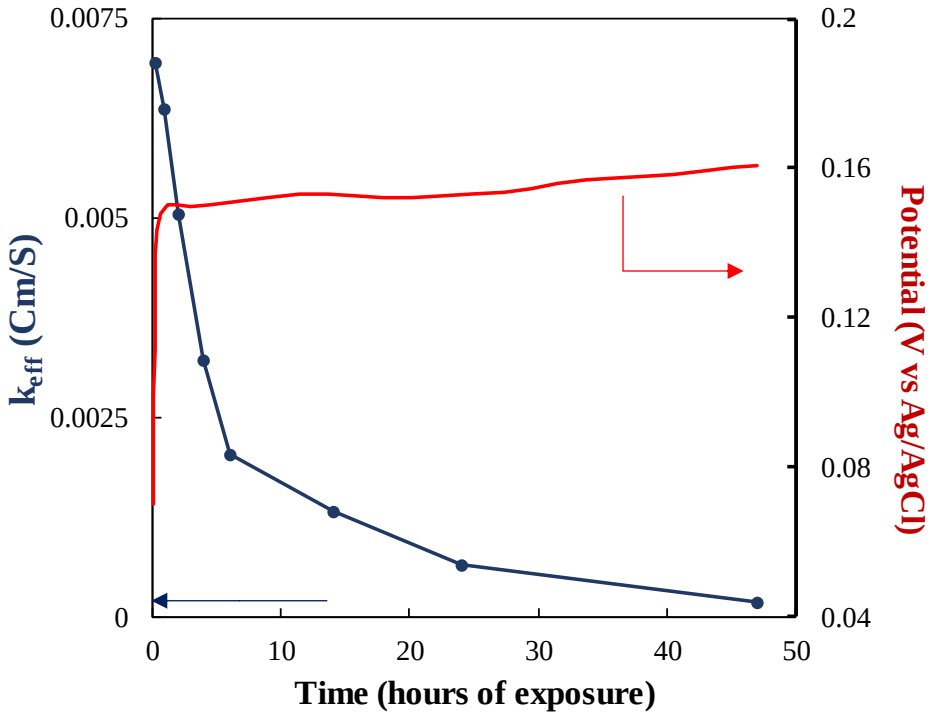

Figure 2-3. Open circuit potential and calculated k_{eff} versus time (obtained from fitting curves in figure 2).

As can be seen, upon exposure to the solution open circuit potential increased and k_{eff} value decreased drastically. Such behavior can be explained by a change in the structure of the oxide film on the surface of carbon steel from a conductor to an insulator. This observation was attributed to the fact that the steel initially was kinetically active and the electron transfer occurred easily between the Fe and the electroactive species, i.e. ions in the pore solution and the mediator. Passive layer forms on the surface of steel in concrete pore solution and ratio of Fe^{2+} to Fe^{3+} increases across the entire depth of the passive layer to the steel substrate [5,27,34–38]. Thus, it was hypothesized that within few minutes after exposure to solution, the steel surface behaves as a pure conductive (first feedback curve in Figure 2-2) and UME continuously accumulated current from the

surface of the steel due direct oxidation of iron[32]. By passing time, the passive layer grew and the k_{eff} decreased continuously; according to point defect model (PDM)[39,40], $Fe^{2+} \rightarrow Fe^{3+} + e^-$ became the dominant oxidation reaction between the mediator and the oxide film. Decreasing the k_{eff} value was attributed to the decrease in the number of liberated electrons and at the same time, due to the more outward flux of Fe^{2+} than the diffusivity of O^{2-}, the oxygen vacancies produced at the interface of steel and the passive layer [37]. Ultimately, by passing the time the donor density of oxide layer decreased [41] and the k_{eff} values approached to a relatively steady state, meaning the complete growth and protection by the passive layer.

Conclusion

This work explained the application of the SECM to study the kinetics of the formation of the passive layer on the surface of carbon steel exposed to the simulated concrete pore solution. Z-approach curves at different times after exposure in pore solution were obtained and by fitting them to theoretical curves, the mediator regenerating heterogeneous rate coefficients, k_{eff}, was calculated. In addition, the diffusion coefficient of potassium ferrocyanide in simulated concrete pore solution was calculated. It was shown that the formation of a passivate layer on the surface of steel was a time-dependent process. It is hypothesized that kinetics of growth of passive film, was the reason of the decreasing in the k_{eff} value. The k_{eff} became steady-state presumably due to the lack of oxygen in the vicinity of steel that lead to complete

formation of the passive layer.

References

[1] A. Poursaee, ed., Corrosion of Steel in Concrete Structures, 1st ed., Woodhead Publishing Series in Civil and Structural Engineering, n.d. https://www.elsevier.com/books/corrosion-of-steel-in-concrete-structures/poursaee/978-1-78242-381-2.

[2] E. Völker, C.G. Inchauspe, E.J. Calvo, Scanning electrochemical microscopy measurement of ferrous ion fluxes during localized corrosion of steel, Electrochem. Commun. 8 (2006) 179–183.

[3] A. Poursaee, Application of agent-based paradigm to model corrosion of steel in concrete environment, Corros. Eng. Sci. Technol. 0 (2018) 1–6.

[4] S. Mehrazi, M. Saremi, J. Neshati, A probe into low-temperature stress corrosion cracking of 304L stainless steel by scanning vibrating electrode technique, Corros. Eng. Sci. Technol. 51 (2016) 358–364.

[5] H. Nanjo, M. Fujimura, N.J. Laycock, Z. Xia, I. Ishikawa, J. Onagawa, The surface nanostructure of pure iron after combined electrochemical passivation and thermal annealing treatments, Surf. Sci. 601 (2007) 5180–5186.

[6] R. Feeney, Determination of heterogeneous electron transfer rate constants at microfabricated iridium electrodes, Electrochem. Commun. 1 (1999) 453–458.

[7] R.K. Zhu, B.T. Lu, J.L. Luo, Y.C. Lu, Effect of cold work on surface reactivity and

nano-hardness of alloy 800 in corroding environments, Appl. Surf. Sci. 270 (2013) 755–762.

[8] M. Zhao, J. Li, G. He, H. Xie, Y. Fu, An investigation of the effect of a magnetic field on the phosphate conversion coating formed on magnesium alloy, Appl. Surf. Sci. 282 (2013) 499–505.

[9] J. Molina, J. Fernández, F. Cases, Scanning electrochemical microscopy for the analysis and patterning of graphene materials: A review, Synth. Met. 222 (2016) 145–161.

[10] D. Polcari, P. Dauphin-Ducharme, J. Mauzeroll, Scanning Electrochemical Microscopy: A Comprehensive Review of Experimental Parameters from 1989 to 2015, Chem. Rev. 116 (2016) 13234–13278

[11] A.G. Marques, J. Izquierdo, R.M. Souto, A.M. Simões, SECM imaging of the cut edge corrosion of galvanized steel as a function of pH, Electrochim. Acta. 153 (2015) 238–245.

[12] C. Li, L. Li, C. Wang, Study of the inhibitive effect of mixed self-assembled monolayers on copper with SECM, Electrochim. Acta. 115 (2014) 531–536.

[13] E. Salamifar, M.A. Mehrgardi, M.F. Mousavi, Ion transport and degradation studies of a polyaniline-modified electrode using SECM, Electrochim. Acta. 54 (2009) 4638–4646.

[14] Y. Yuan, L. Li, C. Wang, Y. Zhu, Study of the effects of hydrogen on the pitting processes of X70 carbon steel with SECM, Electrochem. Commun. 12 (2010) 1804–1807.

[15] A. Davoodi, J. Pan, C. Leygraf, S. Norgren, Probing of local dissolution of Al-alloys in chloride solutions by AFM and SECM, Appl. Surf. Sci. 252 (2006) 5499–5503.

[16] S. Bollo, S. Finger, J.C. Sturm, L.J. Núñez-Vergara, J.A. Squella, Cyclic voltammetry and scanning electrochemical microscopy studies of the heterogeneous electron transfer reaction of some nitrosoaromatic compounds, Electrochim. Acta. 52 (2007) 4892–4898.

[17] S.E. Pust, D. Scharnweber, S. Baunack, G. Wittstock, Electron Transfer Kinetics at Oxide Films on Metallic Biomaterials, J. Electrochem. Soc. 154 (2007) C508.

[18] W.R. Fawcett, The role of the metal and the solvent in simple heterogeneous electron transfer reactions, Electrochim. Acta. 42 (1997) 833–839.

[19] A.M. Bond, T.L.E. Henderson, D.R. Mann, T.F. Mann, W. Thormann, C.G. Zoski, A fast electron transfer rate for the oxidation of ferrocene in acetonitrile or dichloromethane at platinum disk ultramicroelectrodes, Anal. Chem. 60 (1988) 1878–1882.

[20] A.M. Bond, K.B. Oldham, C.G. Zoski, Theory of electrochemical processes at an inlaid disc microelectrode under steady-state conditions, J. Electroanal. Chem. Interfacial Electrochem. 245 (1988) 71–104.

[21] L. V. Protsailo, W.R. Fawcett, Studies of electron transfer through self-assembled monolayers using impedance spectroscopy, Electrochim. Acta. 45 (2000) 3497–3505.

[22] O. Fontaine, C. Lagrost, J. Ghilane, P. Martin, G. Trippé, C. Fave, J.C. Lacroix, P. Hapiot, H.N. Randriamahazaka, Mass transport and heterogeneous electron transfer of a ferrocene derivative in a room-temperature ionic liquid, J. Electroanal. Chem. 632 (2009)

88–96.

[23] A. Poursaee, C.M. Hansson, Reinforcing steel passivation in mortar and pore solution, Cem. Concr. Res. 37 (2007) 1127–1133.

[24] T. Zakroczymski, Kinetics and Mechanism of Passive Film Formation on Iron in 0.05M NaOH, J. Electrochem. Soc. 132 (1985) 2862. doi:10.1149/1.2113684.

[25] M.F. Montemor, A.M.P. Simões, M.G.S. Ferreira, Analytical Characterization of the Passive Film Formed on Steel in Solutions Simulating the Concrete Interstitial Electrolyte, Corrosion. 54 (1998) 347–353.

[26] H. Torbati-Sarraf, A. Poursaee, Corrosion of coupled steels with different microstructures in concrete environment, Constr. Build. Mater. 167 (2018) 680–687.

[27] C. Wei, A.J. Bard, M. V. Mirkin, Scanning Electrochemical Microscopy. 31. Application of SECM to the Study of Charge Transfer Processes at the Liquid/Liquid Interface, J. Phys. Chem. 99 (1995) 16033–16042.

[28] P. Sun, Z. Liu, H. Yu, M. V Mirkin, Effect of mechanical stress on the kinetics of heterogeneous electron transfer., Langmuir. 24 (2008) 9941–4.

[29] A. Asserghine, D. Filotás, L. Nagy, G. Nagy, Scanning electrochemical microscopy investigation of the rate of formation of a passivating TiO 2 layer on a Ti G4 dental implant, Electrochem. Commun. 83 (2017) 33–35.

[30] Z.O. Ameur, M.M. Husein, Electrochemical Behavior of Potassium Ferricyanide in Aqueous and (w/o) Microemulsion Systems in the Presence of Dispersed Nickel Nanoparticles, Sep. Sci. Technol. 48 (2013) 681–689.

[31] K. Ngamchuea, S. Eloul, K. Tschulik, R.G. Compton, Planar diffusion to macro

disc electrodes—what electrode size is required for the Cottrell and Randles-Sevcik equations to apply quantitatively?, J. Solid State Electrochem. 18 (2014) 3251–3257.

[32] D.D. MacDonald, B. Roberts, The cyclic voltammetry of carbon steel in concentrated sodium hydroxide solution, Electrochim. Acta. 23 (1978) 781–786. doi:10.1016/0013-4686(78)80039-5.

[33] W. Chen, R.G. Du, C.Q. Ye, Y.F. Zhu, C.J. Lin, Study on the corrosion behavior of reinforcing steel in simulated concrete pore solutions using in situ Raman spectroscopy assisted by electrochemical techniques, Electrochim. Acta. 55 (2010) 5677–5682.

[34] M.A. Climent, C. Gutiérrez, Proof by UV-visible modulated reflectance spectroscopy of the breakdown by carbonation of the passivating layer on iron in alkaline solution, Surf. Sci. 330 (1995) 2–7.

[35] C.G. Zoski, M. V. Mirkin, Steady-state limiting currents at finite conical microelectrodes, Anal. Chem. 74 (2002) 1986–1992.

[36] B. Huet, V. L'Hostis, F. Miserque, H. Idrissi, Electrochemical behavior of mild steel in concrete: Influence of pH and carbonate content of concrete pore solution, Electrochim. Acta. 51 (2005) 172–180.

[37] Z.H. Dong, W. Shi, G.A. Zhang, X.P. Guo, The role of inhibitors on the repassivation of pitting corrosion of carbon steel in synthetic carbonated concrete pore solution, Electrochim. Acta. 56 (2011) 5890–5897.

[38] H.B. Gunay, P. Ghods, O.B. Isgor, G.J.C. Carpenter, X. Wu, Characterization of atomic structure of oxide films on carbon steel in simulated concrete pore solutions using EELS, Appl. Surf. Sci. 274 (2013) 195–202.

[39] D.D. Macdonald, The history of the Point Defect Model for the passive state : A brief review of film growth aspects, Electrochim. Acta. 56 (2011) 1761–1772.

[40] Y. Li, Y.F. Cheng, Applied Surface Science Passive film growth on carbon steel and its nanoscale features at various passivating potentials, Appl. Surf. Sci. 396 (2017) 144–153.

[41] A. Poursaee, Temperature dependence of the formation of the passivation layer on carbon steel in high alkaline environment of concrete pore solution, Electrochem. Commun. 73 (2016) 24–28.

CHAPTER 3

Corrosion improvement of carbon steel in concrete environment through modification of the steel microstructure[2]

Introduction

Corrosion affects a steel reinforced concrete structure's integrity. Increasing the corrosion resistance of the reinforcement is the most effective corrosion control method. The first and most reasonable mean for this concept is using alloying element in steel. Addition of a certain amount of Cr, Mo or Ni to steel during its manufacturing process decreases its corrosion rate by formation a corrosion resistance protective oxide layer on the surface that controls or hinders the corrosion in most environments. However, unless in certain applications, exploiting these types of steels, i.e. stainless steel, in the concrete environment does not have economic justification due to their high cost.

The other method that affects the corrosion resistance of steel is the modification of its microstructure, either during steel manufacturing or post-treatment procedure. Any changes in microstructure particularly grain size, grain size distribution and phase properties can affect the electrochemical behavior of steel. Indeed, the microstructure of the steel affects the formation and breakdown of the passive layer [1]. Little analysis has

[2] H. Torbati-Sarraf, A. Poursaee, Corrosion Improvement of Carbon Steel in Concrete Environment through Modification of Steel Microstructure, J. Mater. Civ. Eng. 31 (2019) 2–7.

been undertaken on this subject; none of them studied the impact of grain size of carbon steel on its corrosion activity in the high alkaline environment in concrete. The objective of this project was to assess the impact of the steel grain size on the occurrence of corrosion in concrete environments.

Steel microstructure, heat treatment and grain size refinement

Pure iron at temperatures below approximately 910°C has a Body-Centered Cubic structure (BCC). When heated above this temperature, the iron structure changes to a Face-Centered Cubic structure (FCC). When cooled, the change is reversed, and a BCC structure is again formed. Up to 2.0 wt.% carbon can dissolve in FCC iron, forming what is known as a solid solution, whereas in BCC iron no more than 0.02 wt.% carbon can dissolve in this way [2]. The solid solutions of carbon atoms in FCC iron and BCC iron are called austenite (γ) and α-ferrite, respectively. Any piece of steel is made up of a large number of grains, which are regions of regularity or crystallinity and the surfaces between them is called grain boundaries.

Influence of steel microstructure on its corrosion behavior

Little analysis has been undertaken on this subject; to date mostly the surface conditions studied have been at the mill scale on “as-received” steel bars, with the effects of this mill scale emphasizing the corrosion and passivation of the steel [6-8]. Modification of the steel grain size may well positively enhance corrosion resistance, however. In their investigation of the effect of grain size reduction on the

electrochemical corrosion behavior of nano-crystalline Fe in alkaline solution (10 wt.% NaOH), Afshari and Dehghanian concluded that the crystal grain size has important role in the resistance of the passive layer. Specifically, they observed a considerable increase in the corrosion resistance of Fe in weak alkaline solution with a decrease in grain size from the micro- to nano-crystalline [9]. Similarly, in their examination of the effect of grain size on the corrosion of mild steel in seawater, Jizhou et al. concluded that the corrosion rate increase with increasing the grain size [10]. A study by Gollapudi determined the existence of a finer and more compact passive layer within that fine microstructure, unlike the coarse-grained microstructure, which exhibited a more open passive layer [11]. Wang et al. concluded that the uniformity of passive layer on the fine microstructure was the result of the fine distribution of grain boundaries in contrast to the coarse distribution of these defects in a coarse-grained microstructure [12]. Ghosh et al. observed that in corrosive environments, the fine-grained materials corroded more uniformly than the coarse-grained alloys [13]. They suggested that the large volume fraction of grain boundaries combined with the fine grain size in fine materials ensured that the pits formed were shallow and closely connected resulting in uniform corrosion conditions. In contrast, the coarse-grained material with less grain boundary volume underwent localized corrosion which caused the formation of large isolated pits. They concluded that under active conditions, the extent of uniform or localized corrosion was again dependent on the grain size distribution. Poursaee and Saremi found that a surface heat-treatment consisting of carburizing and normalizing significantly improved the corrosion resistance of steel bars in concrete pore solution [14]. They hypothesized that

the more corrosion resistant phase of Fe_3C and finer grains formed on the surface decreased the corrosion rate. As above-mentioned, the impact of steel grain size on formation of the passive layer and the consequent corrosion is an important fact, and has been addressed in many studies, yet gaps in the literature exist. As far as the authors are concerned most of the previous studies, (except [14]), emphasized the impact of the steel microstructure on its corrosion in acidic-to-mild alkaline environment which do not represent the concrete environment.

Materials and experimental procedures

Specimen preparation

#4 (ϕ= ~12.7 mm) reinforcing steel bar was used in the project. To ascertain uniformity, specimens were cut and prepared from one bar. The main alloying elements were 0.39wt.% C, 1.3wt.% Mn, 0.15wt.% Si, 0.03wt.% P and 0.011wt.% S and Fe for balance. Specimens were cut into the length of 10 mm and after the required heat-treatments, they were epoxy mounted. To avoid any undesirable and unplanned microstructural change (including phase transformation, stress relief, etc.) low shrinkage cold epoxy were used for mounting. The surfaces of the epoxy mounted specimens were grounded, using 80 to 1200 grit SiC sandpaper, and then polished to 1μm using alumina slurry. The bottom epoxy portion up to the surface of the specimen bottom of each epoxy mounted specimen was drilled, and a copper wire was attached to the steel specimen to establish electrical connection. Then the hole was filled with epoxy. This procedure of

wire connection obviated the use of high temperature wire soldering that might alter the microstructure.

Heat-treatments were carried out using an electric furnace. Three different microstructures were used in this study: as-received, fine, and coarse. The grain size of the fine specimens was approximately half the size of the grains in the as-received specimens and the grain size of the coarse specimens was approximately two times larger than those in the as-received specimens. For heat-treatment, a benchtop muffle electric furnace with the heating rate of ~3oC/s was used. The fine specimens were prepared, using the method suggested by [15, 16] as the guideline. First, the as-received specimens were kept at 820 °C for 1 h and then air-cooled. Then, they were heated again to 710 °C for 30 min. nd air-cooled. To prepare the coarse specimens, the specimens were heated at 1020 °C for 1 h and then air-cooled. The time and temperature for both heat-treatment were selected based on the several trials. To examine the heat-treated specimens, 4% nital (4 mL of 15 M nitric acid in 96 mL ethanol) solution was used to etch the surface and reveal the microstructure of the specimens exposed to different heat-treatments. Each specimen was etched approximately 4 s and then washed with de-ionized water immediately and sprayed with ethanol and dried using air.

Electrochemical tests

Concrete simulated pore solution, with the composition given in Table 3-1, was used as the electrolyte in each cell to simulate the concrete environment [17].

Table 3-1. The composition of the simulated concrete pore solution.

Compound	mol/L
NaOH	0.1
KOH	0.3
$Ca(OH)_2$	0.03
$CaSO_4.H_2O$	0.002

Three identical specimens of each microstructure, i.e. as-received, find and coarse, were used in each measurement cell. The plastic container with the specimens and pore solution was sealed to minimize the carbonation. To keep the pH and oxygen level in the solution constant, the solution in each measurement cell was partially refreshed twice a month. The pH of the solution was periodically measured during the experiment to ascertain the pH remained around 13.2. To ascertain passivation, the specimens were exposed to chloride-free pore solution for 10 days and then 3 wt.% NaCl was added to solution and specimens were immersed in the chloride-contaminated pore solution for 60 days.

A three-electrode measurement setup, including a specimen as the working electrode, an SCE (saturated calomel electrode) as the reference electrode, and a 316L stainless-steel sheet as the counter electrode, were used for the LPR (linear polarization resistance), CP (cyclic polarization) and CV (cyclic voltammetry) and EIS (electrochemical impedance spectroscopy) tests. All electrochemical measurements were conducted at ambient temperature.

Corrosion potentials were measured every 10 min. starting immediately after

immersing the specimens in the solution, using an automated measuring system [18]. To determine the corrosion current densities of the specimens, the LPR within the range of ±10 mV vs. corrosion potential with the scan rate of 0.166 mV/s [19] was conducted on all specimens every 10 days. CP technique was carried out on one of the specimens in each cell to analysis the protectiveness of the passive film and the pitting susceptibility of the specimens. This test started at -100 mV below the corrosion potential to +500 mV vs. SCE and then decreased to -100 mV below the corrosion potential with the scan rate of 0.166 mV/s. CV was conducted to study oxidation and reduction behaviors of each specimen. The voltammograms were obtained between voltage limits of -1.4 V and +0.4 V vs. SCE at a linear sweep rate of 20 mV/s. The conventional EIS with sinusoidal perturbation of ±10mV, the frequency range of 100 kHz to 10 mHz was used to study the electrochemical behavior of the surface in solution.

Results and discussion

Figure 3-1 shows the microscopic images of the specimens. Phases, grain size distribution, and grain size, were determined using ASTM E112 [20]. Grain size, grain size distribution, and the ASTM number were also calculated which are given in

Table 3-2.

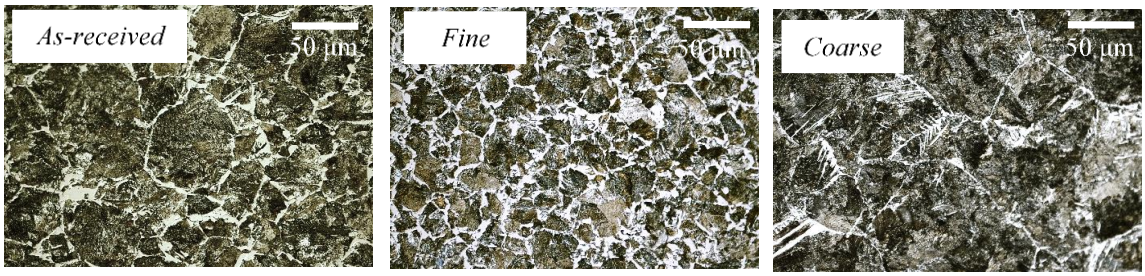

Figure 3-1. Optical microscopic images of the specimens.

Table 3-2. Grain size distribution and free ferrite portion of as-received and heat-treated steel rebar.

Specimen	Average grain size (µm)	ASTM #
As-received	57	5-6
Fine	24	8
Coarse	90	4

The results of the corrosion potential and corrosion current density measurements are shown in Figure 3-2. 24 h after addition of 3 wt.% NaCl, the corrosion potential values of the as-received specimens drastically dropped, showing that the passive layer could not protect the as-received specimens. A small drop of the corrosion potential was also observed for the fine specimens, while the potential of the coarse specimens continued to increase. The current density values (

Figure 3-2b) agreed with the trend observed from the corrosion potential measurements. The as-received specimens showed the worst corrosion resistance, followed by the fine and coarse specimens.

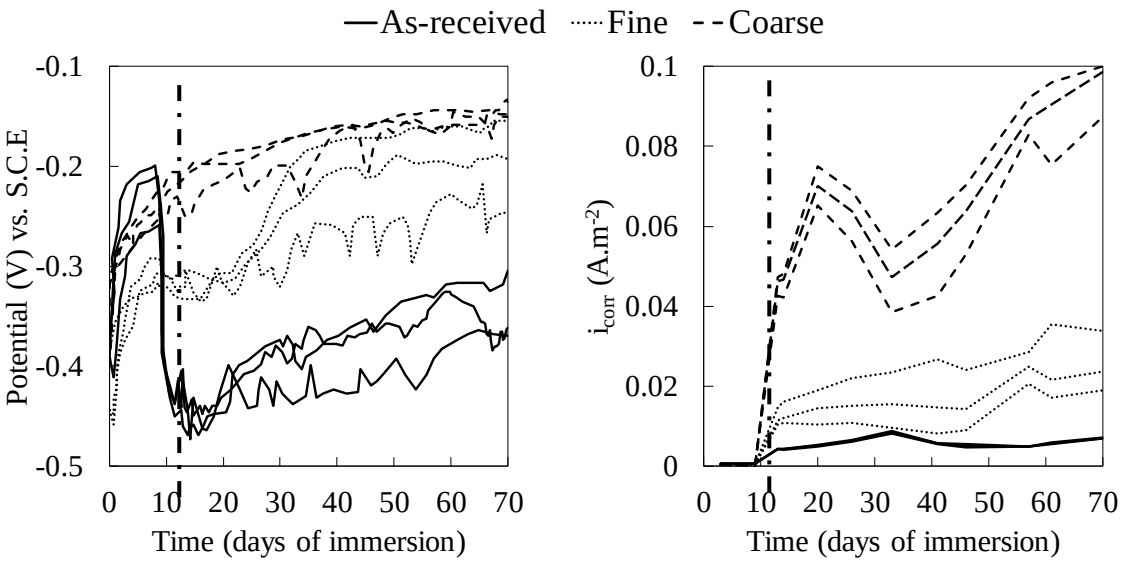

Figure 3-2. (a) Corrosion potential values and (b) corrosion current densities of the specimens.

Mass loss during the exposure time was calculated using Faraday's law [21] and the results are shown in Figure 3-3. As can be seen, the mass loss in coarse and fine specimens compared to the as-received specimens decreased ~91% and ~72%, respectively.

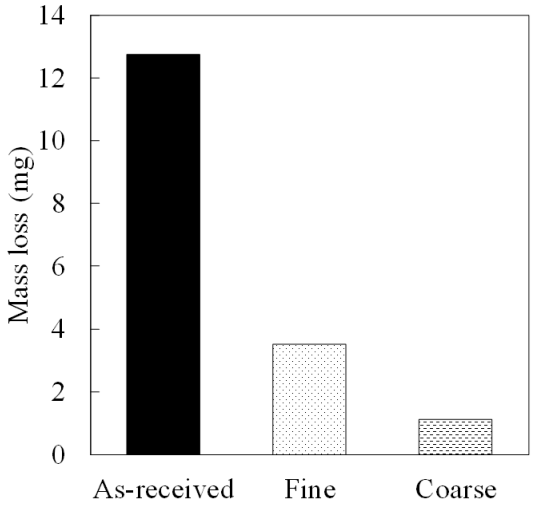

Figure 3-3. The calculated average mass loss for the specimens during the entire time of exposure.

Figure 3-4 shows the results of the cyclic polarization experiments on one the specimens from each microstructure, 42 days after exposure to the chloride-contaminated pore solution. As can be seen the location of the curves and the size of the cycle loops for both fine and coarse specimens showed more corrosion resistance compared to the as-received specimen.

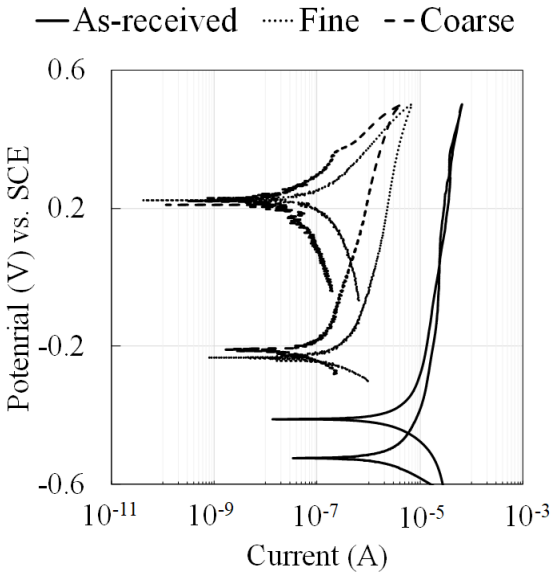

Figure 3-4. Cyclic polarization plots from three different microstructures, immersed 42 days in chloride-contaminated pore solution with 3 wt.% NaCl.

Voltammograms from the results of the cyclic voltammetry tests in chloride-contaminated pore solution for ten cycles perturbation performed at a scan rate of 50 mV/s are given in Figure 3-5. Peak a was attributed to the formation of a layer consisted of $Fe(OH)_2$ and FeO, peak b was ascribed to the transformation of Fe^{2+} to Fe^{3+}, and Peak d appeared as the result of the reduction reactions corresponding to the anodic reactions at Peak b. Peak c was attributed to an oxidation within the compact passive layer, due to

the formation of the Fe_2O_3, Fe_3O_4, and FeOOH and Peak e was appeared as the result of the reduction reactions for Peak c [22-23] . These results indicated that the redox reactions on all specimens are similar. However, regardless of the position of the peaks, as-received specimen showed wider hysteresis loop in both oxidation and reduction potentials, which was due to more activity on its surface. In addition, the as-received specimen showed higher current density values for peaks a, b and c compared to the other specimens, indicating more oxidation reactions on that specimen compared to the other specimens.

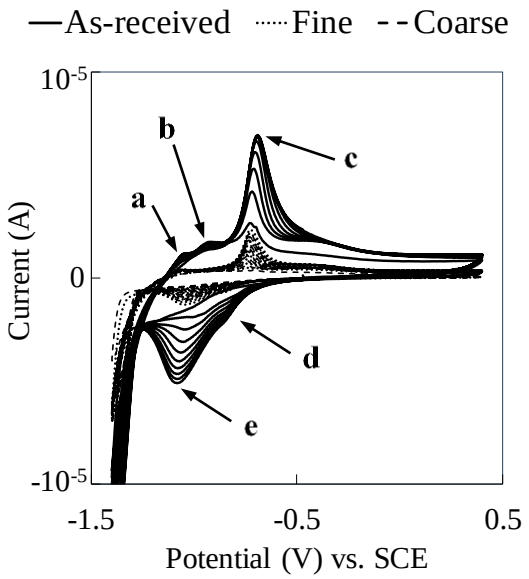

Figure 3-5. *Cyclic voltammogram curves from three different microstructures obtained in chloride-contaminated pore solution.*

The results of all electrochemical tests showed that the corrosion resistance of the heat treatment specimens increased compared to the as-received specimen. In addition, the coarse specimen showed superior performance compared to the fine specimen. It was

hypothesized that the grain distribution and the proportion of different phases in the grains were the reason for such observation.

To determine the grain distribution within each specimen, Image analysis was conducted on the microscopic images, using SPIP software [33]. For this purpose, for each specimen, three images from different magnifications, (i.e. 20×, 50×, 100×, and 200×) were selected. Using images from different magnification minimized the measurement error. Results of this analysis are shown in Figure 3-6.

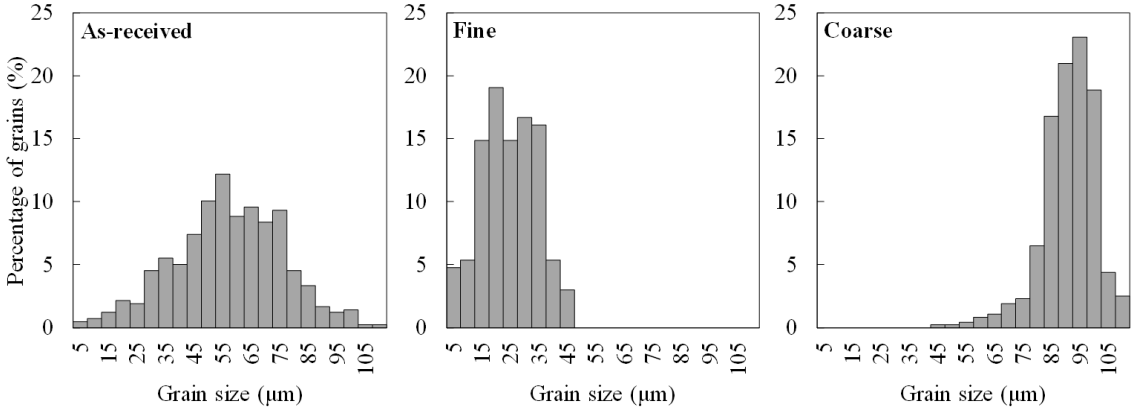

Figure 3-6. The average grain size distribution in different specimens.

As can be seen, the as-received specimens had the widest distribution among the specimens. Both heat-treated specimens had more uniform and less distribution compared to the as-received specimens. Thus, the better corrosion performance of the heat-treated specimens compared to the as-received specimens was due to more uniform and even distribution of the grain throughout the specimens compared to the as-received specimens. The amount of pro-eutectoid α-ferrite (free ferrite) on the grain boundaries

was also calculated, using image analysis. Image analysis results showed that the approximately 10% of the surafce was pre-eutectoid α-ferrite for as-received specimens while this amount for fine and coarse specimens were 18% and 6.5% of surface area, respectively. It seems that the grain size distribution was the overarching reason for the better performance of the heat-treated specimens compared to the as-received specimens. However, it was hypothesized that the lower free ferrite in coarse specimens was the reason for its superior performance compared to the fine specimens. It was reported that the cementite in pearlite acted as a cathodic site in the carbon steel [34,35]. Thus, the lower free ferrite in coarse specimens, left more ferrite in the pearlite structure. The ratio of the ferrite to the cementite in pearlite directly affected the kinetics of corrosion. The higher the ferrite content in the pearlite, led to the higher the anode-to-cathode ratio in coarse specimens which consequently improved their overall corrosion resistance compared to the fine specimens.

Conclusions

Microstructure alternation through heat-treatment influenced the electrochemical behavior of reinforcing steel in a concrete environment. Both heat-treated specimens, with approximately twice finer and coarser grains with respect to the as-received specimens, indicated superior corrosion performance compared to the as-received specimens. This was attributed to the better grain distribution throughout the heat-treated specimens compared to the as-received specimens. The specimens with coarse grains showed the best corrosion resistance among other specimens. Their corrosion current

densities and potential values remained in the range of passive corrosion after 60 days exposure in chloride-contaminated pore solution. The better corrosion resistance of the coarse specimens compared to the fine specimens was attributed to the lower free ferrite on the grain boundaries of these specimens which provided more ferrite to the pearlitic structure. This observation led to an increase of the anode-to-cathode ratio in coarse specimens which significantly impacted the kinetics of corrosion.

It should be noted that the reported results and disruptions were based on three grain sizes and limited experiments. Certainly, more experiments, including using another type of carbon steel, and more grain sizes and grain distributions are required to confidentially recommend the steel with modified microstructure for use in a real concrete structure.

References

[1] H. Torabati-Sarraf, A. Poursaee, Corrosion of coupled steels with different microstructures in concrete environment, Constrcution and Building Materials, 167 (2018) 680-687.

[2] W. Smith, J. Hashemi, Foundations of Materials Science and Engineering, 5 ed., McGraw-Hill, 2009.

[3] T. G. Digges, S. J. Rosenberg, G. W. Geil, Heat Treatment and Properties of Iron and Steel, in: National Bureau of Standards Monograph 88, United States Department of Commerce, Washington DC, 1966.

[4] G. E. Totten, Steel heat treatment: metallurgy and technologies, CRC Press, 2006.

[5] ASM, Metals handbook: Heat Treating, ASM International, 2014.

[6] E. Mahallati, M. Saremi, An assessment on the mill scale effects on the electrochemical characteristics of steel bars in concrete under DC-polarization, Cem. Concr. Res, 36 (2006) 1324-1329.

[7] P. Ghods, Multi-scale investigation of the formation and breakdown of passive films on carbon steel rebar in concrete, PhD thesis in Civil Engineering, Carlton University, (2010).

[8] T. D. Marcotte, Characterization of Chloride-Induced Corrosion Products that form in Steel-Reinforced Cementitious Materials, PhD thesis, University of Waterloo, (2001).

[9] V. Afshari, C. Dehghanian, Effects of grain size on the electrochemical corrosion behavior of electrodeposited nanocrystalline Fe coatings in alkaline solution, Corros. Sci, 51 (2009) 1844–1849.

[10] D. Jizhou, H. Baorong, H. Yanliang, S. Huyuan, L. Yan, M. Shide, Corrosion of mild steel in different granularity seabed sediment saturated with seawater, Materials and Corrosion, 53 (2002) 845-849.

[11] S. Gollapudi, Grain size distribution effects on the corrosion behaviour of materials, Corros. Sci, 62 (2012) 90-94.

[12] L. Wang, Y. Lin, Z. Zeng, W. Liu, Q. Xue, L. Hua, J. Zhang, Electrochemical corrosion behavior of nanocrystalline Co coatings explained by higher grain boundary density, Electrochim. Acta, 52 (2007) 4342–4350.

[13] S. K. Ghosh, G. K. Dey, R. O. Dusane, A. K. Grover, Improved pitting corrosion behavior of electrodeposited nanocrystalline Ni–Cu alloys in 3.0 wt.% NaCl solution,

Journal of Alloys and Compounds, 426 (2006) 235-243.

[14] A. Poursaee, M. Saremi, Corrosion of heat-treated steel bars in concrete synthetic pore solution, Magazine of Concrete Research, 64 (2012) 395-400.

[15] Q. F. Wang, C. Y. Zhang, W. W. Xu, S. J. Zhao, X. Q. Zhao, Z. S. Yan, Refinement of S\steel austenite grain under an extremely high degree of superheating, Journal of Iron and Steel Research, International, 14 (2007) 161-166.

[16] S. W. Mahajan, G. Venkataraman, A. K. Mallik, Grain refinement of steel by cyclic Rrapid heating, 345 (1973) 337–345., Metallography, 6 (1973) 337-345.

[17] A. Poursaee, C. M. Hansson, Reinforcing steel passivation in mortar and pore solution, Cem. Concr. Res, 37 (2007) 1127-1133.

[18] A. Poursaee, Automatic system for monitoring corrosion of steel in concrete, Advances in Engineering Software, 40 (2009) 1179–1182.

[19] ASTM, G 61-86: Standard Test Method for Conducting Cyclic Potentiodynamic Polarization Measurements for Localized Corrosion Susceptibility Iron-, Nickel-, or Cobalt-Based Alloys. , in, 2018.

[20] ASTM, E112: Standard Test Methods for Determining Average Grain Size, (2012).

[21] A. Poursaee, Potentiostatic transient technique, a simple approach to estimate the corrosion current density and Stern–Geary constant of reinforcing steel in concrete, Cem. Concr. Res, 40 (2010) 1451–1458.

[22] F. R. Foulkes, P. McGrath, Rapid cyclic voltammetric method for studying cement factors affecting the corrosion of reinforced concrete, Cem. Concr. Res, 29 (1999) 873-883.

[23] D. D. MacDonald, B. Roberts, The cyclic voltammetry of carbon steel in concentrated sodium hydroxide solution, Electrochim Acta, 23 (1978) 781-786.

[24] M .K. Ravikumar, T. S. Balasubramanian, K. Shukla, S. Venugopalan, A cyclic voltammetric study on the electrocatalysis of alkaline iron-electrode reactions Journal of Applied Electrochemistry, 26 (1996) 1111-1115.

[25] G. P. Kalaignan, V. S. Muralidharan, K. I. Vasu, Triangular potential sweep voltammetric study of porous iron electrodes in alkali solutions, Journal of Applied Electrochemistry, 17 (1987) 1083-1092.

[26] M. Sánchez, J. Gregori, M. C. Alonso, J. J. García-Jareño, F. Vicente, Anodic growth of passive layers on steel rebars in an alkaline medium simulating the concrete pores, Electrochim. Acta, 52 (2006) 47-53.

[27] K. Tang, Stray current induced corrosion of steel fibre reinforced concrete, Cem. Concr. Res, 100 (2017) 445-456.

[28] R. R. Hussain, A. Alhozaimy, A. Al-Negheimish, D. D. N. Singh, Time-dependent variation of the electrochemical impedance for thermo-mechanically treated versus plain low alloy steel rebars in contact with simulated concrete pore solution, Constrcution and Building Materials, 73 (2014) 283-288.

[29] W. Wang, H. Chen, X. Li, Z. Zhu, Corrosion behavior of steel bars immersed in simulated pore solutions of alkali-activated slag mortar, Constrcution and Building Materials, 143 (2017) 289-297.

[30] J. K. Singh, D. D. N. Singh, The nature of rusts and corrosion characteristics of low alloy and plain carbon steels in three kinds of concrete pore solution with salinity and

different pH, Corros. Sci, 56 (2012) 129-142.

[31] L. D. Burke, D. P. Whelan, Growth of electrochromic film on nickel in base under potential cycling conditions, Journal of Electroanalytical Chemistry, 109 (1980) 385-388.

[32] L. D. Burke, M. E. G. Lyons, The formation and stability of hydrous oxide films on iron under potential cycling conditions in aqueous solution at high pH, Journal of Electroanalytical Chemistry, 198 (1986) 347-368.

[33] Image Metrology, Scanning Probe Image Processor (SPIP), https://www.imagemet.com/products/spip/, (2018).

[34] E. W. Revie, H. H. Uhlig, Corrosion and corrosion control: an introduction to Corros. Sci and engineering, John Wiley & Sons, Inc., Hoboken, New Jersey and Toronto, Canada, 2008.

[35] D. Trejo, P. J. Monteiro, Corrosion performance of conventional (ASTM A615) and low-alloy (ASTM A706) reinforcing bars embedded in concrete and exposed to chloride environments, Cem. Concr. Res, 35 (2005) 562-571.

CHAPTER 4

Corrosion of Coupled Steels with Different Microstructures in Concrete Environment[1]

Introduction

In the alkaline environment of concrete, a protective passive film forms on the surface of the embedded steel bar which makes it resistant to corrosion. Many studies have been focused on determining the growth mechanism of this passive film, its structure, and composition in alkaline solution [1-6]. However, this passive film damages and leads to localized corrosion when pH or the chloride concentration of environment reach the critical values [7-9]. Steel composition and microstructure can affect the formation and breakdown of this the passive film, consequently the corrosion and mechanical properties of the steel [10-13]. Steel reinforcing bars are produced through the different manufacturing process. Conventionally, hot rolled and air-cooled mild steel have been used in this industry. However, recently, high strength bars are becoming more popular [14-16]. Thermomechanical treated steel bars are in this category. These steel

[1] H. Torbati-Sarraf, A. Poursaee, Corrosion of coupled steels with different microstructures in concrete environment, Constr. Build. Mater. 167 (2018) 680–687.

bars generally have an outer layer consisted of tempered martensite phase and an inner core made of ferrite-pearlite phases. The combination of different phases in these steel bars improves the load-bearing and ductility of these steels compare to the single-phase bars [10,12,15]. Unless specifically mentioned, both of the above-mentioned bars can be embedded in concrete [17,18], thus; in practice, both types of steels may be connected and used together. Since these steels have different phases and approximately 10% of the surafce was pre-eutectoid α-ferrite for as-received specimens while this amount for fine and coarse specimens were 18% and 6.5% of surface area, respectively. this connection could lead to corrosion, particularly in the joints, due to galvanic effect. The objective of this work was to evaluate and compare the passivation and corrosion behavior of steel bars with different microstructures, individually and when they were connected.

Materials and Experimental Procedures

#4 steel bars from two different suppliers, satisfying the ASTM A615 standard [18], with the chemical composition given in Table 4-1 were used in this investigation. Microscopic analysis revealed (Section 3) that Steel A had tempered martensitic microstructure on its surface while Steel B had ferrite-pearlite microstructure.

For microstructure analyses, 10 mm long pieces of each type of the steel were cut and mounted in two-part cold epoxy. Then, the specimens were ground, polished and etched in 4% nital solution. For electrochemical measurement**,** 100 mm long pieces of

each bar were cut, and then slightly wire brushed and cleaned by alcohol and dried with a hairdryer. Each specimen was coated with three layers of U.V. cure vinyl ester epoxy resin, except 25 mm of the midsection, the exposed area, and 10 mm of one end of each specimen for electrical connection.

Table 4-1. The main alloying elements in the steel specimens used in this study.

Alloying element (%)	C	Mn	P	S	Si	Cu	Ni	Mo	V
A	0.31	1.23	0.018	0.024	0.29	0.23	0.08	0.016	0.002
B	0.39	1.37	0.03	0.011	0.15	-	-	-	-

Three cells with three bars in each one were used in this experiment. One cell contained three bar of Steel A, one cell contained three bars of Steel B, and the last cell had tree coupled bars of A and B. Figure 4-1, schematically shows the measurement cells. Concrete simulated pore solution, with the composition given in Table 4-2, was used as the electrolyte in each cell to simulate the concrete environment [5].

The advantage of performing the experiments in the solution rather than in concrete is that the surface of the steel bars can be visually examined during the test period and the results can be obtained in a reasonable time frame. All specimens were immersed in pore solution for 30 days and then 3 wt.% of laboratory grade NaCl was added to each cell. The pH of the solution was periodically measured during the experiment to ascertain the pH remained around 13.2. A three-electrode measurement setup, including a specimen as the working electrode, an SCE as the reference electrode, and a 316L stainless-steel sheet as the counter electrode, was used for the LPR (linear polarization resistance), CP (cyclic polarization) and CV (cyclic voltammetry) tests. All

electrochemical measurements were conducted at ambient temperature and cells were sealed during the experiment to minimize atmospheric carbonation effect.

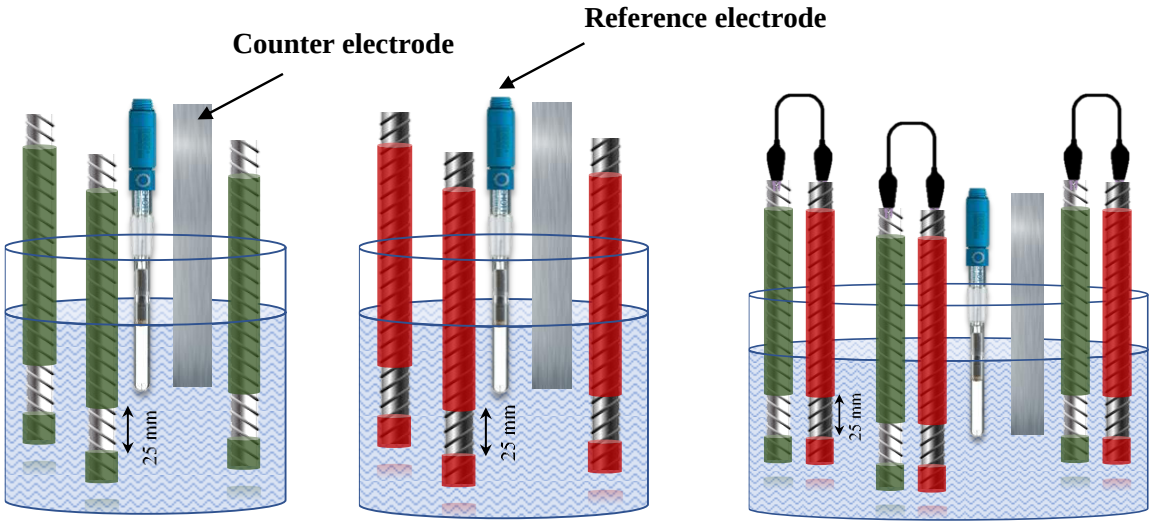

Figure 4-1. Schematic illustration of the measurement cells with (a) three specimens made with Steel A bars; (b) three specimens made with Steel B bars; and (c) coupled bars.

Table 4-2. The chemical composition of the concrete simulated pore solution.

Compound	Mol/L
NaOH	0.1
KOH	0.3
$Ca(OH)_2$	0.03
$CaSO_4.H_2O$	0.002

Corrosion potentials were measured every 24 h. To determine the corrosion current density of the specimens, LPR within the range of ±10 mV vs. corrosion potential with the scan rate of 0.166 mV/s [19] was conducted on all specimens every 2-3 days. ZRA (zero resistant amperometry) was used to determine galvanic current flow between two types of steel in the cell with coupled steel bars (Figure 1c). The test was carried out

for 1 h during each measurement. CP technique was carried out every week on one of the specimens in each cell to analysis the protectiveness of the passive film and pitting susceptibility of the specimens. This test started at -100 mV below the corrosion potential to +500 mV vs. SCE and then decreased to -100 mV below the corrosion potential with the scan rate of 0.166 mV/s. βc and βa (Tafel slopes) were extracted from CP results to calculated Stern-Geary values and subsequently corrosion current densities. CV was conducted to study oxidation and reduction behaviors of each specimen. The voltammograms were obtained between voltage limits of -1.4 V and +0.4 V vs. SCE at a linear sweep rate of 20 mV/s.

Result and Discussion

The image of the bulk specimen and microstructure of each type of steel are shown in Figure 4-2 and Figure 4-3. The microstructure of Steel A can be delineated distinctly into three regions. First, the outer layer corresponding to tempered martensite. Second, intermediate narrow bright ring comprised of the bainitic[1] transition zone and third, a comparably grey core consisted of the ferrite (light phase) and pearlite (dark phase). During manufacturing, due to water quenching process, first martensite formed at the outer layers (about 1.5 mm) and then inside residual heat flew outward, resulting in the formation of the tempering martensite; bainite formed at the narrow interface region

[1] *Bainite is a non-lamellar microstructure that forms in steels at temperatures of 250–550 °C*

between the tempered martensite and ferrite-pearlite core [12]. However, since just the outer layer of bars was exposed to the pore solution, the corrosion results just represented the behavior of the tempered martensite phase. As can be seen in Figure 4-3, Steel B had ferrite-pearlite phases in its microstructure.

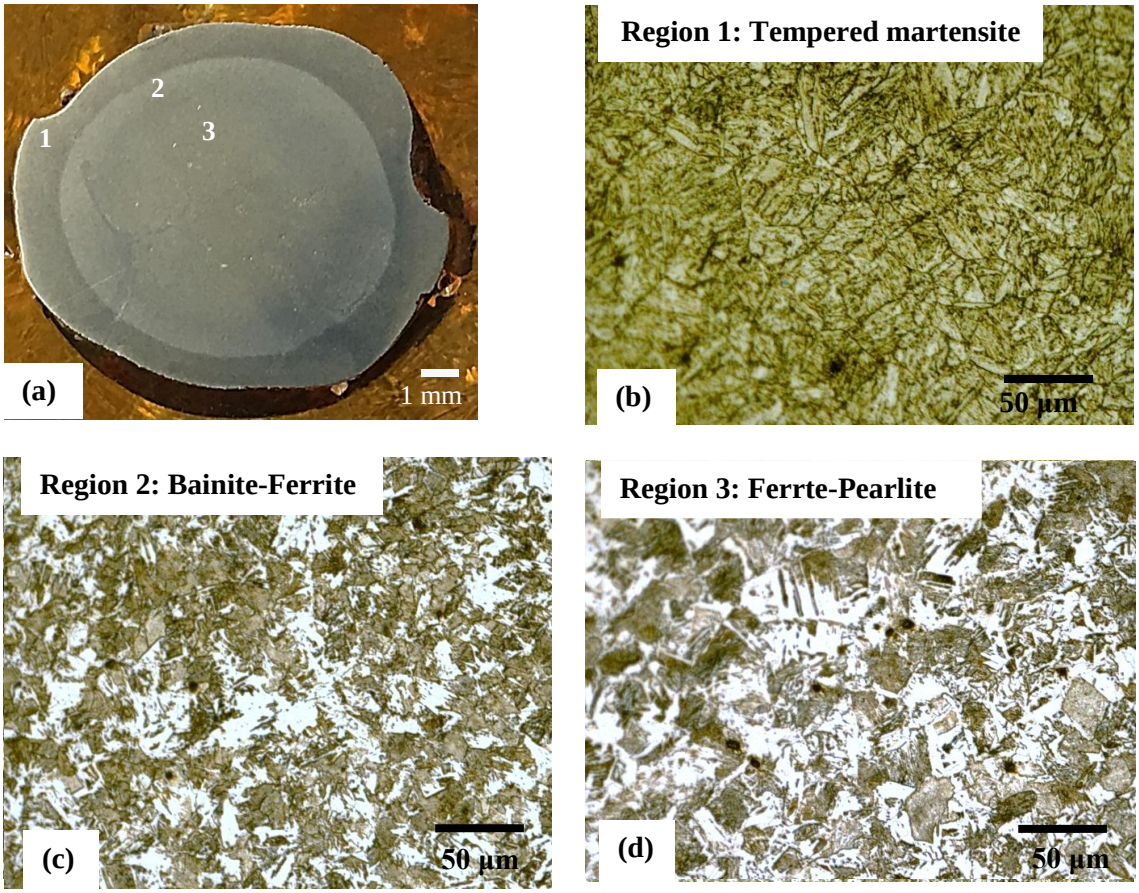

Figure 4-2. Images of Steel A: (a) photograph of the cross-section, (b) microstructure of the tempered martensite phase (region 1), (c) microstructure of the bainite-ferrite phase – transition zone (region 2), and (d) ferrite-pearlite phases (region 3).

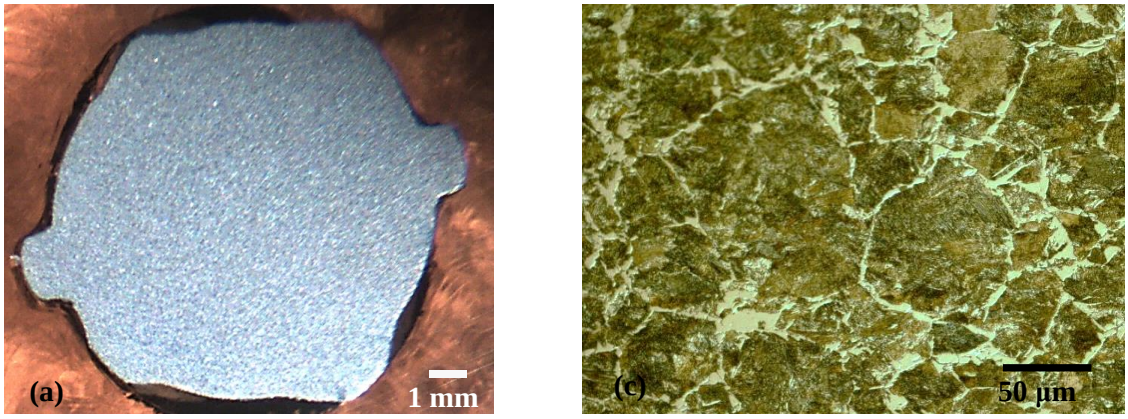

Figure 4-3. Images of steel B: (a) photograph of the cross-section, and (b) its microstructure (ferrite-pearlite phases).

The corrosion potential values of all individual and coupled specimens are shown in Figure 4-4. Specimens made with Steel A (tempered martensite phase) in the individual cell, showed lowest values of potentials during passivation (before adding salt) compared to the other specimens. On average, the potential values of Steel A specimens were approximately -270 mV vs. SCE after one month of exposure to chloride-free pore solution. After addition of 3 wt.% NaCl to the pore solution, these values decreased to around -480 mV vs. SCE. After about ten days they increased (gradually) to approximately -390 mV vs. SCE and remained relatively constant until the end of the experiment.

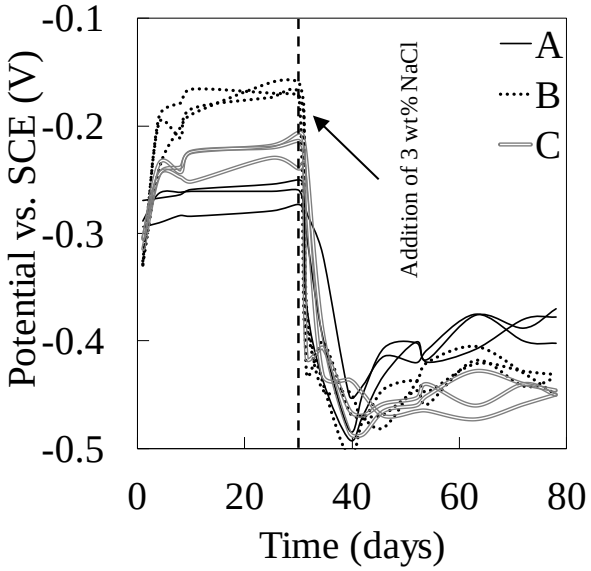

Figure 4-4. Images Corrosion potential values of the specimens. Dash line represents the time of addition of the NaCl.

The corrosion current densities obtained from the LPR tests are shown in Figure 4-5. These results corroborated the results from corrosion potential measurements. The sudden decrease of the potential values and increase in current densities, after addition of the salt, can be attributed to the dissolution of the passive layer [20]. The gradual increase of the potential values and a decrease of the current densities, 10 days after addition of the salt, can be ascribed as the accumulating of corrosion products on the surface which can act as a protective film [21]. However, a slight decrease in corrosion current densities or decrease in potential, 10 days after addition of the salt, did not necessarily mean that the corrosion was ameliorated but it might become worse due to localized corrosion.

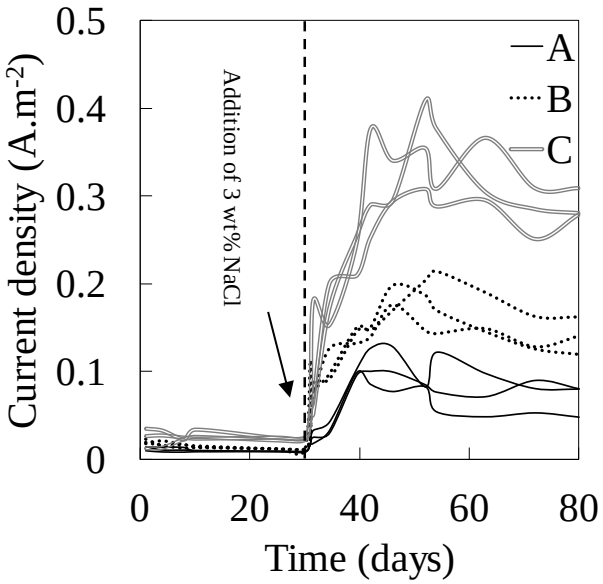

Figure 4-5. Corrosion current density values; salt added at 30th day of immersion. Dash line represents the time of addition of the NaCl.

Corrosion potential values for specimens made with Steel B increased intensely compare to specimens made with Steel A, during passivation time. This observation indicated that Steel B passivated faster and better compared to Steel A. After addition of the salt, the corrosion potential values and corrosion current densities of Steel B compared to Steel A stabilized in lower values and higher values, respectively, indicating less corrosion activity of Steel A compared to Steel B.

Alloying element may be involved in this behavior. For example, Cu, even in low quantity (i.e. less than 0.2 wt.%), showed a beneficial effect of increasing the corrosion resistance due to enhancing the formation of a very thin protective oxide film on the surface of the steel [14]. In addition, the presence of copper improves the formation of a homogenous layer of packed α-FeOOH (goethite), which can hinder the diffusion of chloride ions to steel and retard the corrosion [10, 11, 21, 22]. Furthermore, Steel A had more carbon and coarser microstructure compared to Steel B which reduced their ability

to form a uniform and compact protective layer. Without proper alloying elements and microstructure, Fe^{2+} in the inner oxide film, exposed to the corrosive medium, can transform to Fe^{3+} which is none-protective [23].

After addition of the salt, the corrosion potential values of the coupled steel specimens were slightly more negative, than the values for the specimens in two individual cells. In addition, coupled cells showed more corrosion current densities compared to the individual cells (Figure 4 5). Furtheremore, Results from the ZRA tests (Figure 4-6) shows that the galvanic electron flowed from the specimens made of Steel A to the specimens made with Steel B in the coupled cell. This current was increased after addition of the salt, indicating an increase of corrosion activity in Steel A and a decrease of the corrosion activity in Steel B in the coupled specimens.

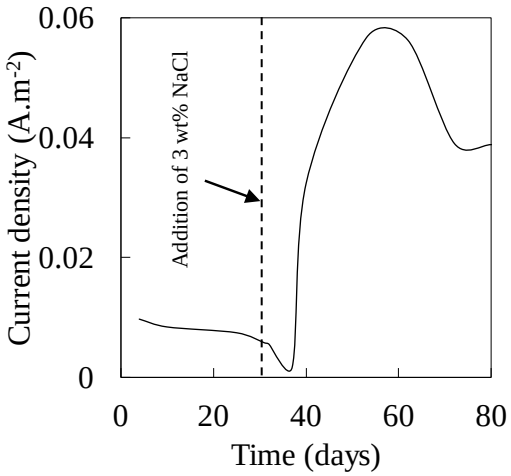

Figure 4-6. Galvanic current vs. time, obtained from the ZRA test on coupled specimens in cell M, salt added at 30th day of immersion. Dash line represents the time of addition of the NaCl.

The mixed potential theory can elucidate this behavior [24, 25]. As above-mentioned, when the specimens were in chloride-free pore solution, Steel A showed

lower corrosion potential values compared to Steel B (Figure 4-4). Figure 4-7 shows Evans diagrams obtained from the last day of the immersion in chloride-free pore solution. Passivation is an anodic process and a specimen needs to be polarized in the anodic direction to passivate. However, as can be seen, Steel B acted as the cathode and polarized Steel A in an anodic direction; meaning electrons flew from Steel A to Steel B did not allow Steel B reacting with pore solution and completely passivate. The overall behavior of the polarization of a galvanic cell can be extracted by the intersection of two individual diagrams, in this case, Steel A and Steel B. Steel A and Steel B were mainly involved in the anodic and cathodic portions, respectively. It should be noted that the galvanic behavior also depends on other factors such as geometry, surface area ratio and mass transport [24].

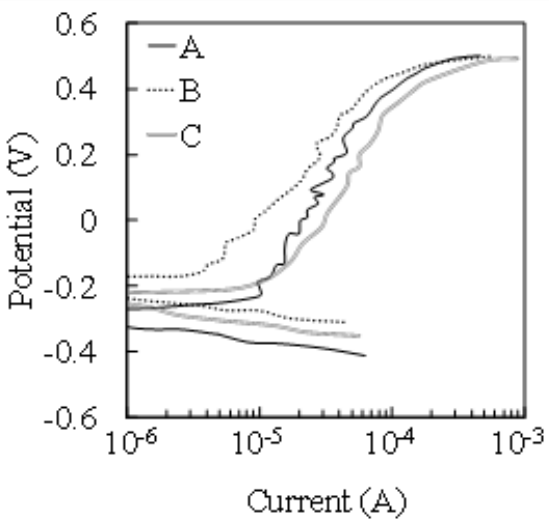

Figure 4-7. Polarization diagrams of Steel A and Steel B in after 30 days exposure to chloride-free pore solution.

However, since in this experiment these parameters were similar for both specimens in the coupled cell, the galvanic behavior in this experiment can only be

attributed to the different microstructures in the steel specimens. As the results shown in Figure 4 confirmed, the corrosion potential of connected specimens (C series) lays between corrosion potential of two type of steel. Also, its cathodic and anodic behavior of connected cell (Figure 4-7) is close what was expected.

Figure 4-8 shows the results of the CP test, conducted 21 days after addition of the NaCl to the pore solution. Results indicated that pitting corrosion occurred on all specimens. Steel A, had the lowest current density in each potential, but in reverse scan, it had the largest hysteresis loop among other specimens that indicated more susceptibility to pitting corrosion. The coupled specimens showed higher current densities compared to Steel A series while the size of their hysteresis loop was smaller than other steels, indicated more localized corrosion incurred by the steels when they were coupled compared to the individual specimens.

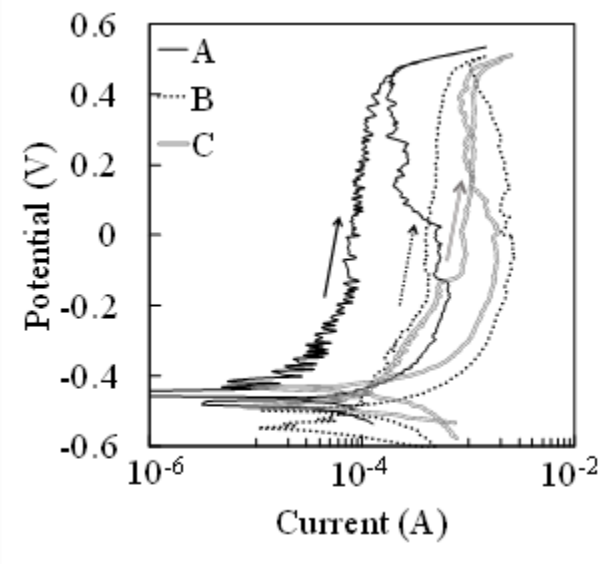

Figure 4-8.Results of the cyclic polarization tests conducted on one of the specimens in each cell, 21 days after addition of the NaCl to the pore solution.

To show the impact of coupling on the corrosion behavior of the specimens, one of the coupled specimens (21 days after addition of the salt) was disconnected and CP test was conducted 1 h after disconnection. Figure 4-9a shows the results of the CP tests on the uncoupled Steel A and Steel A in one an individual cell (not coupled). As can be seen, in each overpotential, anodic current densities increased for uncoupled Steel A compared to the Steel A in the individual cell. Additionally, sharper breakdown points and larger negative hysteresis loop were observed for the disconnected Steel A in the coupled cell compared to the Steel A in the individual cell.

This behavior is completely different for Steel B (Figure 4-9b). Disconnected specimen from the coupled cell had a lower current density in each overpotential compared to Steel B in the individual cell. In addition, the direction of the hysteresis loop was opposite of that in the individual specimens, indicating that Steel B (pearlite-ferrite) still had the tendency be passivated in chloride contaminated-pore solution.

Figure 4-9c shows the results of the CP tests on the disconnected Steel A and disconnected Steel B 1 h after disconcertion, and the coupled specimens. Clearly, coupling the steels changed their corrosion behavior. Particularly, the size of the hysteresis loop on the coupled specimens decreased significantly compared to the

disconnected ones, showing an increase of the amount on pitting corrosion in the coupled specimens.

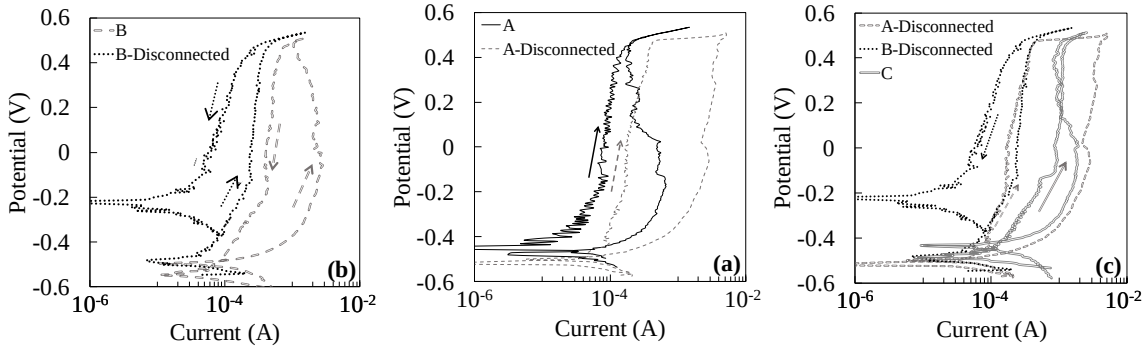

Figure 4-9.Results of the CP test, 21 days after addition of the NaCl to the pore solution (a) disconnected Steel A and Steel A in the individual cell, (b) disconnected Steel B and Steel B in the individual cell, and (c) disconnected Steel A, disconnected Steel B, and coupled steels.

Figure 4-10 shows the results of the CV tests. There were no considerable differences between the voltammogram of Steel A and Steel B in individual cells, except the position of Peak A. Although the mechanism of formation of oxide layers was not fully identified, it was hypothesized that these anodic peaks represented the successive formation of the FeOOH and Fe_2O_3 in the outer layer of the oxide film [23,26,27]. Comparisons between steels in individual cells with their disconnected counterparts in the coupled cell are shown in Figure 4-10 b and c. The position of Peak A, as well as its intensity, increased in each cycle in the disconnected specimens for both steels, indicating occurrence of more oxidation activity on those specimens compared to the steels in individual cells.

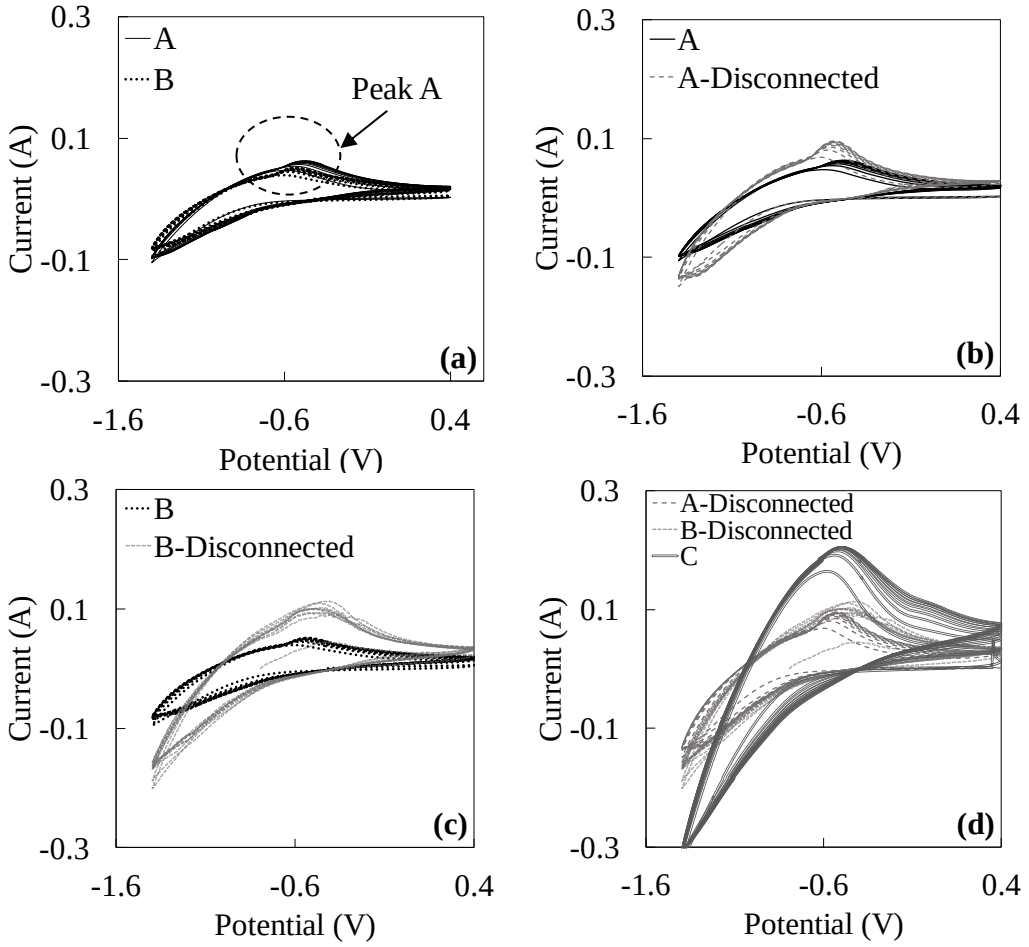

Figure 4-10. CV data from 21st day of adding salt in pore solution from different steel specimens (a) Steel A and Steel B in individual cells (b) Steel A in individual cell and disconcerted Steel A in a coupled cell (c) Steel B in individual cell and disconcerted Steel B in a coupled cell (d) disconnected with coupled specimens.

Nonetheless, Peak A in the voltammogram of the coupled steels, showed higher current compared to the disconnected steels. This observation indicated the significance of coupling on increasing the corrosion activity on the steel specimens. By passing each cycle, the anodic current peak increased, signifying that the inner oxide film allowed passing more iron ions into the outer oxide film to get oxidized. This behavior mostly resembled disconnected Steel A.

The total mass loss during the entire experiment for each specimen was calculated using the current densities from the LPR test and the Faraday's law [28] and the results are shown in Figure 4-11. Note that this mass loss did not consider the localized nature (pitting) of the corrosion. As it can be seen, Steel A in the individual cell, had lower mass loss compared to Steel B. Nevertheless, the coupled specimen showed the highest mass loss compared to the individual specimens. The mass loss in the coupled specimens was about 360% of Steel A and 180% of Steel B in the individual cells. The mass loss of the disconnected Steel A in the coupled cell was more than that for the Steel A in the individual cell. This observation showed that Steel A sacrified itself to protect Steel B in the coupled cell.

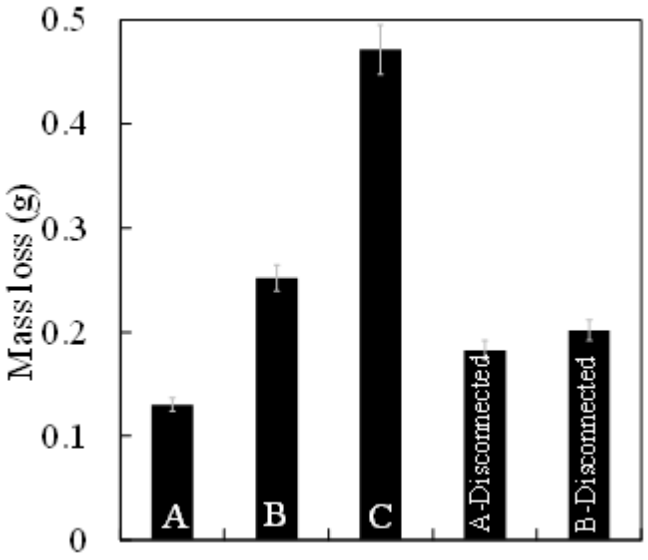

Figure 4-11. The calculated average mass loss for the specimens during the entire time of exposure.

Optical microscopy and the scanning electron microscopy (SEM) were conducted on the specimens at the end of the experiment to study the microstructure and the surface condition of the steels as well as the corrosion products formed on the surface of the specimens. For Steel A in both cases (Figure 4-12), i.e. individual and coupled cells, corrosion was mostly observed in the form of localized (pits or accumulated particles) corrosion. On Steel B, Figure 4-13, the corrosion products were formed in larger areas, compared to Steel A. The SEM images showed the globular morphology of the pits along with some cracks in congested corrosion product region for both of steels (Figure 4-12d and Figure 4-13d). Since specimens had a ferrous base, the corrosion products were same, i.e., oxides or hydroxides of iron. Nevertheless, the size of these globular areas was much larger in Steel A compared to Steel B, indicating more severe localized dissolution in Steel A compared to that in Steel B.

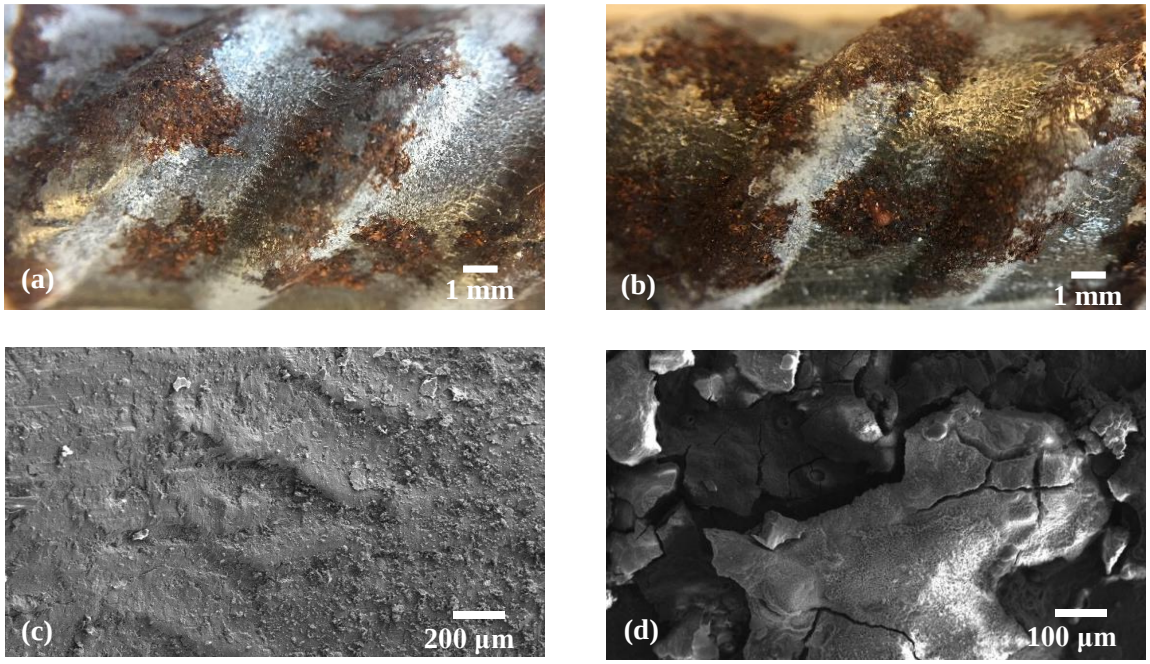

Figure 4-12. Optical micrograph of corroded surfaces of one of the specimens of (a) Steel A in the individual cell, (b) Steel A in the coupled cell, (c) SEM image of Steel A in the individual, and (d) SEM

image from a pit on the surface of Steel A in the coupled cell.

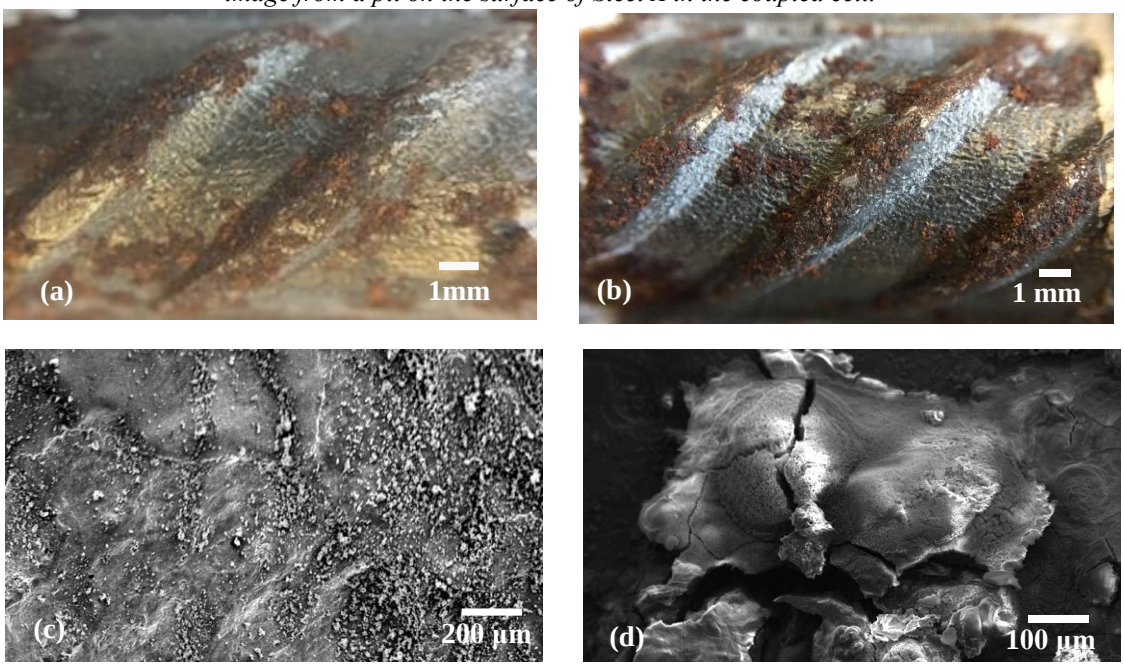

Figure 4-13. Optical micrograph of corroded surfaces of one of the specimens of (a) Steel B in individual cell, (b) Steel B in coupled cell, (c) SEM image of Steel B in the individual cell, and (d) SEM image from a pit on surface of Steel B in the coupled cell.

Conclusions

The galvanic connection between thermomechanical treated steel (Steel A) and conventional steel (Steel B) in chloride-contaminated concrete pore solution led to significant increase in the corrosion activity of the steel specimens. Individual thermomechanical treated steel specimens showed superior corrosion resistance compared to the conventional steel specimens. When coupled, the conventional steel showed better passivation compared to the thermomechanical treated steel in chloride-free pore solution; In chloride-contaminated pore solution, when thermomechanical

treated steel was coupled with the conventional steel, they became the anode and their corrosion activity increased compared to the conventional steel. Morphology of corrosion products of both steels was similar. However, the corrosion products formed on the thermomechanical treated steel was mostly fragmented while the conventional steel showed relatively continuous corrosion products.

References

[1] M.K. Ravikumar, T.S. Balasubramanian, a. K. Shukla, S. Venugopalan, A cyclic voltammetric study on the electrocatalysis of alkaline iron-electrode reactions, J. Appl. Electrochem. 26 (1996) 1111–1115. doi:10.1007/BF00243735.

[2] Y. Zhang, Study on corrosion activity of carbon steel in concrete simulated pore solution under static tensile and compressive, (2012).

[3] G.P. Kalaignan, V.S. Muralidharan, K.I. Vasu, Triangular potential sweep voltammetric study of porous iron electrodes in alkali solutions, J. Appl. Electrochem. 17 (1987) 1083–1092. doi:10.1007/BF01024374.

[4] E. Volpi, A. Olietti, M. Stefanoni, S.P. Trasatti, Electrochemical characterization of mild steel in alkaline solutions simulating concrete environment, J. Electroanal. Chem. 736 (2015) 38–46. doi:10.1016/j.jelechem.2014.10.023.

[5] A. Poursaee, C.M. Hansson, Reinforcing steel passivation in mortar and pore solution, Cem. Concr. Res. 37 (2007) 1127–1133. doi:10.1016/j.cemconres.2007.04.005.

[6] A. Poursaee, Corrosion of steel bars in saturated Ca (OH) 2 and concrete pore

solution, Concr. Res. Lett. 1 (2010) 90–97.

[7] P. Ghods, O.B. Isgor, G.A. Mcrae, G.P. Gu, Electrochemical investigation of chloride-induced depassivation of black steel rebar under simulated service conditions, Corros. Sci. 52 (2010) 1649–1659. doi:10.1016/j.corsci.2010.02.016.

[8] A. Islam, Corrosion behaviours of high strength TMT steel bars for reinforcing cement concrete structures, Procedia Eng. 125 (2015) 623–630. doi:10.1016/j.proeng.2015.11.084.

[9] B.K. Panigrahi, S. Srikanth, G. Sahoo, Effect of alloying elements on tensile properties, microstructure, and corrosion resistance of reinforcing bar steel, J. Mater. Eng. Perform. 18 (2009) 1102–1108. doi:10.1007/s11665-008-9336-z.

[10] S.K. Nandi, N.K. Tewary, J.K. Saha, S.K. Ghosh, Microstructure, mechanical properties and corrosion performance of a few TMT rebars, Corros. Eng. Sci. Technol. 51 (2016). doi:10.1080/1478422X.2016.1141744.

[11] L. Ding, A. Poursaee, The impact of sandblasting as a surface modification method on the corrosion behavior of steels in simulated concrete pore solution, Constr. Build. Mater. 157 (2017) 591–599. doi:10.1016/j.conbuildmat.2017.09.140.

[12] R.B. Figueira, A. Sadovski, A.P. Melo, E. V. Pereira, Chloride threshold value to initiate reinforcement corrosion in simulated concrete pore solutions: The influence of surface finishing and pH, Constr. Build. Mater. 141 (2017) 183–200. doi:10.1016/j.conbuildmat.2017.03.004.

[13] B.K. Panigrahi, S.K. Jain, Impact toughness of high strength low alloy TMT reinforcement ribbed bar, Bull. Mater. Sci. 25 (2002) 319–324. doi:10.1007/BF02704125.

[14] O. Kelestemur, M.H. Kelestemur, S. Yildiz, Improvement of Mechanical Properties of Reinforcing Steel Used in the Reinforced Concrete Structures, J. Iron Steel Res. Int. 16 (2009) 55–63. doi:10.1016/S1006-706X(09)60044-3.

[15] S. Alimoradi, R. Faraj, A. Torabian, Effects of residual aluminum on hybrid membrane bioreactor (Coagulation-MBR) performance, treating dairy wastewater, Chem. Eng. Process. - Process Intensif. 133 (2018) 320–324. doi:10.1016/j.cep.2018.09.023.

[16] P. Niksiar, M.B. Frank, J. McKittrick, M.M. Porter, Microstructural evolution of paramagnetic materials by magnetic freeze casting, J. Mater. Res. Technol. 8 (2019) 2247–2254. doi:10.1016/j.jmrt.2018.12.024.

[17] C.T. Properties, Standard Specification for Low-Alloy Steel Deformed and Plain Bars for Concrete, (2019) 9–14. doi:10.1520/A0706.

[18] S. Specification, Standard Specification for Deformed and Plain Carbon-Steel Bars for Concrete Reinforcement, Annu. B. ASTM Stand. (2016) 1–8. doi:10.1520/A0615_A0615M-16.

[19] A. Poursaee, Determining the appropriate scan rate to perform cyclic polarization test on the steel bars in concrete, Electrochim. Acta. 55 (2010) 1200–1206. doi:10.1016/j.electacta.2009.10.004.

[20] H. Tamura, The role of rusts in corrosion and corrosion protection of iron and steel, Corros. Sci. 50 (2008) 1872–1883. doi:10.1016/j.corsci.2008.03.008.

[21] W. Chen, R.G. Du, C.Q. Ye, Y.F. Zhu, C.J. Lin, Study on the corrosion behavior of reinforcing steel in simulated concrete pore solutions using in situ Raman spectroscopy assisted by electrochemical techniques, Electrochim. Acta. 55 (2010) 5677–5682.

doi:10.1016/j.electacta.2010.05.003.

[22] M.G. Jeon, R.T. Leon, Effect of Reinforcing Bar Chemical Composition on Corrosion Resistance, (1994).

[23] P. Ghods, O. Burkan Isgor, F. Bensebaa, D. Kingston, Angle-resolved XPS study of carbon steel passivity and chloride-induced depassivation in simulated concrete pore solution, Corros. Sci. 58 (2012) 159–167. doi:10.1016/j.corsci.2012.01.019.

[24] J. Oldfield, Electrochemical theory of galvanic corrosion, Galvanic Corros. (1988) 18. doi:10.1520/STP26188S.

[25] C.M. Abreu, M.J. Cristóbal, M.F. Montemor, X.R. Nóvoa, G. Pena, M.C. Pérez, Galvanic coupling between carbon steel and austenitic stainless steel in alkaline media, Electrochim. Acta. 47 (2002) 2271–2279. doi:10.1016/S0013-4686(02)00086-5.

[26] R.D. Hable, S. Alimoradi, B.S.M. Sturm, S.M. Stagg-Williams, Simultaneous solid and biocrude product transformations from the hydrothermal treatment of high pH-induced flocculated algae at varying Ca concentrations, Algal Res. 40 (2019) 101501. doi:10.1016/j.algal.2019.101501.

[27] W. Wang, H. Chen, X. Li, Z. Zhu, Corrosion behavior of steel bars immersed in simulated pore solutions of alkali-activated slag mortar, Constr. Build. Mater. 143 (2017) 289–297. doi:10.1016/j.conbuildmat.2017.03.132.

[28] A. Poursaee, Corrosion of steel in concrete structures, 1st ed., Woodhead Publishing, 2016. doi:10.1016/B978-1-78242-381-2.00002-X.

CHAPTER 5

Study of effect of phase distribution of reinforcement steel microstructure against chloride ion depassivation in concrete pore solution

Introduction

Premature corrosion of reinforcing steel bars in concrete is the major reason of deterioration in such structures [1,2]. Steel bars initially are protected by a protective passive film, formed in alkaline environment of concrete. However, in a critical chloride content, i.e. chloride threshold (C_{crit}), this passive film breaks down, corrosion initiates and propagates leading to damage [3,4]. Chloride threshold, C_{crit}, is defined as the minimum amount of chloride required to break down the passive film and initiate corrosion [1,5-10]. This value is influenced by the level of stress [11,12], chemistry and chloride activity of the environment [8–10,13–19], steel / concrete interface [18,20,21], and the surface condition and metallurgy of the reinforcement [6,19,22–30].

Studies were conducted on modification of the steel surface or composition to tackle the damage of corrosion by applying coating [31–33], cladding and alloying procedure [30,34–36]. However, most of these procedures require huge changes in design and manufacturing process that is not cost-effective options in many cases. Comprehensive studies were devoted to broadening understanding of the electrochemical characterization of the passivation and break down of the passive film on the carbon steel

in simulated concrete environment [37–46]. There is a significant gap in corrosion research addressing the influence of phases and microstructure on passivation and corrosion of steel in concrete environment [19,23,29].

The main purpose of this work was to understand the role of steel microstructure and phases on passivation and break down of the passive film, i.e. chloride threshold value. The microstructure of steel was modified through different heat treatment processes. Different electrochemical tests were conducted, and passivation and the chloride threshold values of each group were studied in simulated concrete pore solution.

Materials and Experimental Procedures

Steel specimens with the length of 10 mm were cut from #12 reinforcing low-alloy steel bar (ϕ ~12.7 mm) with the nominal allying elements of (in wt.%) 0.39 C, 1.30 Mn, 0.15 Si, 0.03 Cu, 0.02 P, 0.01 S and Fe for balance. Two heat treatment routes as illustrated in Figure 5-1 were used to obtain different microstructures compare to as-received (reference, R) specimens. For Route 1, first specimens were heated to 1020 ^{o}C and kept for 1 h that produced 100% austenite phase. Then, they air cooled to room temperature. Route 2 consisted of two parts. In part 1, specimens were heated to 820 ^{o}C and kept for 1 h, then air-cooled to room temperature. In part 2, specimens were tempering at 720 ^{o}C for 30 min, then air- cooled to room temperature. The obtained specimens from Route 1 and 2 were labeled as N and C, respectively.

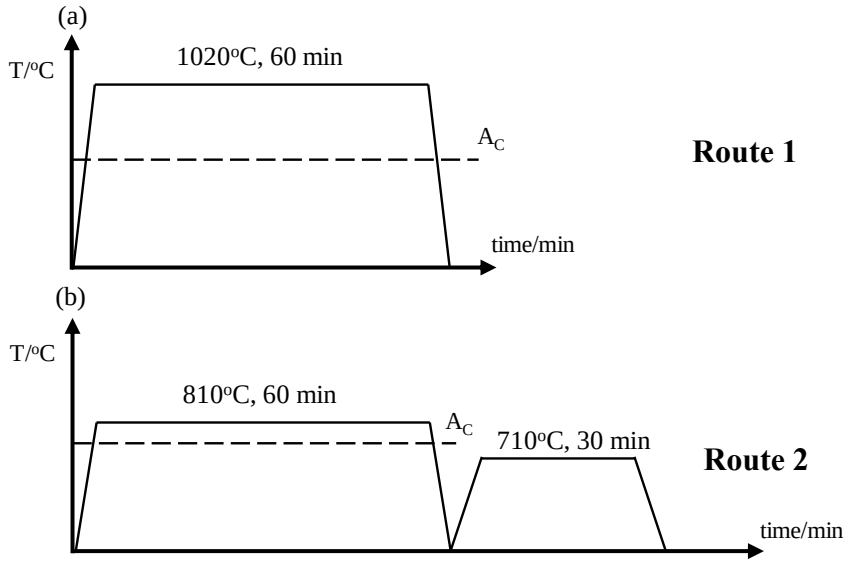

Figure 5-1. Heat treatment routes used in the study.

Subsequently, all specimens were cleaned from oxides and mounted in two-part high-shrinkage epoxy. The bottom of each mounted specimen was drilled, and a copper wire was inserted and glued in the hole of each mounted specimen for the required electrical connection. To assure reproducibility of experimental results, three identical specimens of each microstructure were prepared.

For the electrochemical tests all specimens were wet grounded sequentially using #80 to #1000 grit SiC paper, then washed with mixed deionized water and ethanol, and dried immediately. For microscopic observations, the mounted specimens polished with 1 μm alumina powder slurry and etched in 4% nital solution.

Concrete simulated pore solution, with the composition given in Table 5-1, was used as the electrolyte in all electrochemical experiments [15].

Table 5-1. The chemical composition of the concrete simulated pore solution.

Compound	mol/L
NaOH	0.1
KOH	0.3
$Ca(OH)_2$	0.03
$CaSO_4.H_2O$	0.002

All measurements were performed at room temperature (~25 ^oC). The pH of the solution was measured every 12 h during the experiments to assure that the pH remained at 13.2. To avoid carbonation and evaporation, all containers were sealed throughout the whole experiment.

To measure the chloride threshold values, the method suggested by Hurley and Scully was adapted and used in this investigation [6]. Accordingly, conservative upper bound of passive potential of 0.2 V vs SCE determines the chloride threshold concentration when stabilized cut-off anodic current density drastically jumps to higher values [6]. Accordingly, immediately after preparation, all the specimens were immersed in chloride-free pore solution for 3 days to reach stability and then passivated at biased potential of 0.2 for 1 day [45,47]. The current density was recorded continuously, using Pt gauze as counter-electrode. Afterwards, NaCl was added to the electrolyte (i.e. pore solution) with the increments of 0.05 M per 12 h. A sudden increase in the current density was attributed to the breakdown of the passive and consequently, the chloride threshold value. The polarization of steel in alkaline media is a strong function of time, thus in this study for each increment of chloride addition, 12 h, was given to system to reach steady state [45,47–49].

In different experiment, cyclic voltammetry (CV) was conducted to study the surface oxidation and reduction behavior with respect to the potential. Voltammograms of specimens were obtained in chloride-free pore solution with repetitive scans from -1.4 V vs. SCE (close to hydrogen evolution potential) to +0.5 V vs. SCE (close to oxygen evolution potential) [40] at 10 mV/s scan rate.

After the determining the threshold value for each group of specimens, to reveal the corrosion on the surface of the corrosion of each phase in the microstructure, propagation, post-corrosion microscopic evaluation was conducted on the electrochemically tested specimens by removing corrosion products in boiling 200 g/L CrO_3 and 10 g/L $AgNO_3$ solution., Then, specimens were slightly polished and etchedin 4% v/v nital solution.

Result and Discussion

Pre-Corrosion Microstructural Evaluation

Three-dimensional cross-section optical micrograph and SEM images of the heat-treated and reference (as-received) specimens are shown in Figure 5-2 and Figure 5-3, respectively. The images from optical microscopy show that all specimens consisted of , ferrite and pearlite phases. However, SEM images revealed more details compared to the optical micrographs. The N specimen (Route 1), Figure 5-3 (a), mainly composed of

perlite with narrow traces of proeutectoid ferrite, which appears as dark phases, at primary austenite grains. Within the range of time and temperature of normalizing, the whole microstructure, including ferrite and pearlite, transformed to austenite, and primary austenite grains started to growth [50]. As a result of intermediate cooling rate, i.e. air cooling, Widmanstatten ferrite formed, with sporadic narrow equiaxed ferrite at coarsened primary austenite grain boundaries. As shown in Figure 5-3, Route 1 generated coarser microstructure compared to the reference specimens.

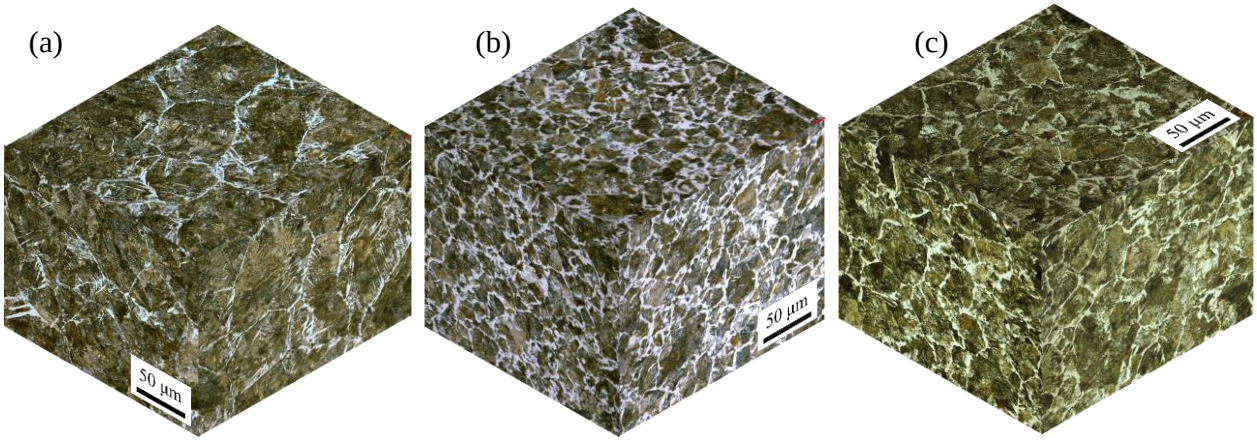

Figure 5-2. three-dimensional optical micrograph of examined steel bar. (a) N, (b) C and (C) R series.

In contrast, processing through Route 2 (C series), yielded to coarser and greater portion of proeutectoid ferrite compared to the the other sets of specimens. Holding specimens at 810 ºC for 60 min, transformed pearlite to austenite, whereas initial proeutectoid ferrite remained stable. Subsequently, greater amount of carbon permeated to austenite and formed interconnected proeutectoid ferrite [50]. Within second step of

Route 2, i.e. tempering at 30 min. at 710 ºC, below the eutectoid temperature, ferrite within interlamellar retained pearlite broke and relatively spheroidized pearlite [51] formed compare to the reference specimen as shown in Figure 5-3 (b) and (c). The volume fraction of the proeutectoid ferrite and hardness obtained from ten different image analysis and Vickers measurements are listed in Table 5-2. Both heat treatment routs softened the steel. Softening in Route 1 was attributed to the coarsening of the primary grain boundaries. and the negligible softening in Route 2 was credited to the stress relief, recovery and phase transformation of hot deformed reference specimen.

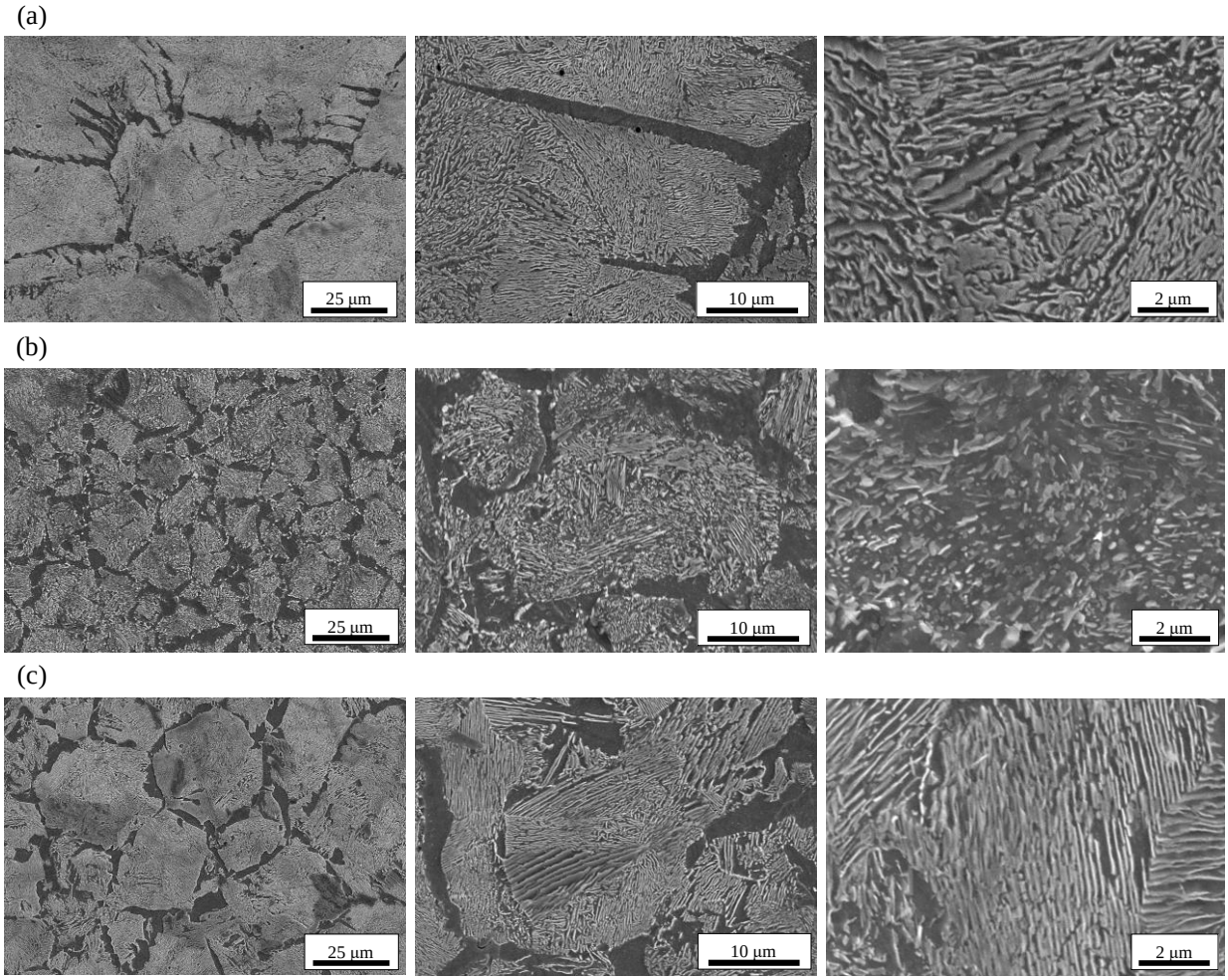

Figure 5-3. SEM micrographs of examined steel bar in different magnifications. (a) N, (b) C and (C) R series.

Table 5-2. Proeutectoid ferrite ferrite portion of as-received and heat-treated steel rebar.

Sample	R	N	C
Proeutectoid ferrite (%)	10	6.5	21
Hardness (HV)	259	238	251

Electrochemical Examinations

Figure 5-4 shows first ten cyclic voltammograms scans of specimens with three different microstructures, immersed in chloride-free pore solution for 3 days. The anodic peaks I and the cathodic peaks IV are assigned to the oxidation and reduction processes

between Fe^0 and Fe^{II} forming $Fe(OH)_2$ or FeO. Peaks II and III are attributed to the redox process for Fe^{III} and formation of Fe_3O_4 (magnetite) from either $Fe(OH)_2$, FeO or Fe^0 [8,40].

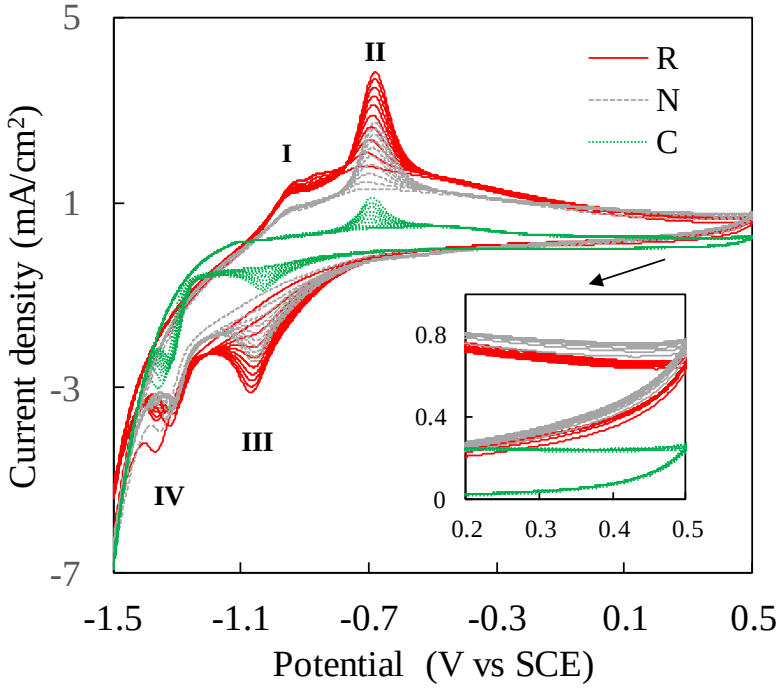

Figure 5-4. Cyclic voltammograms of reference and heat-treated specimens immersed in pore solution for 3 days.

According to the point defect model, the passivity domain can be determined where current is relatively constant with increasing applied anodic potential [16–18]. As shown in Figure 5-4, this range was between approximately +0.2 to +0.5 V vs. SCE for all specimens. Cyclic voltammograms obtained at 50, 20, 5 and 2 mV/s also indicated the same range and similar peaks. Results presented here, are in agreement with previous investigations [18–21]. Accordingly, choosing +0.2 V vs. SCE as upper bound limit as the passive film breakdown potential [22], where the barrier and the deposit films both

contributed to the diffusion process space charge, seemed to be appropriate.

Apparently, greater peaks in forward reduction scan led to greater peaks in reverse scan for the oxidation. The specimen is C group showed shorter oxidation peaks compared to N and R specimens, due to slower oxidation kinetics on its surface compared to the other specimens. In addition, even in higher anodic potentials, a narrower hysteresis can be observed in the specimen from C group probably due to less capacitive behavior within the space charge layer of this specimen compared to other specimens [8,54,55]. The specimen from N group showed comparatively shorter oxidation and reduction peaks compared to the R specimen implying lower surface energy [56,57] presumably due to release of residual stress and formation of more stabilized phases in this specimen compared to the specimen from R group [58]. However, the ultimate current values recorded for specimen from N group in passive region (i.e. +0.2 V to +0.5 V vs. SCE) was lower than that for the specimen from R group R. This behavior implies that higher or lower oxidation rate in the passivating environment does not necessarily enhance the protectivity in the passive film [41–43]. In Contrast, the nature of the substrate, i.e. the microstructure, as catalyzer plays important role for adsorption and desorption of ions, such as OH^-, in alkaline solution [41,59].

Figure 5-5 shows the results of the EIS tests on specimens charged at stationary anodic

potential of +0.2 V vs. SCE in chloride free pore solution. The ohmic resistance of the solution was corrected in Bode plots [60]. Level of module of impedance in low frequencies increased in order of N > R > C, respectively. Due to inhomogeneous dispersion of physical properties along and normal to the passive film, constant phase element (CPE) is replaced with pure constant capacitive behavior in whole frequencies [61]. Two ranges of time constant can be observed from the phase angles (Figure 5-5c) as also previously reported by Joiret et al. for stationary steel with porous passive film in high alkaline solution[40]. High frequency range, i.e. > 100 Hz, was attributed to the dielectric properties of the solution/outer oxide layer and relaxation of double layer, while, the low frequency dielectric response, i.e. lower than 1 Hz was assigned to charge transfer and faradaic resistances at metal/hydroxide at bottom of porosities. Phase angle peak for N samples appears in lower frequencies which imply higher time constant and lower capacitance of double layer.

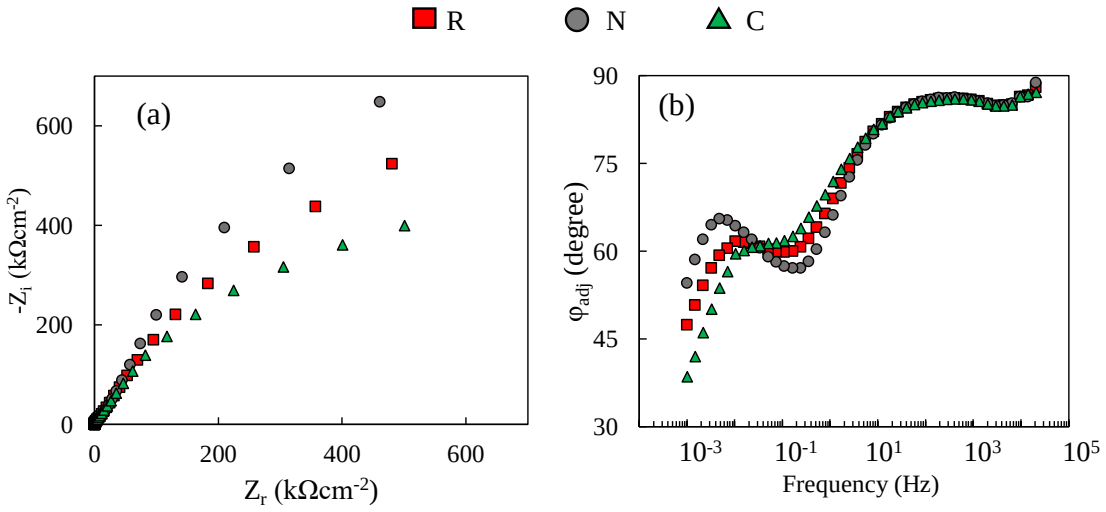

Figure 5-5. (a)Nyquist, (b) bode and (c) bode phase plots of EIS results of obtained after one day polarization of specimens at 0.2 V vs SCE in chloride free pore solution.

Results of measuring the chloride threshold value, C_{crit}, are shown in Figure 5-6. The values of C_{crit} for the N, and R and C groups were 0.8, 1.3, and 1.5 M, respectively. Normalizing of steel through route 1, severely reduced its C_{crit}. In chloride free and low levels of chloride contamination pore solutions, obtained anodic current is relatively lower for N series. However, with increasing amount of chloride, anodic current densities evolved passed the values obtained for C and R groups. This observation indicated the porosity and the defectiveness in the passive film formed on the surface of these specimens [49]. In contrast, specimens in C group remained passive until chloride concentration reached to 1.5 M.

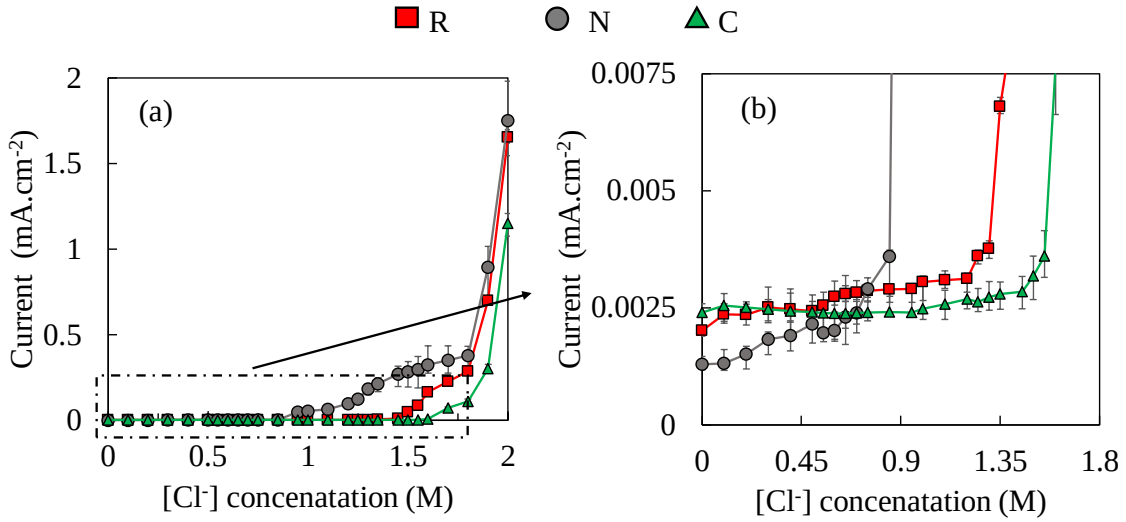

Figure 5-6. Resultant current density of steel with different microstructures immersed in pore solution and polarized at +0.2 V vs. SCE with respect to chloride concertation.

Figure 5-7 shows the SEM images of one specimen from each group, after corrosion initiation. As can be seen, pitting is mostly originated between ferrite and

pearlite boundaries and propagated through pearlite phase. It is well-known that the Cl^- locally adsorbs and competes with OH^- on the surface and accelerate the oxidation and reduction reactions, which ultimately yields breakdown of the passive film and pitting corrosion. The passive film formed on locations such as grain boundaries, different phases and inclusion boundaries is more prone to be attacked by the chloride ions compared to the passive film form on a uniform and homogeneous surface [29,62,63].

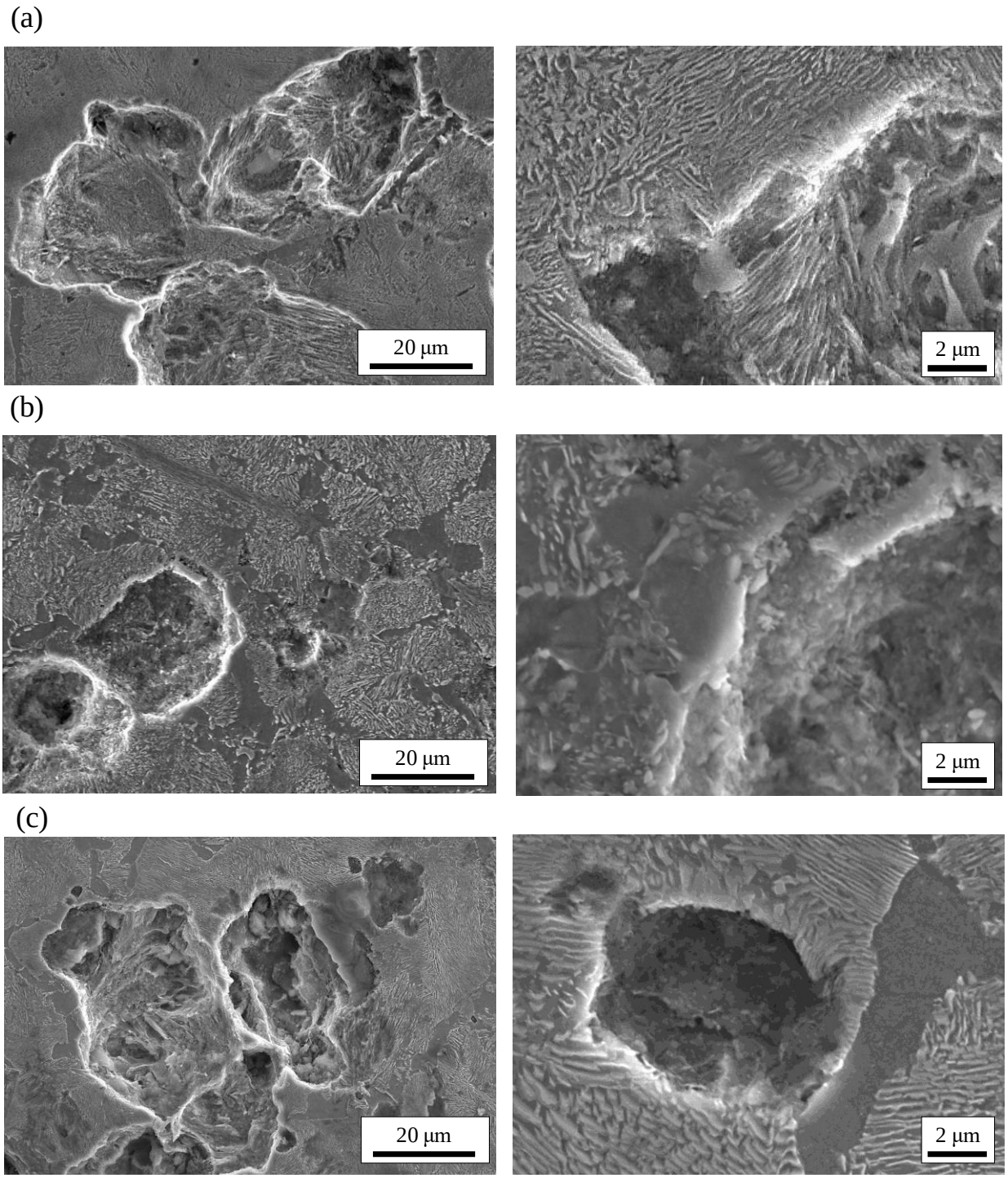

Figure 5-7. SEM micrographs of the specimens after corrosion initiation. Corrosion products were removed, and specimens were slightly polished and etched. (a) N, (b) C and (C) R series.

Cementite is more cathodic than ferrite [64-66]. It is hypothesized that the larger cathodic area in N specimens compared to the other specimens led to more adsorption of anions on their surface, as shown in the voltammograms (Figure 5-4). As a result, the discontinuity in passive film and lower C_{crit} in these specimens can be attributed to the pearlite phase and heterogenous distribution of potential and current between interlamellar cementite and ferrite. With increasing of $[Cl^-]/[OH^-]$, chloride preferentially adsorbed to the most defective area, i.e. at and around pearlite area, and triggered the development of pits. However, in C specimens, relatively broken and discontinued cementite in pearlite ameliorated corrosion resistance. In addition, continuous and higher amount of proeutectoid ferrite in C specimens compared to the other specimens, isolated the more vulnerable phase, i.e. pearlite, and confined deep pitting growth. The proposed mechanism is schematically depicted in Figure 5-8.

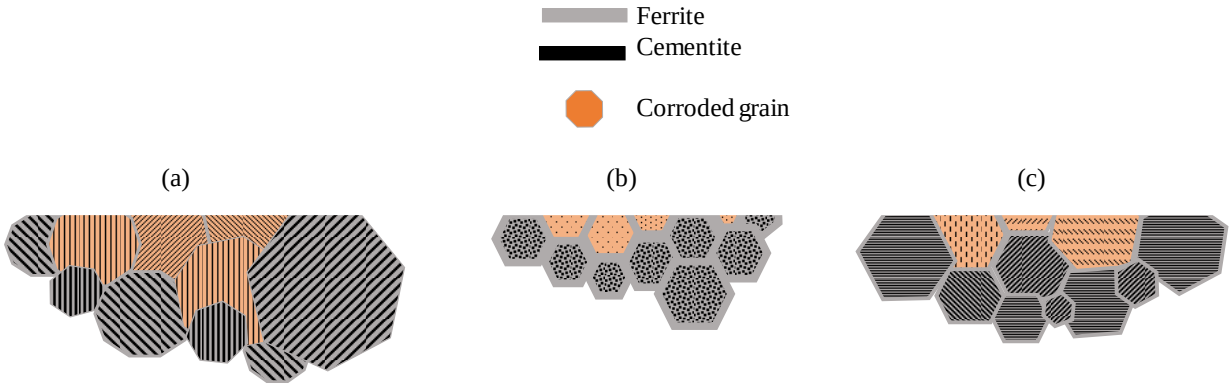

Figure 5-8. Schematic on mechanism of pitting growth on passivated reinforcement steel in pore solution (a) N series, (b) C series and (c) R series.

Conclusions

Based on the results from electrochemical and microscopic analyses, the

following conclusions can be drawn: Microstretches of steel can significantly alter its chloride threshold value in concrete pore solution. The measured chloride threshold values were 0.6, 1.4 and 1.6 for the N, R and C, respectively. Pearlite is the prone phase to pit initiation and corrosion propagation in simulated pore solution in carbon steel. Formation of discontinuous cementite and pearlite phases and greater portion of ferrite retard breakdown of the passive film and pit nucleation. Controlling phase morphology and distribution can potentially enhance the corrosion resistance of steel.

References

[1] A. Poursaee, Corrosion of steel in concrete structures, in: Corros. Steel Concr. Struct., Elsevier, 2016: pp. 19–33.

[2] U.M. Angst, Challenges and opportunities in corrosion of steel in concrete, Mater. Struct. 51 (2018) 1–20.

[3] H.S. Wong, Y.X. Zhao, A.R. Karimi, N.R. Buenfeld, W.L. Jin, On the penetration of corrosion products from reinforcing steel into concrete due to chloride-induced corrosion, Corros. Sci. 52 (2010) 2469–2480.

[4] C. Fu, N. Jin, H. Ye, X. Jin, W. Dai, Corrosion characteristics of a 4-year naturally corroded reinforced concrete beam with load-induced transverse cracks, Eval. Program Plann. 117 (2017) 11–23.

[5] U. Angst, B. Elsener, C.K. Larsen, Ø. Vennesland, Critical chloride content in reinforced concrete — A review, Cem. Concr. Res. 39 (2009) 1122–1138.

[6] M.F. Hurley, J.R. Scully, Threshold chloride concentrations of selected corrosion-resistant rebar materials compared to carbon steel, Corrosion. 62 (2006) 892–904.

[7] Y. Zhao, X. Zhang, W. Jin, Influence of environment on the development of corrosion product filled paste and a corrosion layer at the steel / concrete interface, Corros. Sci. 124 (2017) 1–9.

[8] S. Mundra, M. Criado, S.A. Bernal, J.L. Provis, Chloride-induced corrosion of steel rebars in simulated pore solutions of alkali-activated concretes, Cem. Concr. Res. 100 (2017) 385–397.

[9] A. Poursaee, A. Laurent, C.M. Hansson, Corrosion of steel bars in OPC mortar exposed to NaCl , MgCl 2 and CaCl 2 : Macro- and micro-cell corrosion perspective, Cem. Concr. Res. 40 (2010) 426–430.

[10] Y. Cao, C. Gehlen, U. Angst, L. Wang, Z. Wang, Y. Yao, Cement and Concrete Research Critical chloride content in reinforced concrete — An updated review considering Chinese experience, Cem. Concr. Res. 117 (2019) 58–68.

[11] D. Sidane, O. Devos, M. Puiggali, M. Touzet, B. Tribollet, V. Vivier, Electrochemical characterization of a mechanically stressed passive layer, Electrochem. Commun. 13 (2011) 1361–1364.

[12] Y. Zhang, A. Poursaee, Passivation and Corrosion Behavior of Carbon Steel in Simulated Concrete Pore Solution under Tensile and Compressive Stresses, 27 (2015) 1–9.

[13] P. Ghods, O.B. Isgor, G. McRae, T. Miller, The effect of concrete pore solution composition on the quality of passive oxide films on black steel reinforcement, Cem.

Concr. Compos. 31 (2009) 2–11.

[14] L. Li, a. a. Sagues, Chloride corrosion threshold of reinforcing steel in alkaline solutions - Open circuit immersion tests, Corrosion. 57 (2001) 19–28.

[15] S. Goni, C. Andrade, Synthetic concrete pore solution chemistry and rebar corrosion rate in the presence of chlorides, Cem. Concr. Res. 20 (1990) 525–539.

[16] G.K. Glass, B. Reddy, N.R. Buenfeld, The participation of bound chloride in passive ® lm breakdown on steel in concrete, 42 (2013) 2013–2021.

[17] U.M. Angst, B. Elsener, C.K. Larsen, Ø. Vennesland, Chloride induced reinforcement corrosion: Electrochemical monitoring of initiation stage and chloride threshold values, Corros. Sci. 53 (2011) 1451–1464.

[18] Z. Shi, M. Rica, K. De Weerdt, T. Anita, B. Lothenbach, F. Winnefeld, J. Skibsted, Cement and Concrete Research Role of calcium on chloride binding in hydrated Portland cement – metakaolin – limestone blends, Cem. Concr. Res. 95 (2017) 205–216.

[19] A. Poursaee, Temperature dependence of the formation of the passivation layer on carbon steel in high alkaline environment of concrete pore solution, Electrochem. Commun. 73 (2016) 24–28.

[20] J.A. González, E. Otero, S. Feliu, W. López, Initial steps of corrosion in the steel/Ca(OH)2 + Cl− system: The role of heterogeneities on the steel surface and oxygen supply, Cem. Concr. Res. 23 (1993) 33–40.

[21] G.K. Glass, N.R. Buenfeld, The inhibitive effects of electrochemical treatment applied to steel in concrete, Corros. Sci. 42 (2000) 923–927.

[22] D. Trejo, P.J. Monteiro, Corrosion performance of conventional (ASTM A615) and

low-alloy (ASTM A706) reinforcing bars embedded in concrete and exposed to chloride environments, Cem. Concr. Res. 35 (2005) 562–571.

[23] H. Torbati-Sarraf, A. Poursaee, Corrosion Improvement of Carbon Steel in Concrete Environment through Modification of Steel Microstructure, J. Mater. Civ. Eng. 31 (2019) 2–7.

[24] H. Torbati-Sarraf, A. Poursaee, Corrosion of coupled steels with different microstructures in concrete environment, Constr. Build. Mater. 167 (2018) 680–687.

[25] L.. Mammoliti, L.. Brown, C.. Hansson, B.. Hope, The influence of surface finish of reinforcing steel and ph of the test solution on the chloride threshold concentration for corrosion initiation in synthetic pore solutions, Cem. Concr. Res. 26 (1996) 545–550.

[26] L. Ding, A. Poursaee, The impact of sandblasting as a surface modification method on the corrosion behavior of steels in simulated concrete pore solution, Constr. Build. Mater. 157 (2017) 591–599.

[27] D. Song, A. Ma, W. Sun, J. Jiang, J. Jiang, D. Yang, G. Guo, Improved corrosion resistance in simulated concrete pore solution of surface nanocrystallized rebar fabricated by wire-brushing, Corros. Sci. 82 (2014) 437–441.

[28] A. Poursaee, C.M. Hansson, Reinforcing steel passivation in mortar and pore solution, Cem. Concr. Res. 37 (2007) 1127–1133.

[29] F. Zhang, J. Pan, C. Lin, Localized corrosion behaviour of reinforcement steel in simulated concrete pore solution, Corros. Sci. 51 (2009) 2130–2138.

[30] J.R. Scully, S.R. Sharp, Literature Review of Commercially Available Alloys That Have Potential as Low-Cost , Corrosion-Resistant Concrete Reinforcement, 66 (2010) 1–

13.

[31] A. Bautista, J.A. Gonzalez, Analysis of the protective efficiency of galvanizing against corrosion of reinforcements embedded in chloride contaminated concrete, Cem. Concr. Res. 26 (1996) 215–224.

[32] E. Ramirez, J.A. Gonzblez, A. Bautista, The protective efficiency of galvanizing against corrosion of steel in mortar and in Ca(OH)2 saturated solutions containing chlorides, Cem. Concr. Res. 26 (1996) 1525–1536.

[33] S. Pour-Ali, C. Dehghanian, A. Kosari, Corrosion protection of the reinforcing steels in chloride-laden concrete environment through epoxy/polyaniline-camphorsulfonate nanocomposite coating, Corros. Sci. 90 (2015) 239–247.

[34] H. Zheng, J. Dai, W. Li, C. Sun, Influence of chloride ion on depassivation of passive film on galvanized steel bars in concrete pore solution, Constr. Build. Mater. 166 (2018) 572–580.

[35] M.C. García-alonso, M.L. Escudero, J.M. Miranda, M.I. Vega, F. Capilla, M.J. Correia, Corrosion behaviour of new stainless steels reinforcing bars embedded in concrete, 37 (2007) 1463–1471.

[36] M.C. García-alonso, J.A. González, J. Miranda, M.L. Escudero, Corrosion behaviour of innovative stainless steels in mortar, 37 (2007) 1562–1569.

[37] S.J. Ahn, H.S. Kwon, Diffusivity of point defects in the passive film on Fe, Passiv. Met. Semicond. Prop. Thin Oxide Layers. 579 (2006) 311–316.

[38] F.R. Foulkes, P. McGrath, Rapid cyclic voltammetric method for studying cement factors affecting the corrosion of reinforced concrete, Cem. Concr. Res. 29 (1999) 873–

883.

[39] Y. Chen, M.E. Orazem, Impedance analysis of ASTM A416 tendon steel corrosion in alkaline simulated pore solutions, 104 (2016) 26–35

[40] S. Joiret, M. Keddam, X.R. Nóvoa, M.C. Pérez, C. Rangel, H. Takenouti, Use of EIS, ring-disk electrode, EQCM and Raman spectroscopy to study the film of oxides formed on iron in 1 M NaOH, Cem. Concr. Compos. 24 (2002) 7–15.

[41] P.S. and H.B. M. Büchler, Formation and Dissolution of the Passive Film on Iron Studied by a Light Reflectance Technique, J. Electrochem. Soc. 144 (1997) 2307–2312.

[42] I. March, The Nature of the Passive Film on Iron, (n.d.) 474–480.

[43] T. Nature, The Anodic Oxidation of Iron in a Neutral Solution The Nature and Composition of the Passive Film, 109 (1963).

[44] M. Sánchez, J. Gregori, M.C. Alonso, J.J. García-Jareño, F. Vicente, Anodic growth of passive layers on steel rebars in an alkaline medium simulating the concrete pores, Electrochim. Acta. 52 (2006) 47–53.

[45] Y. Chen, N.G. Rudawski, E. Lambers, M.E. Orazem, Application of Impedance Spectroscopy and Surface Analysis to Obtain Oxide Film Thickness, 164 (2017).

[46] M. Sánchez, J. Gregori, C. Alonso, J.J. García-Jareño, H. Takenouti, F. Vicente, Electrochemical impedance spectroscopy for studying passive layers on steel rebars immersed in alkaline solutions simulating concrete pores, Electrochim. Acta. 52 (2007) 7634–7641.

[47] H. Torbati-Sarraf, A. Poursaee, Study of the Passivation of Carbon Steel in Simulated Concrete Pore Solution Using Scanning Electrochemical Microscope (SECM),

Materialia. (2018).

[48] A. Poursaee, Determining the appropriate scan rate to perform cyclic polarization test on the steel bars in concrete, 55 (2010) 1200–1206.

[49] T. Journal, T. Journal, C.Y. Chao, D.D. Macdonald, A Point Defect Model for Anodic Passive Films, (1983) 1874–1879.

[50] S. Hashmi, ed., Comprehensive Materials Processing, Elsevier, 2014. https://www.elsevier.com/books/comprehensive-materials-processing/hashmi/978-0-08-096532-1.

[51] M.O.R.P.H.O.L.O.G.I.C.A.L. Instability, Mechanisms of Pearlite Spheroidization, 18 (1987) 1403–1414.

[52] D.D. Macdonald, M. Urquidi-Macdonald, Theory of Steady-State Passive Films, J. Electrochem. Soc. 137 (1990) 2395–2402.

[53] Y. Li, Y.F. Cheng, Passive film growth on carbon steel and its nanoscale features at various passivating potentials, Appl. Surf. Sci. 396 (2017) 144–153.

[54] S. Sharifi-Asl, D.D. Macdonald, A. Almarzooqi, B. Kursten, G.R. Engelhardt, A Comprehensive Electrochemical Impedance Spectroscopic Study of Passive Carbon Steel in Concrete Pore Water, J. Electrochem. Soc. 160 (2013) C316–C325.

[55] S. Sharifi-Asl, M.L. Taylor, Z. Lu, G.R. Engelhardt, B. Kursten, D.D. Macdonald, Modeling of the electrochemical impedance spectroscopic behavior of passive iron using a genetic algorithm approach, Electrochim. Acta. 102 (2013) 161–173.

[56] B.R. Kumar, R. Singh, B. Mahato, P.K. De, N.R. Bandyopadhyay, D.K. Bhattacharya, Effect of texture on corrosion behavior of AISI 304L stainless steel, 54

(2005) 141–147.

[57] M. Hoseini, A. Shahryari, S. Omanovic, J.A. Szpunar, Comparative effect of grain size and texture on the corrosion behaviour of commercially pure titanium processed by equal channel angular pressing, Corros. Sci. 51 (2009) 3064–3067.

[58] H.S. Kim, W.J. Kim, Annealing effects on the corrosion resistance of ultrafine-grained pure titanium, Corros. Sci. 89 (2014) 331–337.

[59] P. Gorostiza, F. Sanz, C. Mu, First Stages of Electrochemical Growth of the Passive Film on Iron, (2001) 307–313.

[60] M.E. Orazem, N. Pébère, B. Tribollet, J.E. Soc, P. B-b, M.E. Orazem, N. Pébère, B. Tribollet, Enhanced Graphical Representation of Electrochemical Impedance Data service Enhanced Graphical Representation of Electrochemical, 153 (2006) 128–136.

[61] B. Hirschorn, M.E. Orazem, B. Tribollet, V. Vivier, I. Frateur, M. Musiani, Determination of effective capacitance and film thickness from constant-phase-element parameters, Electrochim. Acta. 55 (2010) 6218–6227.

[62] P.K. Rai, S. Shekhar, K. Mondal, Development of gradient microstructure in mild steel and grain size dependence of its electrochemical response, Corros. Sci. 138 (2018) 85–95.

[63] O.F.Y.M. Kolotyrkin, I.I. Reformatskaya, L.I. Freiman, Precipitation of Sulfide Inclusions in Steel Structure and Their Effect on Local Corrosion Processes, 37 (2001) 511–516.

[64] F. Danoix, D. Julien, X. Sauvage, J. Copreaux, Direct evidence of cementite dissolution in drawn pearlitic steels observed by tomographic atom probe, 250 (1998) 8–

13.

[65] B. Mishra, D.L. Olson, M.M. Salama, Effect of Microstructure on Corrosion of Steels in Aqueous Solutions Containing Carbon Dioxide, (1998) 480–491.

[66] N.. M. A, S.A. Kaluzhina b, Microstructure Role in Passivation and Local Activation Processes of Carbon Steels N.A Muratova, ECS Trans. 13 (2008) 13–17.

CHAPTER 6

The influence of the sandblasting as a surface mechanical attrition treatment on the electrochemical behavior of carbon steel in different pH solutions[1]

Introduction

Studies showed that alteration of the surface structure of a metal can change the mechanical properties as well as corrosion behavior of metals [1-6]. In general, the surface mechanical attrition treatment (SMAT) technique modifies the surface structure of a metal by applying severe plastic deformation through impacting milling balls or hard particles onto the specimen's surface repeatedly [1, 7-14]. Sandblasting [7, 15-17], shot peening [8, 9, 18-21] are the typical SMATs which were successfully used.

The SMAT is an effective method of inducing localized plastic deformation that results in grain refinement down to the nanometer scale without changing the chemical composition of the materials [10, 12, 22-26]. It was shown that the severe plastic deformation induced by the SMAT significantly influences the corrosion resistance of a variety of metallic materials [27-34]. Sandblasting, as a SMAT method, was used for different applications such as enhancing the surface strength [35], alteration of the modification of the surface [36], and cleaning the surface of the metal [37]. While

[1] - L. Ding, H. Torbati-Sarraf A. Poursaee, Surface and coating technology, 2018.

sandblasting cleans the surface and removes the oxide layer from the surface, it also creates a local plastic deformation and grain modification on the surface [7, 38] which may lead to a compressive residual stress beneath the surface layer [17]. A study by Wang and Li showed formation of a nano-crystalline layer on the surface of the sandblasted 304 stainless steel [39]. This layer decreased the corrosion resistance of the sandblasted specimens significantly compared to the as-received specimens in a 3.5% NaCl solution. On the other hand, an investigation by Hou et al. indicated that sandblasting increased the corrosion resistance of carbon steel in an alkaline environment [40]. Ding and Poursaee also reported the significant improvement in corrosion resistance of the sandblasted specimens in an alkaline environment which was proportional to the increase in the sandblasting time. They hypothesized that the formation of calcium-rich layer combined with the enhanced passive layer on the sandblasted specimens were the reasons for the improvement [41].

While there are some studies on the impact of sandblasting on the corrosion resistance of carbon steel, nonetheless, to the best of the author's knowledge, there is no in-depth study on the impact of time of sandblasting on long-term corrosion of carbon steel in the different pH solutions, which was the objective of this work. In this study, the surfaces of the steel sheets were treated by sandblasting for 5, 10 and 15 min. and the impact of these treatments on the corrosion activity of carbon steel in acidic, neutral and basic solutions was studied. In addition, scanning electrochemical microscopy (SECM) along with microscopic analysis and micro-hardness measurements were exploited to determine the depth of the affected area as well as the impact of the duration of the

sandblasting on the activity of the surface and depth of the affected area.

Materials and Experimental

Steel specimens

All steel specimens were prepared from a carbon steel satisfying the ASTM A572-50 [42] with the properties given in Table 6-1.

Table 6-1. The chemical composition of the steel specimens

Element	C	Si	Mn	P	S	V	Ni	Co
Weight %	0.23	0.4	1.35	0.04	0.05	0.06	0.015	0.05

Specimens with a length of 90 mm and a width of 25.4 mm were cut and their surfaces were sandblasted by particles with an approximately 750 μm diameter under 350 kPa of air pressure. During sandblasting, the angle between the gun and the specimen was kept approximately 90°. As-received steel specimens (AR) as well as three sets of sandblasted specimens were used in this study. The as-received specimens were cut from degreased and cleaned as-rolled steel. Specimens were sandblasted for 5 min. (SB5), 10 min. (SB10), and 15 min. (SB15). A wire was welded to one end of each specimen for electrical connection required for the electrochemical tests. To prevent extraneous and edge effects, all the edge and wired was area was coated with epoxy, as shown in *Figure 6-1*. Epoxy coating provided a 70×20 mm exposure area. The as-received specimens washed and cleaned with ethyl alcohol to remove any possible grease and contaminations and dried immediately with air.

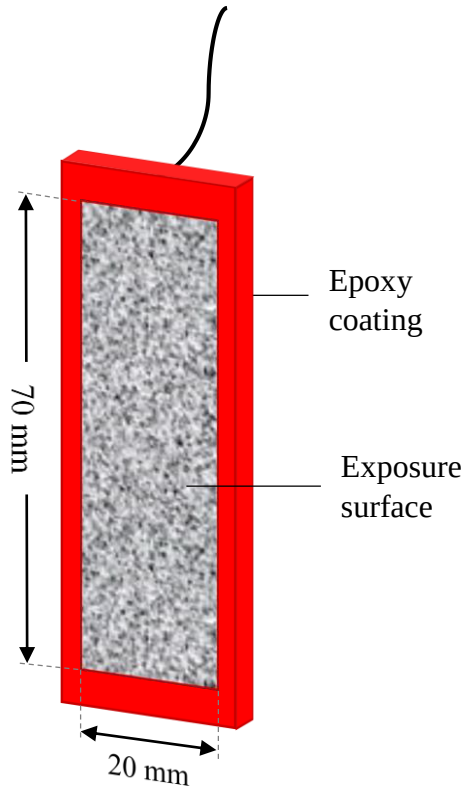

Figure 6-1. An epoxy coated steel specimen.

Experimental procedures

Optical microscopy was used to investigate the surface microstructure alteration due to sandblasting. In addition, to study the activity and the thickness of the affected area by the sandblasting, cross sections of the specimens were mounted in two-parted cold epoxy. Then, the surface was abraded successively with sandpapers and polished with 1μm alumina powder. The surface of each mounted specimen was etched in 4% v/v nital solution for 5 s to reveal its microstructure.

The hardness of the affected area (from the surface toward the center of each specimen) was measured using a Buehler Vickers micro-hardness tester with a load of 10 g and dwell time of 15s. Each point corresponded to the average of at least five indentation measurements. The acidic solution was made of 0.003 M HCl with the pH of 2.5. For the neutral solution, the pH of the deionized water was adjusted to 7.1, using 0.1 M Na3PO4 solution. An aqueous solution with 0.01 M NaOH and 0.01 M KOH was used to prepare the alkaline solution with a pH of 12.4.

To ascertain reproducibility and reliability of corrosion data, for each set of solution and treatment, a container with three identical steel specimens was prepared. The specimens were immersed in solutions and containers were sealed to minimize atmospheric effects, (e.g. carbonation and change in pH) and possible evaporation. Specimens were immersed in chloride-free solutions for 14 days, then the solution in each measurement cell was partially replaced with 3.5 % chloride contaminated solution, and the pH of all solutions was measured and adjusted every day to make sure that the pH stayed constant during the test. Electrochemical measurements were started 24 h after immersing the specimens in the solution and continued for 70 days. All tests were conducted at the laboratory temperature, i.e. ~23ºC.

A three-electrode measurement cell were used for all electrochemical tests. A steel specimen was used as the working electrode and a saturated calomel electrode (SCE) and a 316-stainless-steel sheet were used as the reference and the counter electrodes,

respectivly. The corrosion potential of the specimens was measured daily. The susceptibility of the specimens to pitting corrosion was evaluated by the Cyclic Polarization (CP) test. For all CP tests, the potential scanned from -50 mV versus open circuit potential to +500 mV versus the reference electrode and reversed to -100 mV versus the reference electrode with the scan rate of 0.1 mV/s. To determine the corrosion current density of the specimens, the Linear Polarization Resistance technique was used by applying a constant potential of ± 10 mV versus the corrosion potential to the specimen under test and measuring the resultant current [41]. PLPR was conducted every three days on each sample. To calculate the polarization resistance (R_p), the Tafel constants (β_a and β_c), were extracted from the results of the CP tests and used to calculate the value of the Stern-Geary constant. Electrochemical Impedance Spectroscopy (EIS) was also carried out on the specimens. A 10mV sinusoidal potential perturbation over the frequency range from 10^6 Hz to 10^{-2} Hz was used for the EIS tests. Impedance parameters consisting of constant phase element (C_{dl}), n, and R_{ct} were extracted from Nyquist plots.

For the SECM, the mounted specimen was placed horizontally, facing upward, in the cell. Scanning probe was a 10 μm diameter platinum microelectrode (UME) inside a capillary glass (RG[1]~15). Ag/AgCl (saturated KCl) and platinized platinum electrode were used as a reference and counter electrodes, respectively. The surface generated/tip

[1] RG = r_{glass}/r_T, where r_{glass} is the total radius of the probe including glass sheath and r_T is the radius of the Pt electrode

collection (SG/TC) mode was used in this experiment. Tests were conducted in a buffer solution with the pH=7, with a chemical composition of 8g/L NaCl, 0.2 g/L KCl, 1.44g/L Na_2HPO_4, 0.24 g/L KH_2PO_4, and 0.1 mM $K_3Fe(CN)_6$ as a redox mediator. The buffer solution was used to assure that the pH level stayed constant within the diffusion layer of the cut edge because of local reactions at the substrate [1,43]. The UME was biased at +0.9 V vs. Ag/AgCl for oxidation of mediator. After 5 min. immersion in the solution, 300 μm across the polished cross-section of each specimen (from the surface toward the center of the specimen) was scanned with the velocity of 1μm/s and the generated current from oxidation of mediator on the tip was recorded.

Results and discussion

Figure 6-2 and Figure 6-3 show images of the morphology, as well as the cross-section of each treated specimen, respectively. As can be seen, relatively similar morphology was obtained during 5 and 10 min. sandblasting. However, 15 min. sandblasted specimens showed less globular morphology compared to the other sandblasted times. In the cross sections images (Figure 6-3), severe plastic deformation and flow of material were observed on the surface and subsurface area. The thickness of the affected area was a function of the sandblasting time.

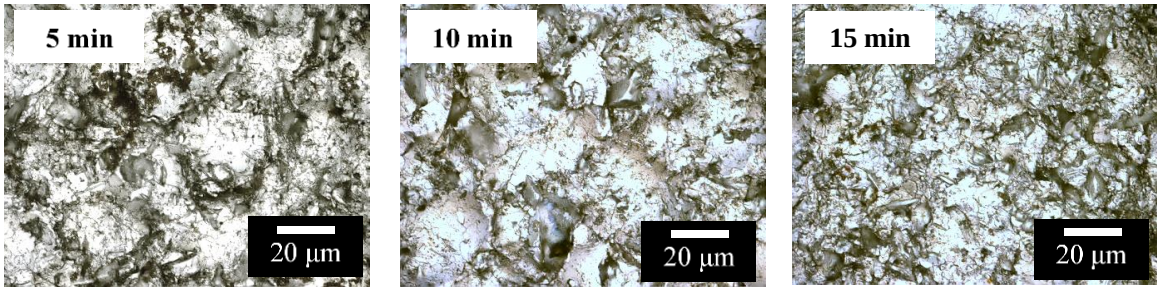

Figure 6-2. Microscopic images of the surfaces of the sandblasted specimens.

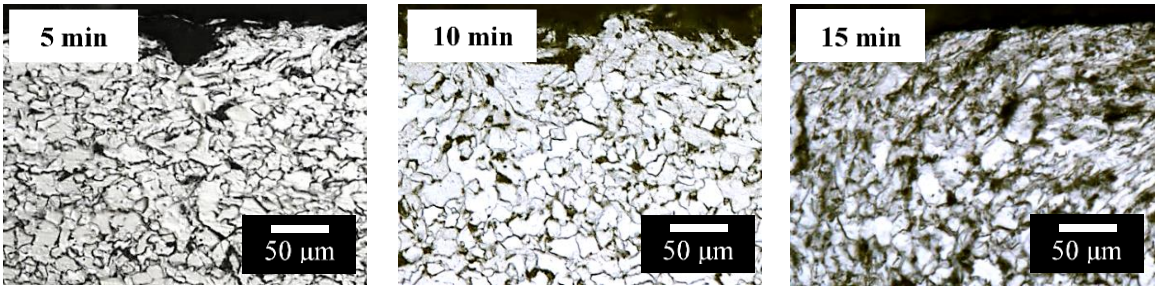

Figure 6-3. Microscopic images of the cross-section of the sandblasted specimens.

In sandblasting, repeated shock load with high-speed strain rate was applied to the surface, which may cause formation of high-density dislocations [2,44], deformation of grains, dissolution of cementite into other grains and ferrite [3], and presumably phase transformation due to high temperature generated during the local intense deformation [35,45,46].

Results of the arithmetical mean roughness value, R_a[1], greatest height of the roughness profile, R_z[2], and estimated thickness of the deformed area for the sandblasted

[1] *Ra is calculated by an algorithm that measures the average length between the peaks and valleys and the deviation from the mean line on the entire surface within the sampling length. Ra averages all peaks and valleys of the roughness profile.*

[2] *Rz is the average maximum peak to valley of five consecutive sampling lengths within the measuring length.*

specimens are given in Table 6-2. While the thickness of the impacted area was increased by increasing the time of sandblasting, the R_a value increased from 5 to 10 min. of sandblasting and stayed relatively constant thereafter.

Table 6-2. The measured mean grain size of the bulk, roughness, and thickness of the affected area.

Sample	The average grain size of the bulk	R_a (μm)	R_z (μm)	Deformed Thickness (μm)
AR	14±8	0.7±0.3	0.8	-
SB5	14±8	12.7±4.1	16.1	17±7
SB10	14±8	8.9±3.9	12.2	24±9
SB15	14±8	8.1±3.1	8.4	45±10

However, R_z values slightly decreased by increasing the duration of sandblasting, meaning that the height of the peaks and valleys declined by increasing the time of sandblasting, which could be attributed to the increase of the repeated multidirectional impact of the sand particles onto the surface due to their random flying directions from moving gun[3-5].

To quantify the depth of sandblasting, i.e. affected area, SECM data along with the micro-hardness profiles on the cross-section of the as-received and sandblasted specimens are presented in Figure 6-4. For all specimens, the current value at the surface of each specimen was higher compared to the other parts of the same specimen, due to the higher corrosion activity of the surface compared to the rest of the specimen. This observation corresponded well with the change in the micro-hardness versus the distance from the surface, which decreases progressively due to a transitional plastic deformed region. Increasing the time of sandblasting, increased the current at the surface. This

current gradually decayed by moving toward the center of the specimen. At a particular distance from the surface of each specimen, the current, as well as the hardness, became stable and did not change.

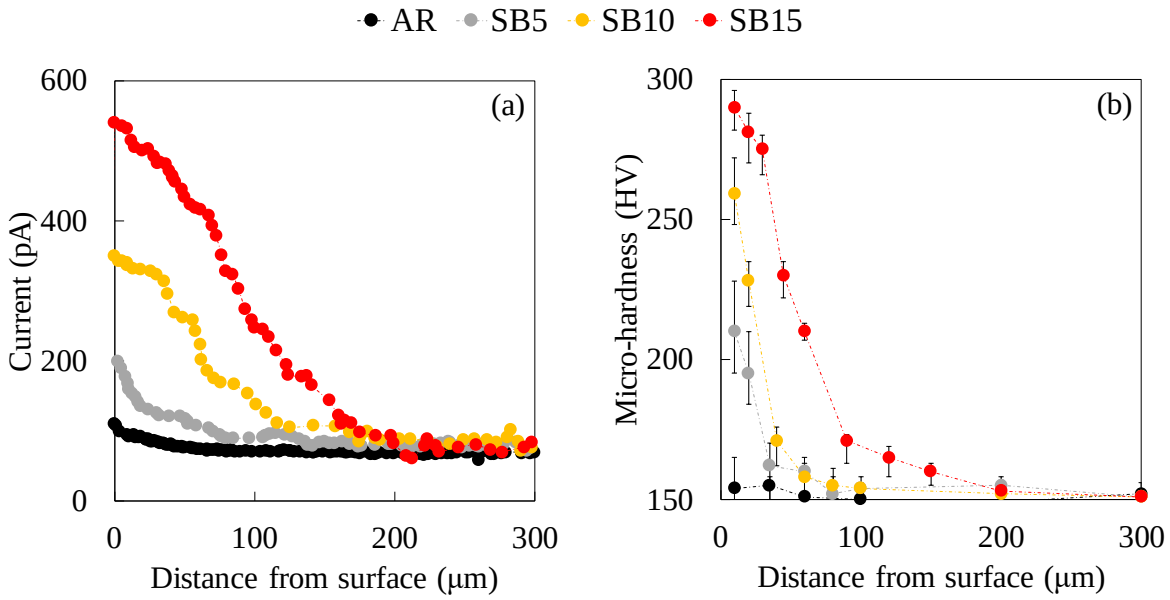

Figure 6-4. SECM currents obtained from the line scan, and (b) micro-hardness values from the cross-section of the specimens.

This distance was determined using the data from Figure 4(a) and is shown in Figure 6 5. As can be seen, there is a relatively linear relationship between this distance and the sandblasting time. This observation showed that sandblasting not only increased surface activity but also changed the electrochemical behavior of the bulk material by inducing plastic strain in the depth of material [6-9, 47]. This change was linearly a function of the sandblasting time. Increasing current particularly at the surface due to sandblasting attributed to the refined structured layer with various dislocation configurations such as dense dislocation walls, dislocation tangles, and dislocation cells

[3, 10-12, 21].

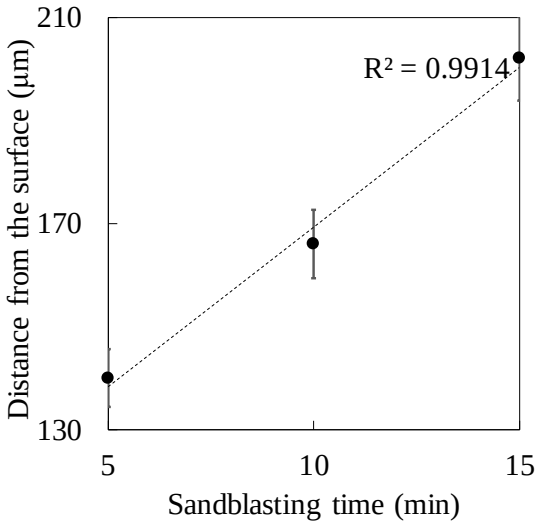

Figure 6-5. Distance from the surface when the current stabilized in the SECM experiment.

Figure 6-6 shows the corrosion potential values of all specimens in all solutions. In neutral solution, the SB5 specimens showed relatively nobler corrosion potential compared to the other specimens, followed by the as-received, SB10, and SB15. By the addition of the chlorides, all corrosion potential values shifted rapidly to more negative values which indicating increasing the corrosion activity. The corrosion potential values for all specimens became relatively stable after 2-3 days. However, the SB5 specimens still showed more positive indicating relatively less corrosion tendency compared to the other specimens. This observation for SB10 and SB15 was attributed to inducing micro-strains, reducing electron work function and decreasing the energy barrier for

electrochemical reactions due to sandblasting [30-33, 48].

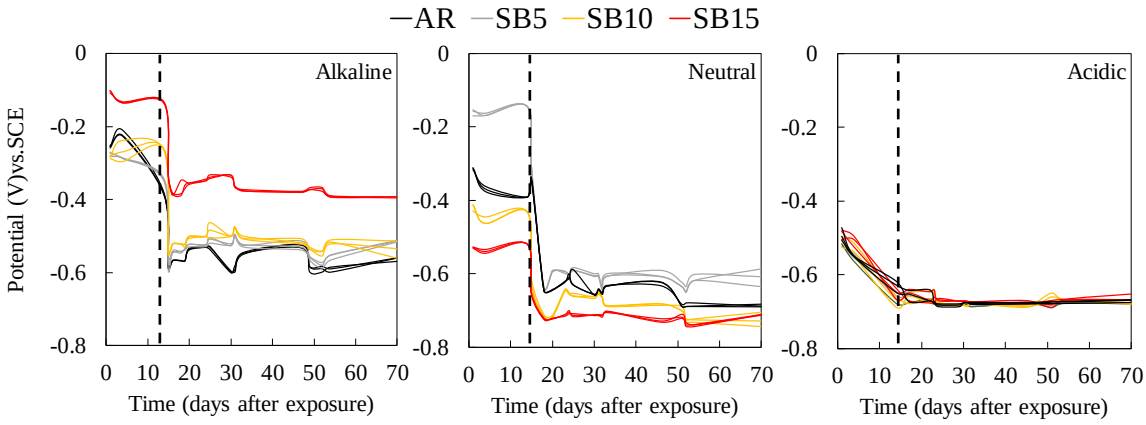

Figure 6-6. Corrosion potential of values all specimens versus time of exposure. Vertical dashed lines represent the date of the addition of chlorides.

In chloride-free acidic solution, all specimens showed active corrosion and they had relatively similar potentials. These values shifted slightly to more negative values by the time of immersion, implying anodic dissolution of surface. Addition of chlorides did not affect the potential values significantly compare to a neutral solution, implying specimens corroded actively through the whole experiment.

In alkaline solution, the potential values showed the formation of the protective layer on the surface of the specimens in chloride-free solution [11,12,16,18,49,50]. The potential of the specimens in chloride-free alkaline solution was a function of sandblasting duration, i.e. increasing the time of sandblasting, shifted the potentials to more noble values. Addition of chlorides to the alkaline solution after 14 days shifted the corrosion potential values of AR, SB5 and SB10 specimens from -0.3 V to approximately -0.6 V vs. SCE, indicating the initiation and progress of dissolution, i.e. active corrosion, of those specimens. Nevertheless, the addition of chlorides altered the potential of SB15

from approximately -0.1 V to -0.4 V indicating less corrosion tendency, presumably due to the formation of a more ablative barrier layer on the surface of SB15 specimens compared to the other specimens [20]. The corrosion current density values calculated from the results of the PLPR tests are shown in Figure 6-7.

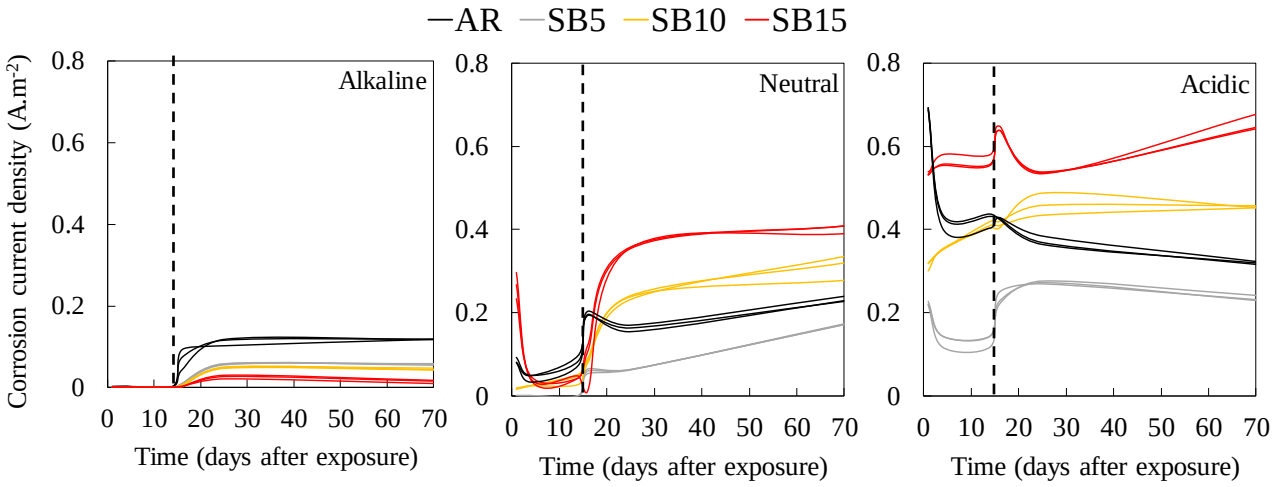

Figure 6-7. Corrosion current densities of all specimen versus time of exposure. The vertical dashed line represents the date of the addition of chlorides.

In alkaline solution, all values of current densities were around 10-3 $A.m^{-2}$ in chloride-free solution, indicating the formation of the protective layer on the surface of all specimens [41, 51]. After addition of chlorides, the current densities of all specimens started to increase and reached to steady state after 4-5 days. This increment in corrosion activity, due to addition of chloride, was highest for the AR specimens compared to the SB specimens and followed by SB15, SB10, and SB5 specimens. Obviously, the sandblasting improved the corrosion resistance of the steel in alkaline solution significantly. The results corresponded well with the results from the corrosion potential measurements. In contrast to the alkaline solution, in neutral and acidic solution, SB15

and then SB10 showed the highest corrosion current density, followed by as-received specimens, both before and after addition of chloride; and the SB5 specimens showed the lowest corrosion current density among the other specimens. In acidic solution, the addition of chloride did not noticeably change the corrosion current density of the specimens, particularly for SB15 and SB10, compared to the neutral and alkaline solutions. While the result from the LPR indicated that the lowest corrosion activity for the SB5 specimens in acidic solution, the results of the corrosion potential measurements did not show this distinction.

The mass losses for all three specimens from each condition were calculated using the area under the curves (in Figure 6-7) and Faraday's law [52], and the percentages of the mass loss change of the sandblasted specimens versus the as-received specimens are shown in Figure 6-8. The major change in corrosion resistance because of sandblasting occurred in alkaline solution. This change (improvement) was proportional with the time of sandblasting, i.e. 15 min. sandblasting reduced the mass loss of the steel in alkaline solution compared to the as-received steel in the same solution, approximately 89 %. However, in neutral and acidic solutions, 15 min. sandblasting increased the mass loss of steel about 40 and 75%, respectively.

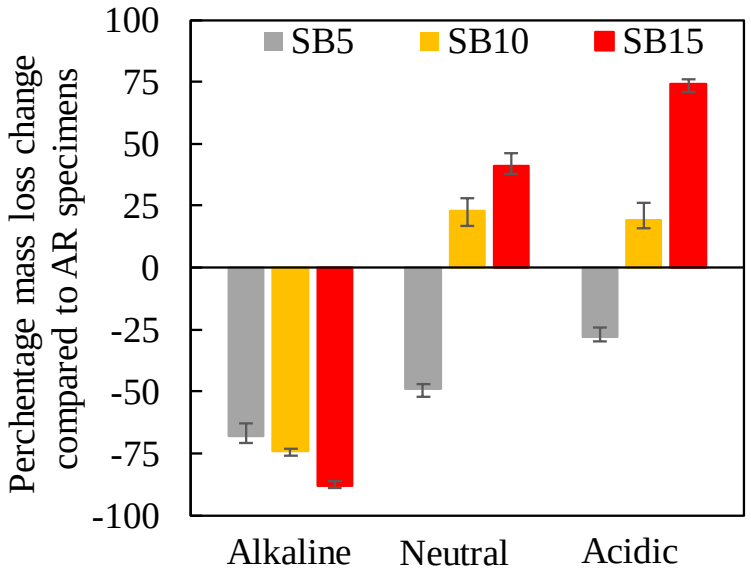

Figure 6-8. Percentage of mass loss of the sandblasted specimens compared to the as-received specimens in different solutions during immersion.

Figure 6-9 shows the results of the cyclic polarization experiments on one of the specimens of each group 56 days after the addition of salt to the solutions. All specimens in neutral and acidic solutions showed active corrosion. The SB5 specimen in both neutral and acidic solution, particularly in the neutral solution, performed better compared to the other specimens which is in agreement with PLPR results. However, in alkaline solution, the SB15 specimen indicated lower active corrosion and higher pitting potential than the SB10, followed by the SB5 and the AR specimens. As we showed in SECM and PLPR part, longer sandblasted specimens showed more activity on the surface which leads more oxidation preferably on defects or dislocations and grain bounders, however, in high alkaline environment this reaction with hydroxyl ions forms a

passivating film on iron surface. Therefore, higher rate of reactions and rapid formation of Fe oxyhydroxide layer on more defected matrix which acted as nucleation site improved passivation procedure [44, 53]. Comparing all polarization curves of the sandblasted specimens, indicated that increasing the time of treatment increased the pitting potential which showed higher integrity of the passive layer for sandblasted specimens. This trend also can be seen in reverse scan, where SB15 still maintained the lower passivation current.

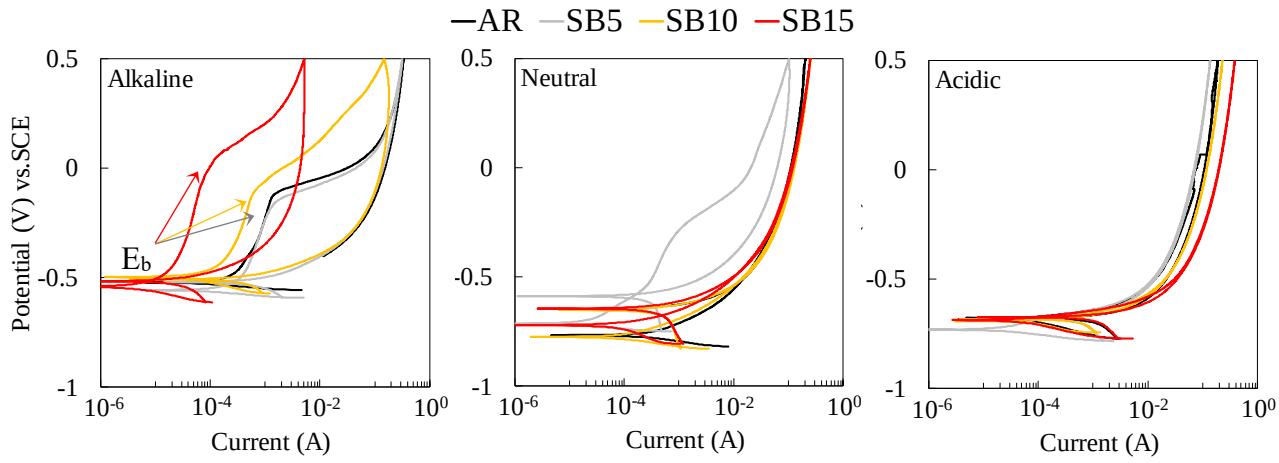

Figure 6-9. Cyclic polarization curves of one of the specimens in each measurement cell 56 days after exposure to the chloride-contaminated solutions.

In order to evaluate the effect of inducing plastic strain with sandblasting procedure on the corrosion and stability of corrosion film, impedance test was also performed. The Nyquist plots from the EIS tests, which are shown in Figure 6-10, also indicated similar trends as the other electrochemical measurements. Each Nyquist plot

was dominated by a capacitive arc. In alkaline solution, the SB15 specimens showed highest corrosion resistance which corroborates with previous results. In the neutral and acidic solutions, the arc diameters for the SB5 were larger than others both before and after addition of the chlorides.

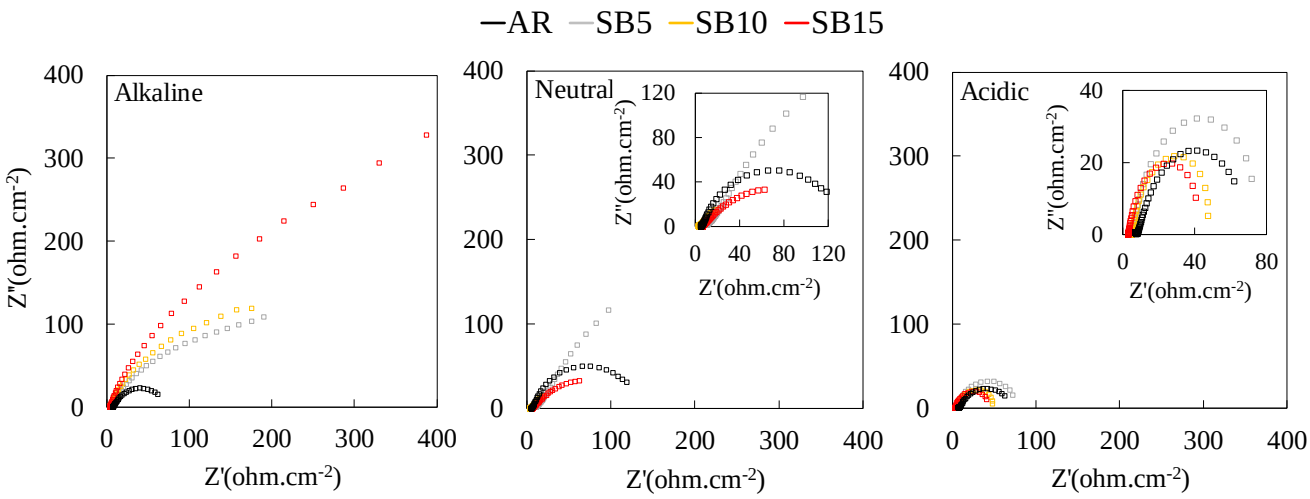

Figure 6-10. Nyquist plots for one of the specimens in each measurement cell 8 weeks after exposure to the chloride-contaminated solutions.

All EIS data were fitted using the equivalent circuit shown in Figure 6-11, where R_s was the solution resistance, R_{po} was the resistance and CPE_{po} was the constant-phase element of the of the pores film, R_{ct} was the charge-transfer resistance, and CPE_{dl} was the constant-phase element of double-layer.

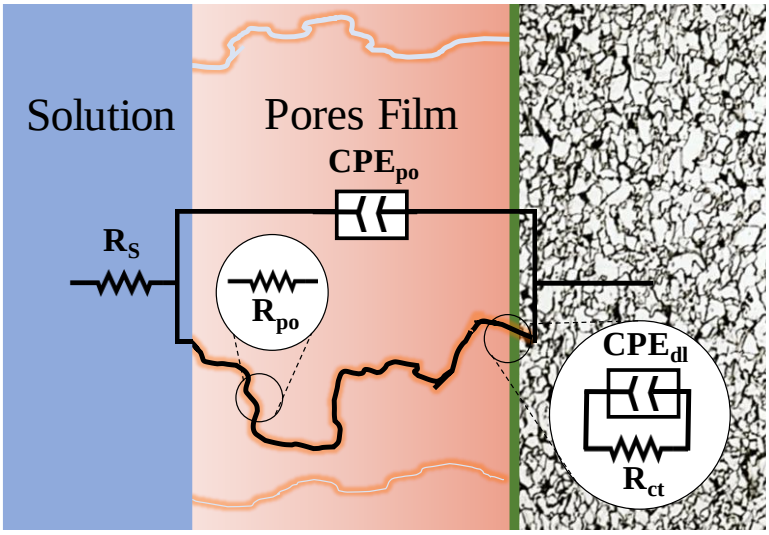

Figure 6-11. Electrochemical equivalent circuits used to fit the EIS data in this work.

In the analysis of the Nyquist diagrams the constant phase element, CPE was used instead of an 'ideal' capacitor to address the deviations of the capacitive loops. The impedance, Z_{CPE} of the CPE, is described by the expression [35]:

$$Z_{CPE} = [CPE(j\omega)^n]^{-1} \quad (1)$$

Where $j=\sqrt{(-1)}$, ω is angular frequency and n is deviation parameter, implying microscopic fluctuation of the surface metal, due to the surface heterogeneities [35,37]. Depending on n, CPE can represent a pure capacitance (n=1) or a pure resistance (n=0). The deviation of n from these values indicates a deviation from the ideal behavior of the system, which was observed for all the specimens. The deviation from a pure capacitance behavior of the double-layer ascribed to surface heterogeneities at the micrometric (roughness, polycrystalline structure) and atomic (surface disorder as dislocations and

steps, chemical in-homogeneities) scale and adsorption phenomena. The n_{po} values of less than 1, was attributed to the surface heterogeneities [54, 55].

The parameters obtained from a circuit equivalent are given in Table 6-3 for 56 days in chloride-contaminated solutions. It was shown that the values of the double-layer constant phase element capacitance are inversely proportional to the thickness of the passive layer [17]. In alkaline solution, by increasing the time of sandblasting, R_{ct} and Rpo increases and double layer capacitance decreased, which indicating an increase in the thicker and smooth nature of protective layer forms on the surface of sandblasted specimens. However, n values decreased by the time of sandblasting. Increasing the surface energy and the roughness of the sandblasted specimens could be the reason for such behavior.

Table 6-3. Values of the elements of the equivalent circuit in Figure 6-11 to fit the impedance spectra of Figure 6-10.

Solution	**Specimens**	**R_s**	**R_{ct}**	**R_{po}**	**CPE_{dl}**	**CPE_{po}**	**n_{dl}**	**n_{po}**
		($\Omega.cm^2$)			($\Omega^{-1}\ s^n\ cm^{-2}$)			
Neutral	SB5	8.64	82.34	86.43	32.56	33.15	0.88	0.89
	SB10	9.56	73.42	77.25	56.18	34.17	0.95	0.93
	SB15	11.45	50.13	50.45	66.43	53.47	0.97	0.97
	AR	9.13	82.34	80.01	43.19	34.68	0.92	0.93
Acidic	SB5	12.01	31.01	35.12	125.68	118.09	0.91	0.91
	SB10	12.33	20.29	32.10	130.57	110.13	0.98	0.98
	SB15	12.29	15.03	11.03	213.12	290.03	0.98	0.98
	AR	12.16	27.68	30.19	112.40	112	0.92	0.92
Alkaline	SB5	7.79	106.56	116.31	21.31	16.32	0.82	0.82
	SB10	6.42	132.53	173.65	17.54	15.23	0.84	0.88
	SB15	5.38	279.35	283.42	10.43	18.65	0.80	0.85
	AR	8.63	76.40	82.69	32.53	32.05	0.85	0.86

In neutral and acidic solutions, the trends exactly complied with the other results, i.e. SB5 had the highest R_{ct} values followed by the AR, SB10, and SB15. SB5 had the least capacitance meaning that the oxide layer formed on the surface was smooth and thicker compared to the other specimens even AR. The enhanced corrosion resistance of the SB5 specimens compared to the SB10 and SB15 in neutral and acidic environments was attributed to the thickness of the affected layer. It was hypothesized that due to the presence of more rough and active layer (affected area) on the surface of the SB specimens, corrosion started and progressed with higher rates compared to the AR specimens, at the first stages of the immersion. This initiation and propagation was a function of sandblasting time, as demonstrated in SECM results. However, the thickness of the active affected area in the SB5 specimens was smaller, compared to the other sandblasted specimens. The microscopic analysis showed that the grain size in the SB5 specimens was about the same size as the thickness of the deformed area (Figure 6-5 and Table 6-2). Thus, it was assumed that the 5 min. sandblasting was not enough time to completely reform and induce micro-strain to deeper grains and, therefore, approximately the first series of surface grains were affected. Hence, due to the more active nature of the deformed grains compared to the other in-depth grains (Figure 6-4a), at the first stages of the exposure, oxides layer were formed on the surface of the SB5 specimens faster than the AR specimens. By consuming, reacting and forming a layer from the surface grains, remained grains underneath of the SB5 specimens behaved similar to the AR specimens (less active) but with a layer of dense corrosion products on their surface. Similar behavior for the SB5 and AR specimens can be observed in Figure 6-7 for neutral and

acidic solutions. Furthermore, the R_{po} for SB5 specimens in both neutral and acidic solutions were higher than those for the AR specimens. For the SB10 and SB15 specimens, however, the thicker affected area continued to corrode with high rate compared to the AR specimens.

Conclusion

SECM was successfully used to directly evaluate the impact of sandblasting as a simple example of SMAT process on the electrochemical activity of the steel surface in solution with neutral pH. This approach provided a better understanding the effect of grain refinement and plastic deformation on the electrochemical behavior which corroborated well with micro-hardness data. Sandblasting increased the surface roughness and induced plastic deformation within the depth of the steel. Increasing the duration of sandblasting, increased the thickness of the affected area. However, on average, the surface roughness (Ra) was not a function of the duration of the sandblasting.SB5 specimens showed improved corrosion resistance compared to the other sandblasted (sandblasted for longer period of time) and AR specimens in neutral and acidic solutions. It was hypothesized that upon exposure to the neutral and acidic solutions, for the SB5 specimens, the affected area corroded rapidly, and corrosion products could act as a protective barrier and reduced the corrosion rate on the SB5 specimens. Nevertheless, the corrosion continued activity on the other SB specimens. Sandblasted specimens showed more active corrosion compared to the as-received specimens in neutral and acidic solutions due to the high-energetic and strained areas formed by the impact of blasted sand. This

increase in corrosion activity was the function of the time of sandblasting. In alkaline solution, formation of a presumably protective passive layer on the surface of the sandblasted specimens improved the corrosion resistance and enhanced integrity to localized attack of these specimens. The improvement was proportional to duration of sandblasting.

References

[1] N. Tao, Z. Wang, W. Tong, M. Sui, J. Lu, K. Lu, An investigation of surface nanocrystallization mechanism in Fe induced by surface mechanical attrition treatment, Acta materialia, 50 (2002) 4603-4616.

[2] G. Liu, S. Wang, X. Lou, J. Lu, K. Lu, Low carbon steel with nanostructured surface layer induced by high-energy shot peening, Scripta Materialia, 44 (2001) 1791-1795.

[3] T. Balusamy, S. Kumar, T.S. Narayanan, Effect of surface nanocrystallization on the corrosion behaviour of AISI 409 stainless steel, Corros Sci, 52 (2010) 3826-3834.

[4] A. Chen, Y. Li, J. Zhang, D. Pan, J. Lu, The influence of interface structure on nanocrystalline deformation of a layered and nanostructured steel, Mater Design, 47 (2013) 316-322.

[5] T. Fu, Z. Zhan, L. Zhang, Y. Yang, Z. Liu, J. Liu, L. Li, X. Yu, Effect of surface mechanical attrition treatment on corrosion resistance of commercial pure titanium, Surface and Coatings Technology, 280 (2015) 129-135.

[6] Y. Liu, B. Jin, D.-J. Li, X.-Q. Zeng, J. Lu, Wear behavior of nanocrystalline structured magnesium alloy induced by surface mechanical attrition treatment, Surface and Coatings Technology, 261 (2015) 219-226.

[7] M. Multigner, E. Frutos, J. González-Carrasco, J. Jiménez, P. Marín, J. Ibáñez, Influence of the sandblasting on the subsurface microstructure of 316LVM stainless steel: Implications on the magnetic and mechanical properties, Materials Science and Engineering: C, 29 (2009) 1357-1360.

[8] V. Azar, B. Hashemi, M.R. Yazdi, The effect of shot peening on fatigue and corrosion behavior of 316L stainless steel in Ringer's solution, Surface and Coatings Technology, 204 (2010) 3546-3551.

[9] P. Peyre, X. Scherpereel, L. Berthe, C. Carboni, R. Fabbro, G. Beranger, C. Lemaitre, Surface modifications induced in 316L steel by laser peening and shot-peening. Influence on pitting corrosion resistance, Materials Science and Engineering: A, 280 (2000) 294-302.

[10] G. Liu, J. Lu, K. Lu, Surface nanocrystallization of 316L stainless steel induced by ultrasonic shot peening, Materials Science and Engineering: A, 286 (2000) 91-95.

[11] K. Dai, J. Villegas, Z. Stone, L. Shaw, Finite element modeling of the surface roughness of 5052 Al alloy subjected to a surface severe plastic deformation process, Acta Materialia, 52 (2004) 5771-5782.

[12] K. Lu, J. Lu, Nanostructured surface layer on metallic materials induced by surface mechanical attrition treatment, Materials Science and Engineering: A, 375 (2004) 38-45.

[13] A.H. Astaraee, R. Miresmaeili, S. Bagherifard, M. Guagliano, M. Aliofkhazraei, Incorporating the principles of shot peening for a better understanding of surface mechanical attrition treatment (SMAT) by simulations and experiments, Mater Design, 116 (2017) 365-373.

[14] S. Bagherifard, S. Slawik, I. Fernández-Pariente, C. Pauly, F. Mücklich, M. Guagliano, Nanoscale surface modification of AISI 316L stainless steel by severe shot peening, Mater Design, 102 (2016) 68-77.

[15] M. Multigner, S. Ferreira-Barragáns, E. Frutos, M. Jaafar, J. Ibáñez, P. Marín, M. Pérez-Prado, G. González-Doncel, A. Asenjo, J. González-Carrasco, Superficial severe plastic deformation of 316 LVM stainless steel through grit blasting: Effects on its microstructure and subsurface mechanical properties, Surface and Coatings Technology, 205 (2010) 1830-1837.

[16] A. Rudawska, I. Danczak, M. Müller, P. Valasek, The effect of sandblasting on surface properties for adhesion, International Journal of Adhesion and Adhesives, 70 (2016) 176-190.

[17] S. Geng, J. Sun, L. Guo, Effect of sandblasting and subsequent acid pickling and passivation on the microstructure and corrosion behavior of 316L stainless steel, Mater Design, 88 (2015) 1-7.

[18] S. Pour-Ali, A.-R. Kiani-Rashid, A. Babakhani, Surface nanocrystallization and gradient microstructural evolutions in the surface layers of 321 stainless steel alloy

treated via severe shot peening, Vacuum, 144 (2017) 152-159.

[19] S. Pour-Ali, A.-R. Kiani-Rashid, A. Babakhani, S. Virtanen, M. Allieta, Correlation between the surface coverage of severe shot peening and surface microstructural evolutions in AISI 321: A TEM, FE-SEM and GI-XRD study, Surface and Coatings Technology, 334 (2018) 461-470.

[20] M. Jayalakshmi, P. Huilgol, B.R. Bhat, K.U. Bhat, Microstructural characterization of low temperature plasma-nitrided 316L stainless steel surface with prior severe shot peening, Mater Design, 108 (2016) 448-454.

[21] B. Mordyuk, O. Karasevskaya, G. Prokopenko, N. Khripta, Ultrafine-grained textured surface layer on Zr–1% Nb alloy produced by ultrasonic impact peening for enhanced corrosion resistance, Surface and Coatings Technology, 210 (2012) 54-61.

[22] S. Benafia, D. Retraint, S.Y. Brou, B. Panicaud, J.G. Poussard, Influence of Surface Mechanical Attrition Treatment on the oxidation behaviour of 316L stainless steel, Corros Sci, DOI (2018).

[23] T. Chen, H. John, J. Xu, Q. Lu, J. Hawk, X. Liu, Influence of surface modifications on pitting corrosion behavior of nickel-base alloy 718. Part 1: Effect of machine hammer peening, Corros Sci, 77 (2013) 230-245.

[24] Z. Yin, X. Yang, X. Ma, J. Moering, J. Yang, Y. Gong, Y. Zhu, X. Zhu, Strength and ductility of gradient structured copper obtained by surface mechanical attrition treatment, Mater Design, 105 (2016) 89-95.

[25] Y.-L. An, H.-Y. Du, Y.-H. Wei, N. Wang, L.-F. Hou, W.-M. Lin, Interfacial structure and mechanical properties of surface iron–nickel alloying layer in pure iron fabricated by

surface mechanical attrition alloy treatment, Mater Design, 46 (2013) 627-633.

[26] L. Petan, J.L. Ocaña, J. Grum, Influence of laser shock peening pulse density and spot size on the surface integrity of X2NiCoMo18-9-5 maraging steel, Surface and Coatings Technology, 307 (2016) 262-270.

[27] S. Hassani, K. Raeissi, M. Azzi, D. Li, M. Golozar, J. Szpunar, Improving the corrosion and tribocorrosion resistance of Ni–Co nanocrystalline coatings in NaOH solution, Corros Sci, 51 (2009) 2371-2379.

[28] J. Hou, Q. Peng, Z. Lu, T. Shoji, J. Wang, E.-H. Han, W. Ke, Effects of cold working degrees on grain boundary characters and strain concentration at grain boundaries in Alloy 600, Corros Sci, 53 (2011) 1137-1142.

[29] A.S. Hamdy, E. El-Shenawy, T. El-Bitar, Electrochemical impedance spectroscopy study of the corrosion behavior of some niobium bearing stainless steels in 3.5% NaCl, International Journal of Electrochemical Science, 1 (2006) 171-180.

[30] T. Wang, J. Yu, B. Dong, Surface nanocrystallization induced by shot peening and its effect on corrosion resistance of 1Cr18Ni9Ti stainless steel, Surface and Coatings Technology, 200 (2006) 4777-4781.

[31] G.B. Hamu, D. Eliezer, L. Wagner, The relation between severe plastic deformation microstructure and corrosion behavior of AZ31 magnesium alloy, Journal of alloys and compounds, 468 (2009) 222-229.

[32] H.-S. Lee, D.-S. Kim, J.-S. Jung, Y.-S. Pyoun, K. Shin, Influence of peening on the corrosion properties of AISI 304 stainless steel, Corros Sci, 51 (2009) 2826-2830.

[33] B. Mordyuk, G. Prokopenko, M. Vasylyev, M. Iefimov, Effect of structure evolution

induced by ultrasonic peening on the corrosion behavior of AISI-321 stainless steel, Materials Science and Engineering: A, 458 (2007) 253-261.

[34] H. Torbati-Sarraf, A. Poursaee, Corrosion of coupled steels with different microstructures in concrete environment, Constr. Build. Mater, 167 (2018) 680-687.

[35] R.K. Chintapalli, A.M. Rodriguez, F.G. Marro, M. Anglada, Effect of sandblasting and residual stress on strength of zirconia for restorative dentistry applications, Journal of the mechanical behavior of biomedical materials, 29 (2014) 126-137.

[36] R.K. Chintapalli, F.G. Marro, E. Jimenez-Pique, M. Anglada, Phase transformation and subsurface damage in 3Y-TZP after sandblasting, Dental Materials, 29 (2013) 566-572.

[37] A. Raykowski, M. Hader, B. Maragno, J. Spelt, Blast cleaning of gas turbine components: deposit removal and substrate deformation, Wear, 249 (2001) 126-131.

[38] L. Yuan, X. Chen, S. Maganty, J. Cho, C. Ke, G. Zhou, Enhancing the oxidation resistance of copper by using sandblasted copper surfaces, Applied Surface Science, 357 (2015) 2160-2168.

[39] X. Wang, D. Li, Mechanical and electrochemical behavior of nanocrystalline surface of 304 stainless steel, Electrochim. Acta, 47 (2002) 3939-3947.

[40] J. Hou, X. Fu, D. Chung, Improving both bond strength and corrosion resistance of steel rebar in concrete by water immersion or sand blasting of rebar, Cem. Concr. Res, 27 (1997) 679-684.

[41] L. Ding, A. Poursaee, The impact of sandblasting as a surface modification method on the corrosion behavior of steels in simulated concrete pore solution, Constr. Build.

Mater, 157 (2017) 591-599.

[42] A. A572/A572M-15, Standard Specification for High-Strength Low-Alloy Columbium-Vanadium Structural Steel, ASTM International, West Conshohocken, PA, 2015.

[43] A. Marques, J. Izquierdo, R. Souto, A. Simões, SECM imaging of the cut edge corrosion of galvanized steel as a function of pH, Electrochim. Acta, 153 (2015) 238-245.

[44] Y. Li, L. Hou, Y. Wei, H. Wei, Y. Cheng, Enhancement of siliconizing behaviors in pure iron induced by surface mechanical attrition treatment, Surface and Coatings Technology, 309 (2017) 462-470.

[45] H. Sun, Y. Shi, M.-X. Zhang, K. Lu, Surface alloying of an Mg alloy subjected to surface mechanical attrition treatment, Surface and Coatings Technology, 202 (2008) 3947-3953.

[46] A. Amanov, Y.-S. Pyun, Local heat treatment with and without ultrasonic nanocrystal surface modification of Ti-6Al-4V alloy: Mechanical and tribological properties, Surface and Coatings Technology, 326 (2017) 343-354.

[47] A.M. Gatey, S.S. Hosmani, C.A. Figueroa, S.B. Arya, R.P. Singh, Role of surface mechanical attrition treatment and chemical etching on plasma nitriding behavior of AISI 304L steel, Surface and Coatings Technology, 304 (2016) 413-424.

[48] U. Trdan, J. Grum, Evaluation of corrosion resistance of AA6082-T651 aluminium alloy after laser shock peening by means of cyclic polarisation and ElS methods, Corros Sci, 59 (2012) 324-333.

[49] A. Poursaee, Temperature dependence of the formation of the passivation layer on

carbon steel in high alkaline environment of concrete pore solution, Electrochemistry Communications, 73 (2016) 24-28.

[50] R.B. Figueira, C.J. Silva, E.V. Pereira, Hybrid sol–gel coatings for corrosion protection of hot-dip galvanized steel in alkaline medium, Surface and Coatings Technology, 265 (2015) 191-204.

[51] C.M. Hansson, Comments on electrochemical measurements of the rate of corrosion of steel in concrete, Cem. Concr. Res, 14 (1984) 574-584.

[52] A. Poursaee, Corrosion measurement techniques in steel reinforced concrete, Journal of ASTM International, 8 (2011) 1-15.

[53] V. Afshari, C. Dehghanian, Effects of grain size on the electrochemical corrosion behaviour of electrodeposited nanocrystalline Fe coatings in alkaline solution, Corros Sci, 51 (2009) 1844-1849.

[54] J.-B. Jorcin, M.E. Orazem, N. Pébère, B. Tribollet, CPE analysis by local electrochemical impedance spectroscopy, Electrochim. Acta, 51 (2006) 1473-1479.

[55] P. Córdoba-Torres, T. Mesquita, O. Devos, B. Tribollet, V. Roche, R. Nogueira, On the intrinsic coupling between constant-phase element parameters α and Q in electrochemical impedance spectroscopy, Electrochim. Acta, 72 (2012) 172-178.

CHAPTER 7

Electrochemical spectroscopic analyses of the influence of the surface nano-crystallization on the passivation of a carbon steel in high pH solution[1]

Introduction

A metal or alloy surface consists of composites of crystalline grains, boundaries and distributed phases that dictates the properties of the metal surface [1–3]. Grain refinement and ultimately reaching a nano-crystalline material, with the average grain size below 100 nm, provides promising physical, electrochemical and catalytic activity properties [2,4–11]. These improvements originate from the large volume fraction of the grain boundaries and crystalline edges mismatches [12–16]. Surface grain refinement introduces novel properties compared to the underneath matrix, while the chemical composition remains unchanged. Such treatment on metals can be achieved through various conventional surface treatment procedures such as wire brushing, sandblasting, ultrasonic shot peening and other surface mechanical attrition treatments (SMAT) [15,17–23].

In such process, the surface of a sample is blasted repeatedly by high speed solid particles, which leads to local sever plastic deformation and subsurface grain refinement

[1] - H. Torbati-Sarraf , L. Ding, I. Khakpour, A. Poursaee, Applied surface science, Under review.

while leaves compressive residual stress on the surface [5,16]. The microstructure obtained by this method has larger specific interphase energy compared to the underneath microstructure [4,8]. This characteristic of refined microstructure leads to a different corrosion behavior compared to polycrystalline counterparts; albeit this behavior depends on the environment potency [13,24–26].

Various types of carbon steel are widely used in different industries such as transportation and infrastructure [25,27–29]. In alkaline environment, a protective oxide film forms, spontaneously, on the surface of the carbon steel that provides natural protection against corrosion [25,30–37]. Previous studies suggest that this film encompasses various composition ranging from amorphous Fe hydroxides / oxyhydroxide [38–41] to layers and crystalline forms of Fe oxide spinel [42–45]. Consequently, semiconductive properties are observed on the surface of the passivated steel. This highly defective oxide film has the nature of an n-type semiconductor with dominant point defects of oxygen vacancies and/or metal interstitials [45–47]. It is known that migration of ionic species through this non-equilibrated oxide film is the most dominant factor controlling the oxide film generation / annihilation reactions [36,48–51]. Various models were proposed to delineate passivation behavior and performance of the carbon steel in alkaline media. Power law model (PLM) offers an accurate approach to evaluate capacitance and thickness of passivated steel, by assuming normal distribution of resistivity in length of oxide film [36,52]. Point defect model (PDM) gives kinetic parameters of passivation that describes the distribution and migration of the ionic

species at metal/film/electrolyte [46,47,53,54]. This model considers point defects, including ions and vacancies, within passive film as charge carriers with semi-conductive properties [55–59]. As a result, point defects density and diffusion thorough oxide lattice govern growth and passive film break down [60–62].

Comprehensive studies were devoted to evaluating the role of microstructure modification on the corrosion performance improvement of carbon steel in alkaline solutions [15,31,35,63–65]. However, few electrochemical studies were conducted on understanding passivation parameters of improved steel microstructure [12,27,66]. Previous study of authors showed [35,64] that although SMAT remains high energetic distorted surface, leading to sever corrosion in acidic and neutral environment. Nonetheless, increasing time of treatment introduces superior corrosion performance compared to non-treated counterpart in chloride contaminated alkaline solution. This paper aimed to investigate the originate of such corrosion resistance through study of oxide film with EIS and passivation parameters addressed by PDM.

In this study, the surfaces of the carbon steel samples were sandblasted for 10 and 30 min, and after immersion in a high alkaline solution, the electrochemical properties of the passive film formed on their surfaces were examined under open circuit and elevated controlled anodic potentials conditions. Numerical and graphical techniques was used to extract equivalent circuit proposed by EIS data. Then, PDM was used to evaluate electronic and diffusivity of the formed passive film. Subsequently, the correspondence

between the grain refinement and passivation of Fe in examined alkaline solution was elaborated.

Materials and Experimental Procedures

All samples were prepared from an ASTM A572-50 carbon steel hot rolled plate with the main alloying elements of 1.35 wt.% Mn, 0.23 wt.% C, 0.4wt.% Si, 0.04wt.% S, 0.06wt.% V, 0.015wt.% Ni and 0.05 wt.% Co. Plates with the thickness of 4.5 mm and the dimensions of 90 × 25.4 mm were sandblasted under 350 kPa of air pressure by silica particles with an approximately diameter of 750 μm. The angle between the gun and the samples was kept 90o with a constant distance of approximately 20 mm and fixed moving velocity. Samples were sandblasted for 10 min. (SB10), and 30 min. (SB30). The reference (Ref) samples were wet abraded by SiC sandpapers with increasing size of grits from 240 to 1200, then followed by cleaning with alcohol to remove any contaminations and dried immediately with compressed air to reach a smooth surface without noticeable blemishes.

X-ray diffractometer analyses, operating at 40 kV and with CuKα radiation (λ=15418nm) was used to perform structural identification before and after sandblasting. The diffraction patterns were obtained in the range of 2θ=30–90° with the step size of 0.02°. Topmost surface crystallite size (D) was calculated through full width at half maximum on the intensity peaks, using the procedure suggested by Scherrer equation as follow [67]:

$$D = 0.9\lambda/\beta cos_\theta \quad (1)$$

where λ is wavelength, β is the width at half height of the peak, and θ is the Bragg angle.

For optical microscopy analysis, the cross-sections of the reference and SB samples were mounted with cold epoxy resin and then ground, polished and etched with 4% v/v nital solution. Samples were cut into smaller sections and a burial wire was brazed to one end of each section to establish electrical connection. All the edges, wire connection area, and the backside area were coated with epoxy, as shown in Figure 7-1. Coating provided a 10×10 mm exposure area. Samples were kept in a desiccator at room temperature before being used.

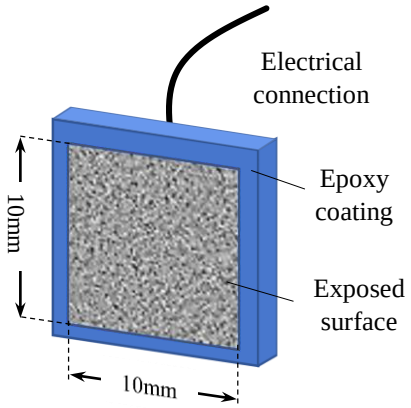

Figure 7-1. Epoxy coated steel sample.

Concrete simulated pore solution, with a pH of ~13.7 (composition given in [32]), was used as the high alkaline passivating environment. To ascertain reproducibility of experimental data, for each set of samples, a container with three identical samples was

prepared. Samples were immersed in the solution and the container was sealed to minimize the adverse effects of atmospheric carbonation that could lead to a decrease in the pH. A three-electrode measurement setup, including a steel sample as the working electrode, a SCE as the reference electrode, and a Pt mesh as the counter electrode, were used for the electrochemical tests.

Two set of experimental procedures were carried out in this study:

(i) Samples were immersed in the solution for 72h at their Open Circuit Potential (OCP) condition and the EIS were conducted within 72 h.

(ii) Samples were anodically (potentiostatic anodic) charged to different constant potentials for 12 h and Mott-Schottky (M-S) tests were conducted at each potential.

EIS measurements were performed with a 10 mV (peak to peak) sinusoidal potential perturbation over the frequency range from 1 MHz to 10 mHz. Differential capacitance measurements were carried out according to M-S theory in a frequency range between 20 kHz to 100 Hz with a perturbing sinusoidal signal of 10 mV. The potential scan was in the range of -0.6 to 0.4 vs. SCE with rate of 20 mV/s to satisfy the frozen-in defect assumption [68].

Results

Microstructure Evolution

Figure 7-1 and Figure 7-2 shows cross-sections and the surfaces of the sandblasted samples. Plastic deformation and flow of the smashed grains was observed at the vicinity of the surface, which became thicker proportionally to time of sandblasting. During this process, impingement of the sand particles induced plastic deformation on topmost surface with a high strain rate that decayed steeply from the surface toward the depth of the samples [18,19,23,69]. This variation along the surface to the depth of the samples was previously observed through microhardness [10,70,71] and scanning electrochemical microscopy [35].

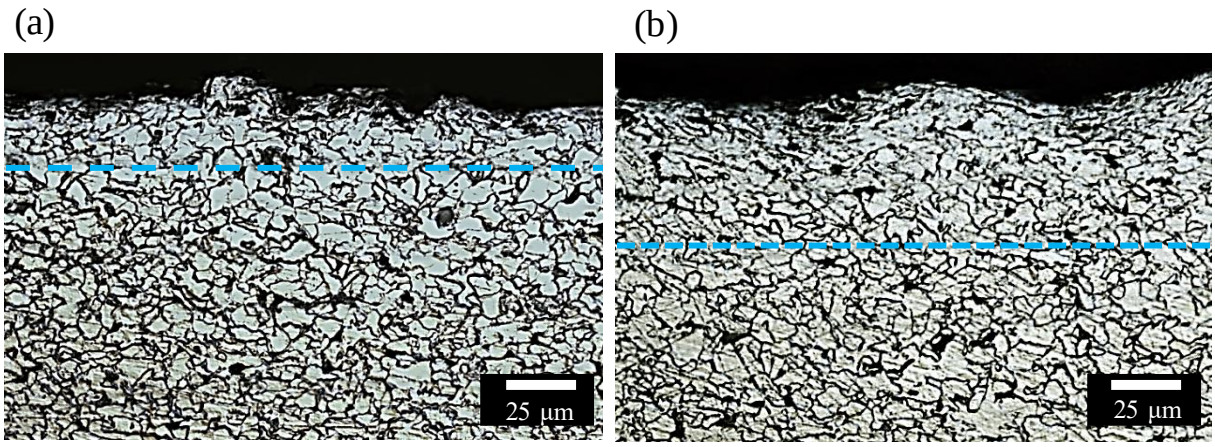

Figure 7-2. Microscopic images of the cross-section of the (a) 10 min. and (b) 30 min. sandblasted samples. The area above the dashed line indicated the deformed area.

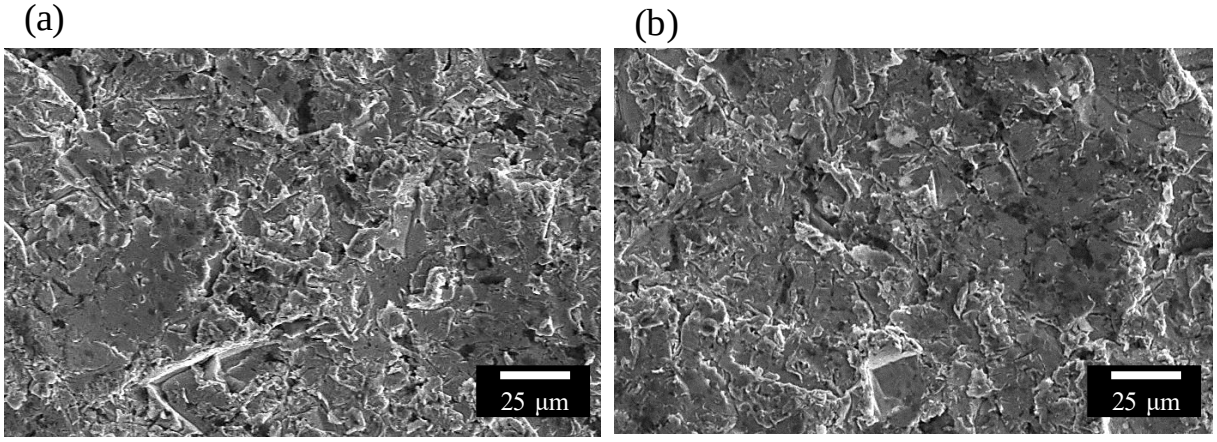

Figure 7-3. Scanning electron microscopy images of the surface of (a) 10 min. and (b) 30 min. sandblasted samples.

XRD patterns of the obtained from surface of the reference and the sandblasted steel samples are presented in Figure 7-4. All patterns mainly revealed iron phase and no apparent phase transformation was observed during sandblasting. Decreasing and broadening of the peaks were proportional to the time of sandblasting. This observation was attributed to the subdivision of coarse crystalline grains and formation of dense dislocation walls due to micro straining induced by repetitive solid particle impacts [18,19,72].

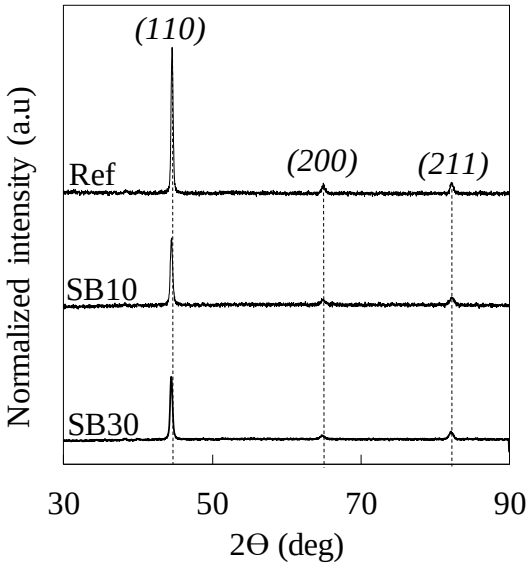

Figure 7-4. XRD patterns of the samples before and after sandblasting.

Table 7-1 listed the calculated equivalent grain sizes, using Eq. 1, and the average surface roughness of the samples obtained from three measurements. Longer time of sandblasting, progressively, accumulated dislocation gliding due to shear strain and subgrains formed on the surface of the samples which broadened the obtained Bragg reflection profile.

Table 7-1. Treatment conditions and average grain size of various samples.

Sample	Condition	Crystallite size (nm)	R_a(µm)	R_z(µm)
Ref	Ground surface finish	14000±3000	-	-
SB10	Sandblasted for 10 min	250±80	5.9	8.3
SB30	Sandblasted for 30 min	58±10	5.7	7.9

As shown in the micrographs in Figure 7-4, and elaborated in previous study [35], due to repeated multidirectional impact of the grits, the surface roughness stayed relatively constant. However, with increase of time of sandblasting, a considerable grain refinement occurred.

Electrochemical results

The open circuit potential values for the reference and sandblasted samples as a function of the immersion time in pore solution are shown in Figure 7-5. The most positive OCP values were recorded for the 30 min. sandblasted samples. During the first hour of immersion, the OCP values for the sandblasted samples decreased and started to become stabilized while the OCP for the reference samples increased and then stabilized. This behavior indicated a higher rate of oxidation than the reduction for the sandblasted samples compared to the reference sample, presumably due to dissolution and changes in stoichiometry of air formed oxide film on the surface those samples [25].

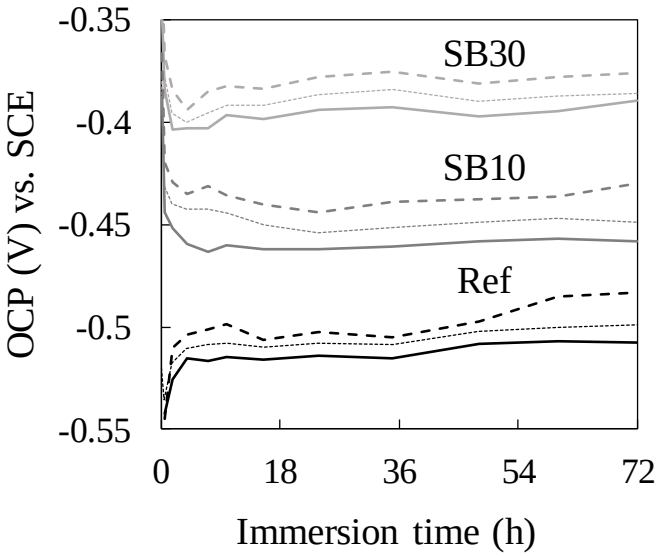

Figure 7-5. OCP values from three sample measurement of reference and sandblasted condition after 72 h immersion in pore solution.

However, by passing time, all the OCP values gently increased, indicating further formation and improvement of the passive film. This interval to reach stabilized passivity

was previously reported by the authors [32,73].

Figure 7-6 shows typical the EIS plots for the samples after 72 h immersion in the pore solution. Although the reference sample shows more impedances and higher phase angles absolute values at 10^2 to 10^3 Hz, an obvious increase in impedances modules can be observed at lower frequencies by applying sandblasting. Phase angle variation above 10^4 Hz, is attributed distribution of current and potential due to roughness and geometry [74-77].

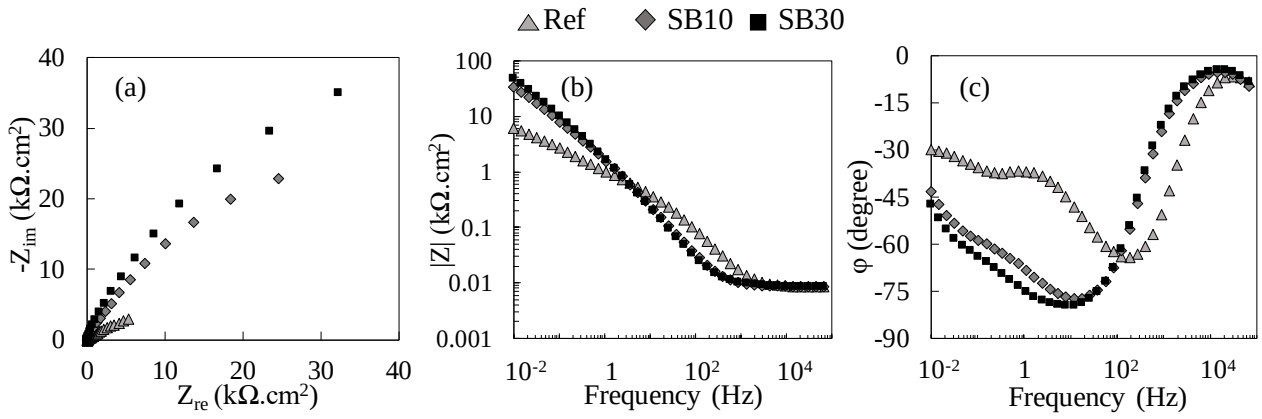

Figure 7-6. (a) Nyquist, (b) bode and (c) bode phase plots of the steel samples after 72 h immersion in the solution at their OCP.

Since the low frequencies of spectra show a curvature, two hierarchically distributed time constants are evident in phase angle plots. As suggested by Joiret et al. for a stationary steel with porous passive film formed at its OCP in high alkaline solution [40], the impedance results can be schematically ascribed to an equivalent circuit, shown in Figure 7-7. R_s is solution resistance in series with blocking electrode, Q_f, due to passive film, parallel to a branch consisted of a pore resistance, R_{pore}, in series with a

paralleled charge transfer resistance, R_t, and double layer dielectric, Q_{dl}, at the through-porosity. Constant phase element, CPE, was used to address non-ideal behavior and frequency dependent of capacitive behavior of dielectric element. Consequently, Q_f corresponds to the dielectric properties of the oxide film at high frequency range and describes the gradient of resistivity normal to the dielectric as proposed by Hirschorn et al. [36,52,78,79]. Q_{dl} is assigned to faradaic oxidation-reduction processes, take place at the surface of metal / double layer in lower frequencies which governed by the diffusion. Q_{dl} was used to describe variation of the time constant along the surface, as proposed by Brug et al. [80]. α_f and α_{dl} are CPE exponent, implying degree of frequency dispersion of time constants. Depending on α, Q represents a pure capacitance (α=1) or a pure resistance (α=0).

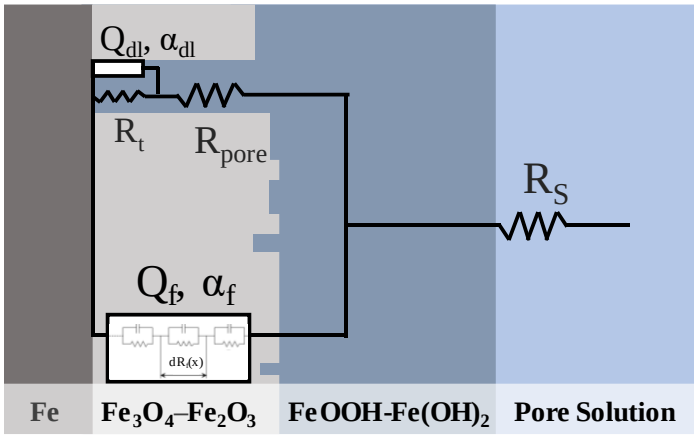

Figure 7-7. Physical interpretation of the impedance response of the surface of the carbon steel immersed in high alkaline solution at it OCP.

Accordingly, the results of the EIS measurements were fitted to the proposed circuit, using the simplex method described in [81]. The fitted values for different samples are listed in Table 7-2. In all cases, with repeated measurement, the Chi-Square

coefficient of χ^2 yields errors are less than of 1% between the fitted and experimental spectra, which show the goodness of fitting specifically in low frequencies [82]. It is worth noting that, the regression was performed at frequencies below 10^4 Hz to eliminate effect of geometry induced current and potential distribution. Evidently, surface modification through sandblasting, decreased the porosity and improved charge transfer resistance on the surface. Higher values of resistivity of the solution in the pores compared to the bulk solution resistivity can be attributed to the lower ionic concentration, narrower, and more torturous path, in the pores compared to the bulk solution [83].

Table 7-2 Values of the equivalent circuit elements for the reference, SB10 and SB30 samples passivated under OCP.

Sample	R_s ($\Omega.cm^2$)	R_{pore} ($k\Omega.cm^2$)	R_t ($k\Omega.cm^2$)	Q_f ($\mu F^{-1} s^{\alpha 1} cm^{-2}$)	Q_{dl} ($\mu F^{-1} s^{\alpha 2} cm^{-2}$)	α_f	α_{dl}
Ref	8.1	0.4	17.3	36.4	453.4	0.87	0.71
SB10	8.4	4.4	75.2	100.2	131.6	0.89	0.75
SB30	8.5	9.1	79.9	104.1	93.2	0.90	0.82

As mentioned before, the Q_{dl}, the double layer dielectric, corresponded to the variation of the time constant along the surface at the bottom of through-porosity on the conductive accessible surface of the electrode. To calculate the effective capacitance, C_{eff}, Brug equation was used [84]:

$$C_{eff} = Q_{dl}^{1/\alpha_{dl}} \left(\frac{1}{R_{pore}} + \frac{1}{R_t}\right)^{(\alpha_{dl}-1)/\alpha_{dl}} \quad (2)$$

This calculation yielded values of 22.5 $\times 10^{-5}$ F.cm^{-2}, 10.9$\times 10^{-5}$ F.cm^{-2} and 8.9$\times 10^{-5}$ F.cm^{-2} for Ref, SB10 and SB30, respectively. Dividing the effective capacitance of the sandblasted samples to reference samples, provided 0.48 and 0.39 for the SB10 and SB30, respectively. These values indicate the accessible surface area for SB10 and SB30 are 48% and 39% of than those for reference sample at the bottom of through the pores. This observation shows more protective oxide surface coverage and less porosity of protective oxide film due to grain refinement through sandblasting.

Under assumption of the PLM which was introduced previously, calculation of effective oxide film capacitance, C_f, needs boundary values of the oxide resistivity [36,52,78,79]. However, recently it was shown that the extrapolation of the complex capacitance at high frequencies can give reliable direct method to determine the C_f. Complex capacitance can be directly calculated using corrected impedance data as shown in Eq. 3:

$$C(\omega) = \frac{1}{j\omega(Z(\omega) - R_s)} \quad (3)$$

where j is the imaginary unit and ω is the angular frequency [85]. The obtained frequency dependent complex capacitance for the reference and sandblasted samples are shown Figure 7-8.

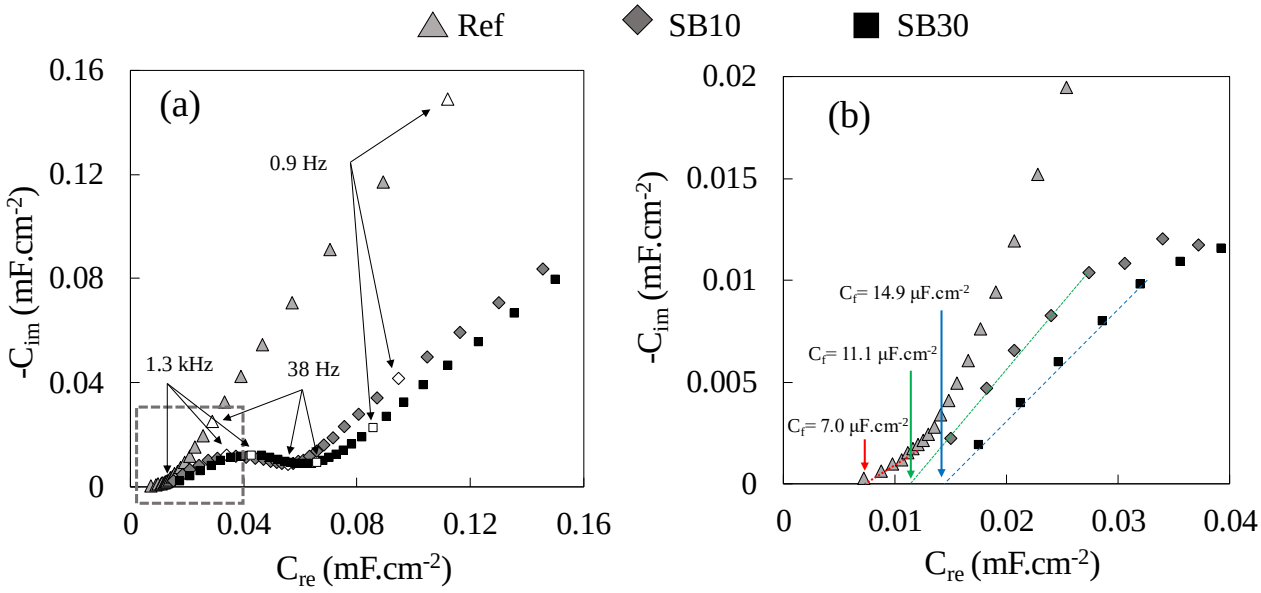

Figure 7-8. (a) Complex-capacitance diagrams obtained from EIS results shown in Figure 6 at high frequencies, (b) magnified rectangle region in (a).

As can be seen, the reference sample was more frequency dependent and capacitance abruptly raised by decreasing frequency compared to the sandblasted samples. This observation implied lower polarization resistance, more contribution of the charge carriers at the surface and consequently, faster relaxation of oxide film with double layer [86,87] of the reference sample compared to the sandblasted samples. Energy dissipation due to irreversible reaction in system is corresponded to C_{im} [88]. As a result, the pure capacitance due to the current leakage at the oxide/double layer can be estimated when $C_{im} \rightarrow 0$ at high frequencies. Accordingly, the effective oxide film capacitance, as shown in Figure 7-8 (a), increased by applying sandblasting and the time of sandblasting. The oxide film thickness (d_f) can be estimated using Eq. 4:

$$d_f = \frac{\varepsilon_0 \varepsilon}{C_f} \quad (4)$$

where $\varepsilon_0=8.85\times10^{-14}$ F.cm^{-1} and $\varepsilon = 12$ for dielectric constant of passive film on Fe in similar environment [36,52,89]. The average values of 1.7, 1 and 0.7 $\times10^{-9}$ m, from three measurements for each treatment, were obtained as the thickness of the passive film on the Ref., SB10 and SB30 samples, respectively. Estimated thickness of the oxide film for the reference sample is in agreement with the values reported in the previous studies [36,52].

As it was shown, in this study, the grain refinement led to decreasing the thickness of the passive film on the surface. It is well known that the grain boundaries act as the dominant defects in a crystalline structure due to their lower atomic densities and higher energy compared to the grain matrix [90-94]. Grain boundaries contribute in free energy which is proportional inversely to the grains size and directly to their population [95]. Increasing the surface activity through grain refinement, increased the nucleation sites with low energy barrier for oxidation. Thus, it was hypothesized that while the apparent thickness of the passive films on the sandblasted samples were thinner than that of the reference sample, the passive film formed on the sandblasted samples were more protective and less porous compared to reference sample.

To further verify this hypothesis, diffusion coefficient of the passive film for charge carriers under anodic passive range potential was estimated based on the procedure suggested by Ahn et al. for Fe in alkaline solution [62]. Based on PDM, this procedure considers transport of oxygen vacancies and/or metal interstitials charge

carriers as dominant point defect through the barrier oxide layer which leads stable generation / annihilation passive film [54]. Due to this controlled diffusion, under stabled anodic passivation, as illustrated in Figure 7-9, a continuous oxide film forms on the surface and acts as blocking electrode, which just allows passing small amount of DC current i.e i_{ss} [36,46,47]. Accordingly, the diffusivity of the point defect, D_o, can be written as:

$$D_o = \frac{i_{ss}}{4K\omega_2 e} \tag{5}$$

where e is the charge of an electron (1.602×10^{-19} C), K = $F\varepsilon_L/RT$, F is the Faraday constant, R is the gas constant, and ε_L corresponds to the mean electric field strength within the passive film which is 3.9×10^8 V/m for the passive film grown on iron [62]. ω_2 is the parameter which can be obtained from extrapolation of Eq. 6 and indicates the donor density, N_D, dependence with the passive film formation potential, E, as following [62]:

$$N_D = \omega_1 \exp(-bE) + \omega_2 \tag{6}$$

ω_1, ω_2, and b can be acquired from the exponential fitting of the donor densities versus film formation plot.

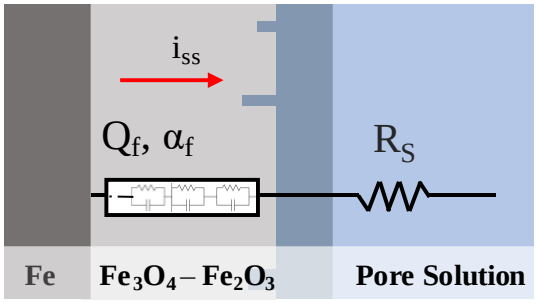

Figure 7-9. Physical interpretation of carbon steel interface immersed in high alkaline solution in the passivating potential field.

In order to estimate donor density in each passivating constant potential, each sample was charged potentiostatically for 12 h to reach i_{ss}, then differential capacitance measurement was performed to obtain space charge capacitance. Due to the presence of CPE on the oxide film, the same procedure, suggested to calculate C_f, was used to obtain C_{sc} [59]. Subsequently, donor densities for each passivation potential, can be obtained using Mott-Schottky equation [62,89]:

$$\frac{\partial C^{-2}}{\partial V} = \frac{2}{N_D e \varepsilon \varepsilon_0} \tag{7}$$

where N_D is the donor density.

Figure 7-10 shows the calculated donor and steady current densities for the reference and sandblasted samples at different passivating potentials.

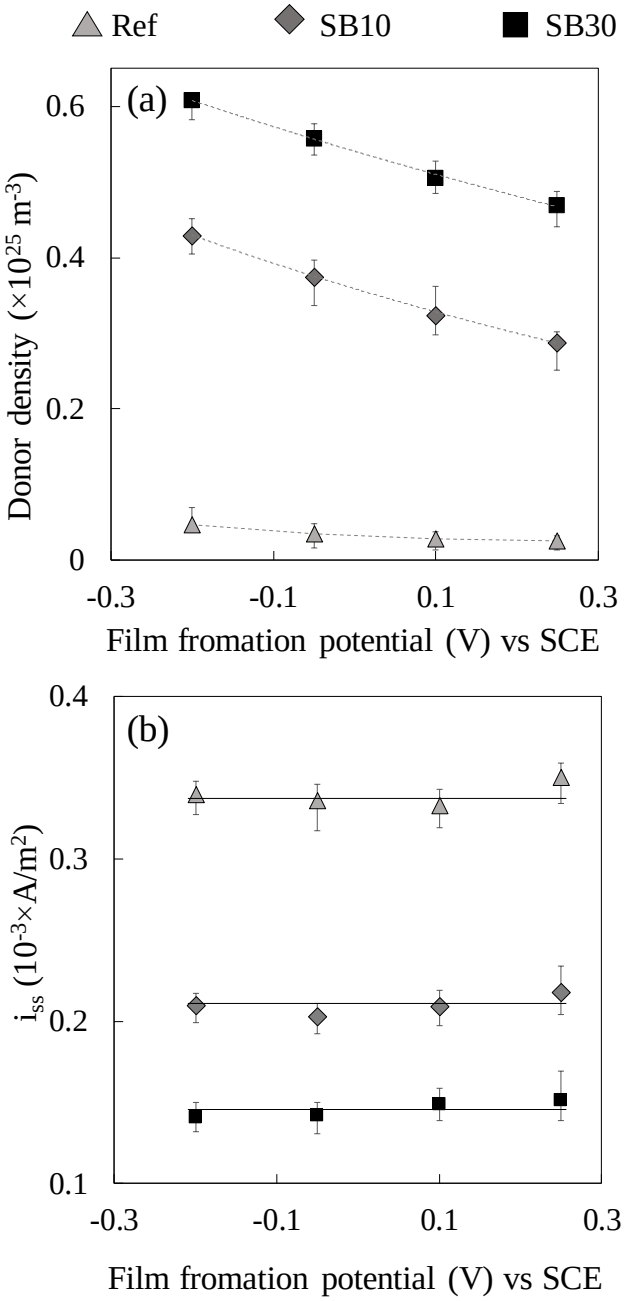

Figure 7-10. (a) Donor and (b) current density (i_{ss}) of the passive films formed on all reference and sandblasted carbon steel in the alkaline solution as a function of anodic polarization potential. Error bars show the max and min values from three measurements for each sample.

Table 7-3 lists the obtained parameters from Figure 7-10. Diffusivity values for charge carriers of the passive film formed on samples in the solution were estimated to be

approximately in the range of 10^{-20} - 10^{-21} m^2/s which are in agreement with the range, previously reported for similar materials and conditions [51,62,96]. While the N_D increased, as expected, both i_{ss} and D_o values decreased with decreasing the crystalline size, i.e. increasing time of sandblasting. The higher N_D for the sandblasted samples implied higher conductivity passive film/electrolyte formed on those samples compared to the reference sample. However, the lower i_{ss} on these samples compared to the reference sample indicated improvement of the passive film due to sandblasting process. This improvement was attributed to the formation of integrated, and less porous passive film of the sandblasted samples compared to the reference sample.

Table 7-3. Calculated parameters of Eq. 6 and 7 to obtain the diffusion of point defects in the passive film formed on the reference and sandblasted samples in the alkaline solution.

Sample	$\omega_1(10^{33}\ m^{-3})$	$\omega_2(10^{33}\ m^{-3})$	$b(V^{-1})$	$i_{ss}\ (10^{-3} A/m^2)$	$D_o\ (10^{-21} m^2/s)$
Ref	0.08	0.24	5.37	0.33	12.5
SB10	2.61	0.97	1.23	0.21	1.97
SB30	3.24	2.15	0.97	0.14	0.59

Discussion

As discussed in the passive film formation under OCP, surface grain refinement enhanced passive film integration and decreased its porosities. In grain refined surfaces, upon formation of the oxide film on the surface, the surface immediately blocked from access to the solution, which prohibit further Fe oxidization and film growth. This blockage increased by the degree of grain refinement due to formation of further grain boundary paths as preferable sites for oxide formation [9,12,13,20,97,98]. In contrast,

large pores on the oxide film of the reference sample still allowed solution to access the surface and consequently, discontinuous film growth continued. Thus, while the reference sample had thicker oxide film compared to the sandblasted samples, the inherent porosity along the oxide film led to lower protectivity on that sample compared to the surface modified samples.

Passivation under anodic current also showed the same abovementioned behavior. Applying anodic potential within the range of passivity, formed blocking oxide films, but with different electronic and electrochemical properties. As shown in Figure 7-10, although passive film formed on the sandblasted samples had higher donor density at interface of film/solution, but the lower steady currents were obtained, which even decreased by the time of sandblasting. This observation also implied that, the passive film on the grain refined surfaces were more impermeable due to formation of integrated and continuous passive film along the whole surface compared to that formed on the reference sample. The suggested mechanism is schematically depicted in Figure 7-11. It should be mentioned scales between grain, oxide film, thickness and distribution are only for comparison and do not show identical portion.

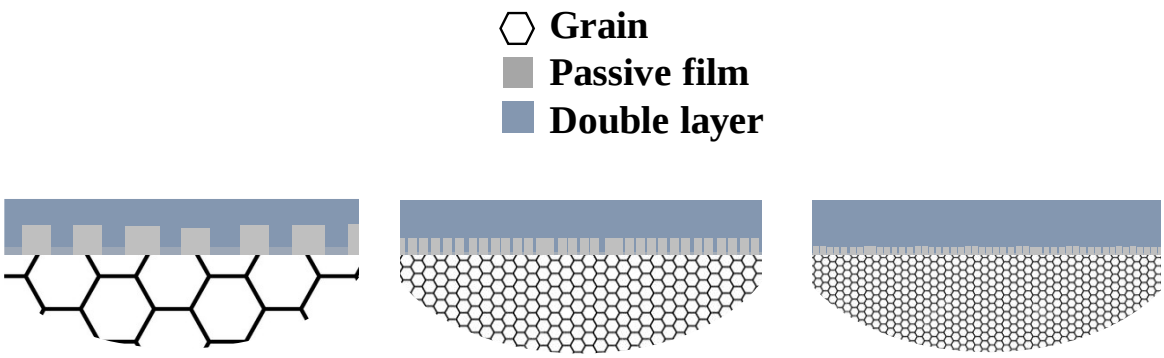

Figure 7-11. Evaluation of integrated Fe passive film in alkaline solution through grain refinement.

Conclusions

This paper discussed the influence of the surface mechanical attrition treatment as grain refinement method on the passivation of the carbon steel in an alkaline solution using electrochemical impedance spectroscopic analyses. Results showed that inducing severe surface strain and grain refinement, enhanced the formation and improved the integrity of the barrier oxide film. Based on the proposed equivalent circuits, the porosity and thickness of this barrier layer both decreased by increasing degree of grain refinement. Point defect diffusivity values clearly showed grain refinement decreased the ionic permeability of the passive film through continuous and integrated formation of a protective oxide film on the defective surface areas, i.e grain boundaries.

References

[1] A. Schreiber, C. Rosenkranz, M.M. Lohrengel, Grain-dependent anodic dissolution of iron, Electrochim. Acta. 52 (2007) 7738–7745. doi:10.1016/j.electacta.2006.12.062.

[2] S.C. Tjong, H. Chen, Nanocrystalline materials and coatings, Mater. Sci. Eng. R Reports. 45 (2004) 1–88. doi:10.1016/j.mser.2004.07.001.

[3] F. Saberi, B.S. Boroujeny, A. Doostmohamdi, A.R. Baboukani, M. Asadikiya, Electrophoretic deposition kinetics and properties of ZrO 2 nano coatings, Mater. Chem. Phys. 213 (2018) 444–454. doi:10.1016/j.matchemphys.2018.04.050.

[4] S. Pour-Ali, A.R. Kiani-Rashid, A. Babakhani, S. Virtanen, M. Allieta, Correlation between the surface coverage of severe shot peening and surface microstructural evolutions in AISI 321: A TEM, FE-SEM and GI-XRD study, Surf. Coatings Technol. 334 (2018) 461–470.

[5] S. Bagheri, M. Guagliano, Review of shot peening processes to obtain nanocrystalline surfaces in metal alloys, Surf. Eng. 25 (2009) 3–14.

[6] X. Tang, D.Y. Li, Production of alloyed nanocrystalline surfaces by combined punching, sandblasting and recovery treatments, Scr. Mater. 58 (2008) 1090–1093.

[7] R.K. Gupta, N. Birbilis, The influence of nanocrystalline structure and processing route on corrosion of stainless steel: A review, Corros. Sci. 92 (2015) 1–15.

[8] S. Pour-Ali, A.R. Kiani-Rashid, A. Babakhani, Surface nanocrystallization and gradient microstructural evolutions in the surface layers of 321 stainless steel alloy treated via severe shot peening, Vacuum. 144 (2017) 152–159.

[9] A. Fattah-Alhosseini, S. Vafaeian, Influence of grain refinement on the

electrochemical behavior of AISI 430 ferritic stainless steel in an alkaline solution, Appl. Surf. Sci. 360 (2016) 921–928.

[10] Z.B. Wang, J. Lu, K. Lu, Wear and corrosion properties of a low carbon steel processed by means of SMAT followed by lower temperature chromizing treatment, Surf. Coatings Technol. 201 (2006) 2796–2801.

[11] D.G. Li, Y.R. Feng, Z.Q. Bai, J.W. Zhu, M.S. Zheng, Photo-electrochemical analysis of passive film formed on X80 pipeline steel in bicarbonate / carbonate buffer solution, 254 (2008) 2837–2843.

[12] V. Afshari, C. Dehghanian, Effects of grain size on the electrochemical corrosion behaviour of electrodeposited nanocrystalline Fe coatings in alkaline solution, Corros. Sci. 51 (2009) 1844–1849.

[13] K.D. Ralston, N. Birbilis, C.H.J. Davies, Revealing the relationship between grain size and corrosion rate of metals, Scr. Mater. 63 (2010) 1201–1204.

[14] L. Wang, J. Zhang, Y. Gao, Q. Xue, L. Hu, T. Xu, Grain size effect in corrosion behavior of electrodeposited nanocrystalline Ni coatings in alkaline solution, Scr. Mater. 55 (2006) 657–660.

[15] D. Song, A. Ma, W. Sun, J. Jiang, J. Jiang, D. Yang, G. Guo, Improved corrosion resistance in simulated concrete pore solution of surface nanocrystallized rebar fabricated by wire-brushing, Corros. Sci. 82 (2014) 437–441.

[16] G. Liu, S.C. Wang, X.F. Lou, J. Lu, K. Lu, low carbon steel with nanostructured surface layer induced by high-energy shot peening, 44 (2001) 1791–1795.

[17] H.W. Zhang, Z.K. Hei, G. Liu, J. Lu, K. Lu, Formation of nanostructured surface

layer on AISI 304 stainless steel by means of surface mechanical attrition treatment, Acta Mater. 51 (2003) 1871–1881.

[18] N.R. Tao, Z.B. Wang, W.P. Tong, M.L. Sui, J. Lu, K. Lu, An investigation of surface nanocrystallization mechanism in Fe induced by surface mechanical attrition treatment, Acta Mater. 50 (2002) 4603–4616.

[19] K. Lu, J. Lu, Nanostructured surface layer on metallic materials induced by surface mechanical attrition treatment, Mater. Sci. Eng. A. 375–377 (2004) 38–45.

[20] T. Balusamy, S. Kumar, T.S.N.S. Narayanan, Effect of surface nanocrystallization on the corrosion behaviour of AISI 409 stainless steel, Corros. Sci. 52 (2010) 3826–3834.

[21] S. Kamps, W. Ensinger, F. Eder, A. Berndt, H. Zeininger, Processes and structures for generation of hydrophobic surfaces for large-scale and industrial operations, Appl. Surf. Sci. (2009) 92–95.

[22] R. Peng, L. Fu, L. Zhou, Improved wear resistance by phase transformation of surface nanocrystalline 1090 steel prepared by sandblasting technique, Appl. Surf. Sci. 388 (2016) 406–411.

[23] Y.N. Petrov, M.A. Vasylyev, L.N. Trofimova, I.N. Makeeva, V.S. Filatova, Layer wise evolution of the Cu – Zn alloy microstructure after sandblasting, Appl. Surf. Sci. 327 (2015) 1–6.

[24] K.D. Ralston, N. Birbilis, Effect of Grain Size on Corrosion : A Review, 66 (2010) 1–13.

[25] Y. Li, Y.F. Cheng, Effect of surface finishing on early-stage corrosion of a carbon steel studied by electrochemical and atomic force microscope characterizations, Appl.

Surf. Sci. 366 (2016) 95–103.

[26] L. Yuan, X. Chen, S. Maganty, J. Cho, C. Ke, G. Zhou, Enhancing the oxidation resistance of copper by using sandblasted copper surfaces, Appl. Surf. Sci. 357 (2015) 2160–2168.

[27] I.M. Gadala, A. Alfantazi, A study of X100 pipeline steel passivation in mildly alkaline bicarbonate solutions using electrochemical impedance spectroscopy under potentiodynamic conditions and Mott – Schottky, Appl. Surf. Sci. 357 (2015) 356–368.

[28] A. Poursaee, Corrosion of steel in concrete structures, in: Corros. Steel Concr. Struct., Elsevier, 2016: pp. 19–33.

[29] E.S. Meresht, T.S. Farahani, J. Neshati, Failure analysis of stress corrosion cracking occurred in a gas transmission steel pipeline, Eng. Fail. Anal. 18 (2011) 963–970.

[30] L. Hamadou, A. Kadri, N. Benbrahim, Characterisation of passive films formed on low carbon steel in borate buffer solution (pH 9 . 2) by electrochemical impedance spectroscopy, Appl. Surf. Sci. 252 (2005) 1510–1519.

[31] H. Torbati-Sarraf, A. Poursaee, Corrosion of coupled steels with different microstructures in concrete environment, Constr. Build. Mater. 167 (2018) 680–687.

[32] A. Poursaee, C.M. Hansson, Reinforcing steel passivation in mortar and pore solution, Cem. Concr. Res. 37 (2007) 1127–1133.

[33] S. Sharifi-Asl, D.D. Macdonald, A. Almarzooqi, B. Kursten, G.R. Engelhardt, A Comprehensive Electrochemical Impedance Spectroscopic Study of Passive Carbon Steel in Concrete Pore Water, J. Electrochem. Soc. 160 (2013) C316–C325.

[34] S.R. Yeomans, Coated Steel Reinforcement in Concrete, Corros. Manag. 3 (1994)

18–27.

[35] L. Ding, H. Torbati-Sarraf, A. Poursaee, The influence of the sandblasting as a surface mechanical attrition treatment on the electrochemical behavior of carbon steel in different pH solutions, Surf. Coatings Technol. 352 (2018) 112–119.

[36] S. Chakri, I. Frateur, M.E. Orazem, E.M.M. Sutter, T.T.M. Tran, B. Tribollet, V. Vivier, Improved EIS Analysis of the Electrochemical Behaviour of Carbon Steel in Alkaline Solution, Electrochim. Acta. 246 (2017) 924–930.

[37] P. Ghods, O.B. Isgor, J.R. Brown, F. Bensebaa, D. Kingston, XPS depth profiling study on the passive oxide film of carbon steel in saturated calcium hydroxide solution and the effect of chloride on the film properties, Appl. Surf. Sci. 257 (2011) 4669–4677.

[38] W.E.O. Grady, MSssbauer Study of the Passive Oxide Film on Iron, (1977).

[39] W. Xu, K. Daub, X. Zhang, J.J. Noel, D.W. Shoesmith, J.C. Wren, Oxide formation and conversion on carbon steel in mildly basic solutions, 54 (2009) 5727–5738.

[40] S. Joiret, M. Keddam, X.R. Nóvoa, M.C. Pérez, C. Rangel, H. Takenouti, Use of EIS, ring-disk electrode, EQCM and Raman spectroscopy to study the film of oxides formed on iron in 1 M NaOH, Cem. Concr. Compos. 24 (2002) 7–15.

[41] E. Volpi, A. Olietti, M. Stefanoni, S.P. Trasatti, Electrochemical characterization of mild steel in alkaline solutions simulating concrete environment, J. Electroanal. Chem. 736 (2015) 38–46.

[42] M.F. Toney, Atomic Structure of the Passive Oxide Film Formed on Iron, (1997) 1–4.

[43] M.R. Ryan, R.C. Newman, G.E. Thompson, An STM Study of the Passive Film

Formed on Iron in Borate Buffer Solution, 142 (1995) 177–179.

[44] H.B. Gunay, P. Ghods, O.B. Isgor, G.J.C. Carpenter, X. Wu, Characterization of atomic structure of oxide films on carbon steel in simulated concrete pore solutions using EELS, Appl. Surf. Sci. 274 (2013) 195–202.

[45] S.P. Harrington, F. Wang, T.M. Devine, The structure and electronic properties of passive and prepassive films of iron in borate buffer, Electrochim. Acta. 55 (2010) 4092–4102.

[46] M. Sánchez, J. Gregori, C. Alonso, J.J. García-Jareño, H. Takenouti, F. Vicente, Electrochemical impedance spectroscopy for studying passive layers on steel rebars immersed in alkaline solutions simulating concrete pores, Electrochim. Acta. 52 (2007) 7634–7641.

[47] M. Sánchez, J. Gregori, M.C. Alonso, J.J. García-Jareño, F. Vicente, Anodic growth of passive layers on steel rebars in an alkaline medium simulating the concrete pores, Electrochim. Acta. 52 (2006) 47–53.

[48] P. Ghods, O.B. Isgor, G. McRae, T. Miller, The effect of concrete pore solution composition on the quality of passive oxide films on black steel reinforcement, Cem. Concr. Compos. 31 (2009) 2–11.

[49] S. Sharifi-Asl, M.L. Taylor, Z. Lu, G.R. Engelhardt, B. Kursten, D.D. Macdonald, Modeling of the electrochemical impedance spectroscopic behavior of passive iron using a genetic algorithm approach, Electrochim. Acta. 102 (2013) 161–173.

[50] X. Zhang, J.C. Wren, I. Betova, M. Bojinov, Estimation of kinetic parameters of the passive state of carbon steel in mildly alkaline solutions from electrochemical impedance

spectroscopic and X-ray photoelectron spectroscopic data, Electrochim. Acta. 56 (2011) 5910–5918.

[51] T. Saario, Conduction Mechanism of the Passive Film on Iron Based on Contact Electric Impedance and Resistance Measurements, (2001) 0–7.

[52] Y. Chen, N.G. Rudawski, E. Lambers, M.E. Orazem, Application of Impedance Spectroscopy and Surface Analysis to Obtain Oxide Film Thickness, 164 (2017).

[53] M. Sánchez-Moreno, H. Takenouti, J.J. García-Jareño, F. Vicente, C. Alonso, A theoretical approach of impedance spectroscopy during the passivation of steel in alkaline media, Electrochim. Acta. 54 (2009) 7222–7226.

[54] T. Journal, T. Journal, C.Y. Chao, D.D. Macdonald, A Point Defect Model for Anodic Passive Films, (1983) 1874–1879.

[55] D. Macdonald, S. Biaggio, H. Song, Steady State Passive Films Interfacial Kinetic Effects and Diagnostic Criteria, J. Electrochem. Soc. 139 (1992) 170–177.

[56] D.D. Macdonald, Passivity–the key to our metals-based civilization, Pure Appl. Chem. 71 (1999) 951–978.

[57] D.D. Macdonald, M. Urquidi-Macdonald, Theory of Steady-State Passive Films, J. Electrochem. Soc. 137 (1990) 2395–2402.

[58] D.D. Macdonald, The Point Defect Model for the Passive State, J. Electrochem. Soc. 139 (1992) 3434.

[59] S. Marcelin, B. Ter-Ovanessian, B. Normand, Electronic properties of passive films from the multi-frequency Mott-Schottky and power-law coupled approach, Electrochem. Commun. 66 (2016) 62–65.

[60] Y.F. Cheng, J.L. Luo, Electronic structure and pitting susceptibility of passive film on carbon steel, 44 (1999) 2947–2957.

[61] S.J. Ahn, H.S. Kwon, Effects of solution temperature on electronic properties of passive film formed on Fe in pH 8 . 5 borate buffer solution, 49 (2004) 3347–3353.

[62] S.J. Ahn, H.S. Kwon, Diffusivity of point defects in the passive film on Fe, Passiv. Met. Semicond. Prop. Thin Oxide Layers. 579 (2006) 311–316.

[63] H. Torbati-Sarraf, A. Poursaee, Corrosion Improvement of Carbon Steel in Concrete Environment through Modification of Steel Microstructure, J. Mater. Civ. Eng. 31 (2019) 2–7.

[64] L. Ding, A. Poursaee, The impact of sandblasting as a surface modification method on the corrosion behavior of steels in simulated concrete pore solution, Constr. Build. Mater. 157 (2017) 591–599.

[65] B. Hadzima, Y. Estrin, H. Seop, Microstructure and corrosion properties of ultrafine-grained interstitial free steel, 462 (2007) 243–247.

[66] A. Poursaee, Temperature dependence of the formation of the passivation layer on carbon steel in high alkaline environment of concrete pore solution, Electrochem. Commun. 73 (2016) 24–28.

[67] B.D. Cullity, Elements of diffraction, 1978.

[68] N. Sato, Electrochemistry at Metal and Semiconductor Electrodes, Elsevier Science, n.d.

[69] H. Li, Y. Liu, M. Li, H. Liu, The gradient crystalline structure and microhardness in the treated layer of TC17 via high energy shot peening, Appl. Surf. Sci. 357 (2015) 197–

203.

[70] M. Jamesh, T.S.N. Sankara Narayanan, P.K. Chu, I.S. Park, M.H. Lee, Effect of surface mechanical attrition treatment of titanium using alumina balls: Surface roughness, contact angle and apatite forming ability, Front. Mater. Sci. 7 (2013) 285–294.

[71] B. Arifvianto, Suyitno, M. Mahardika, P. Dewo, P.T. Iswanto, U.A. Salim, Effect of surface mechanical attrition treatment (SMAT) on microhardness, surface roughness and wettability of AISI 316L, Mater. Chem. Phys. 125 (2011) 418–426.

[72] L. Zhou, G. Liu, X.L. Ma, K. Lu, Strain-induced refinement in a steel with spheroidal cementite subjected to surface mechanical attrition treatment, 56 (2008) 78–87.

[73] H. Torbati-Sarraf, A. Poursaee, Study of the Passivation of Carbon Steel in Simulated Concrete Pore Solution Using Scanning Electrochemical Microscope (SECM), Materialia. (2018).

[74] C.L. Alexander, B. Tribollet, M.E. Orazem, Contribution of Surface Distributions to Constant-Phase-Element (CPE) Behavior : 1 . Influence of Roughness, Electrochim. Acta. 173 (2015) 416–424

[75] S. Cattarin, M. Musiani, B. Tribollet, V. Vivier, Impedance of passive oxide films with graded thickness : Influence of the electrode and cell geometry, 54 (2009) 6963–6970.

[76] C.L. Alexander, B. Tribollet, M.E. Orazem, Contribution of Surface Distributions to Constant-Phase-Element (CPE) Behavior: 2. Capacitance, Electrochim. Acta. 188 (2016) 566–573.

[77] C.L. Alexander, B. Tribollet, M.E. Orazem, Influence of Micrometric-Scale Electrode Heterogeneity on Electrochemical Impedance Spectroscopy, Electrochim. Acta. 201 (2016) 374–379.

[78] M. Musiani, M.E. Orazem, N. Pébère, B. Tribollet, V. Vivier, Constant-Phase-Element Behavior Caused by Coupled Resistivity and Permittivity Distributions in Films, J. Electrochem. Soc. 158 (2011) C424.

[79] B. Hirschorn, M.E. Orazem, B. Tribollet, V. Vivier, I. Frateur, M. Musiani, L. Interfaces, U.P.R. Cnrs, U. Pierre, Constant-Phase-Element Behavior Caused by Resistivity, (2010) 458–463.

[80] G.J. Brug, A.L.G. van den Eeden, M. Sluyters-Rehbach, J.H. Sluyters, The analysis of electrode impedances complicated by the presence of a constant phase element, J. Electroanal. Chem. Interfacial Electrochem. 176 (1984) 275–295.

[81] M. Keddam, H. Takenouti, X.. Nóvoa, C. Andrade, C. Alonso, Impedance measurements on cement paste, Cem. Concr. Res. 27 (1997) 1191–1201.

[82] J.P. Phillips, R.C. Crowley, Characterization of the porosity of silicon nitride thin layers by Electrochemical Impedance Spectroscopy, Talanta. 9 (1962) 178–180.

[83] T. Barrès, B. Tribollet, O. Stephan, H. Montigaud, M. Boinet, Y. Cohin, Characterization of the porosity of silicon nitride thin layers by Electrochemical Impedance Spectroscopy, Electrochim. Acta. 227 (2017) 1–6.

[84] B. Hirschorn, M.E. Orazem, B. Tribollet, V. Vivier, I. Frateur, M. Musiani, Determination of effective capacitance and film thickness from constant-phase-element parameters, Electrochim. Acta. 55 (2010) 6218–6227.

[85] M. Benoit, C. Bataillon, B. Gwinner, F. Miserque, M.E. Orazem, C.M. Sánchez-sánchez, B. Tribollet, V. Vivier, Comparison of different methods for measuring the passive film thickness on metals, Electrochim. Acta. 201 (2016) 340–347.

[86] M. Itagaki, Y. Hatada, I. Shitanda, K. Watanabe, Complex impedance spectra of porous electrode with fractal structure, Electrochim. Acta. 55 (2010) 6255–6262.

[87] and K.W. Masayuki Itagaki, Satoshi Suzuki, Isao Shitanda, Electrochemical Impedance and Complex Capacitance to Interpret Electrochemical Capacitor, Electrochemistry. (2007) 649–655.

[88] P.L. Taberna, P. Simon, J.F. Fauvarque, Electrochemical Characteristics and Impedance Spectroscopy Studies of Carbon-Carbon Supercapacitors, (2003) 292–300.

[89] Y. Zhang, Q. Li, Electrochemical study on semiconductive properties of the passive film on rebar in concrete, J. Zhejiang Univ. A. 7 (2006) 1447–1452.

[90] K.L. Merkle, D.J. Smith, Atomic structure of symmetric tilt grain boundaries in NiO, Phys. Rev. Lett. 59 (1987) 2887–2890. doi:10.1103/PhysRevLett.59.2887.

[91] K.L. Merkle, Atomic Structure of Grain Boundaries, J. Phys. Chem. Solids. 55 (1994) 991.

[92] K.L. Merkle, D.J. Smith, Atomic Structure of Symmetric Tilt Grain Boundaries in NiO, Phys. Rev. Lett. 59 (1987) 2887–2890.

[93] J. Robertson, J.E. Forrest, Corrosion of carbon steels in high temperature acid chloride solutions, Corros. Sci. 32 (1991) 521–540.

[94] H. Torbati-sarraf, S.A. Torbati-sarraf, A. Poursaee, T.G. Langdon, Electrochemical behavior of a magnesium ZK60 alloy processed by high-pressure torsion, Corros. Sci.

(2019) 1–11.

[95] M. Nastasi, D.M. Parkin, H. Gleiter, eds., Mechanical Properties and Deformation Behavior of Materials Having Ultra-Fine Microstructures, Springer Netherlands, Dordrecht, 1993.

[96] Y.F. Cheng, C. Yang, J.L. Luo, Determination of the diffusivity of point defects in passive films on carbon steel, Thin Solid Films. 416 (2002) 169–173.

[97] S. Gollapudi, Grain size distribution effects on the corrosion behaviour of materials, Corros. Sci. 62 (2012) 90–94.

[98] P.K. Rai, S. Shekhar, K. Mondal, Development of gradient microstructure in mild steel and grain size dependence of its electrochemical response, Corros. Sci. 138 (2018) .

CHAPTER 8

Electrochemical behavior of a Magnesium ZK60 alloy processed by high-pressure torsion[1]

Introduction

Magnesium alloys are desirable choices as lightweight materials for energy or fuel conservation and biomedical applications; Nevertheless, the main factors currently limiting a wider use of Mg products are the difficulties in processing these alloys, the relatively low strength and ductility, and the extremely high reactivity and poor corrosion resistance in various working environments [1-3]. Recent studies attempted to address these difficulties with the objective of improving either the mechanical or the corrosion properties but relatively few studies have considered the mutual impact of these properties on each other [4]. In practice, both properties are linked to the alloy composition and microstructure and this originates from the manufacturing process [5] and therefore needs to be considered synergistically.

Severe plastic deformation (SPD) is an effective method for improving the mechanical properties of Mg alloys. Processing by SPD causes grain refinement, a

[1] HamidrezaTorbati-Sarraf, Seyed Alireza Torbati-Sarraf, AmirPoursaeea, Terence G.Langdon, Corrosion science, 2019.

redistribution of solutes and changes in the crystallographic orientations within the microstructure which may also have a significant impact on the corrosion properties. To date, there are number of recent studies examining the influence of SPD processing on the corrosion behavior of Mg and its alloys [5-12]. Theoretically, the grain boundaries appear more active than the bulk, therefore, grain refinement leads to a more susceptive surface [13]. However, other modifications such as the grain size distribution [14] and the evolution of anisotropic texture [5,11,12,15,16] may also occur simultaneously with the grain refinement and this may play a more critical influence on the corrosion behavior of the Mg alloys.

The deformation capabilities of Mg alloys through conventional processing are poor due to their hexagonal close-packed (HCP) structure and this means that the processing is generally conducted at relatively high temperatures. However, high-pressure torsion (HPT) is an SPD process that has an established capability in producing significant grain refinement in a range of Mg alloys and, more important, the processing can be effectively conducted at room temperature without the development of segmentation or cracking in the base metal [17,18]. Although the effect of various SPD processes on corrosion of magnesium was investigated thoroughly [5,6,8,12,19-21], nevertheless little attention was devoted to the development of electrochemical behavior in the HPT-processed Mg alloys [9,10,22-24] where reports have centered mainly on noting that more refined grains lead to a more homogenous corrosion. In practice, processing by HPT permits a study of corrosion behavior over a wide range of grain sizes

and grain size distributions [25,26].

Earlier investigations of authors on the ZK60 Mg alloy showed that HPT induced an inhomogeneous strain along the radius of samples by torsional straining and, as a result, the average grain size and the mechanical properties tended to vary along the radius of the samples but an almost homogeneous microhardness distribution with finer grain size and reasonable uniformity was attained after higher numbers of HPT turns [27-29]. The mechanical and thermal stability behavior of ZK60 after HPT was evaluated recently by the current authors [30,31] but it is imperative to study the electrochemical behavior of the refined ZK60 alloy. Accordingly, this research was initiated to assess the electrochemical and semiconductive oxide layer behavior of the ZK60 Mg alloy after processing through HPT with different numbers of turns and to make a direct comparison with the behavior of extruded material.

Experimental Procedures and Materials

Materials

A commercially available ZK60 Mg alloy with a composition (in wt.%) of 5.5 % Zn, 0.5 % Zr was used in this study in the form of extruded rods. The rods with diameters of 10 mm were sliced into disks having thicknesses of approximately 1.2 mm and then both sides of each disk were abraded with SiC papers to achieve smooth surfaces with

uniform final thicknesses of approximately 0.8 mm.

HPT Processing

The HPT processing was conducted using a facility with a rotating lower anvil and stationary upper anvil and the experiments were carried out under quasi-constrained conditions [32]. The torsional strain was applied to the disks by rotating the lower anvil under an applied pressure of 2.0 GPa at a constant speed of 1 rpm. The HPT-processed disks were prepared through total numbers, *N*, of 1, 2, 5, 10 and 20 turns. Post-inspection of the processed disks revealed no cracking or signs of damage by HPT processing.

Electron Back-Scatter Diffraction (EBSD) Sample Preparation

Samples were prepared for electron back-scatter diffraction (EBSD) with a JEOL IB09010CP ion beam cross-sectional polishing machine for 5 h at an operating voltage of 6 kV. A scanning electron microscope (SEM) JEOL JSM-7001F was used at an operating voltage of 7 kV and orientation imaging microscopy (OIM) was employed to record the experimental data. A minimum of 2000 grains was examined for measurements of the average grain size and the grain size distributions. In subsequent descriptions, ND, RD, and TD correspond to the Normal Direction (torsion axis), Radial Direction, and

Tangential Direction, respectively. The crystallographic plane of {0001} in the EBSD images was used to evaluate textural evolutions of the materials with the pole figures. The EBSD images were recorded from the semi-oval areas of samples in the mid-radius of the TD-RD plane at the near surface position of the disks. Earlier studies provide a more detailed description of the sample preparation for EBSD [33,34].

Electrochemical Testing

All of the electrochemical tests were carried out at room temperature in a 0.1 M NaCl aqueous solution. Prior to exposure to the solution, samples were sequentially wet ground with 800 and 1200 grit SiC abrasive papers, washed with distilted water and alcohol and then dried immediately. A SCE and a platinum mesh were used as the reference and the counter electrodes, respectively. Extruded and HPT processed samples were used as the working electrode.

To stablish the electrical connection for electrochemical tests, wires were glued to one side of each processed disk. In order to conduct overall examination on the electrochemical behavior of ZK60 Mg alloy processed with different number of HPT turns, the whole surfaces of the samples were exposed to the solution. Therefore, the edges, back side and the connection were coated with epoxy to minimize any undesirable effects. To achieve a quasi-steady open circuit potential (OCP), the samples were immersed in the solution for approximately 200 min. Then, EIS was performed with a sinusoidal potential amplitude of 5 mV versus the OCP over the frequency range of 100

kHz to a few mHz. At 30 min. after the EIS test, potentiodynamic polarization was carried out over a potential range from -2.0 V to 0 V versus SCE with a scan rate of 1 mV/s.

In order to assess the semiconductive and the capacitive behaviors of the oxide layer formed on the surface of the disks, the same sample from the polarization test was again ground and prepared for OCP and EIS similar to the earlier procedure and afterwards the Mott–Schottky test was carried out on the sample by employing staircase potential electrochemical impedance spectroscopy (SPEIS) with 5 mV AC perturbation at selected frequencies from 100 kHz to 100 Hz in a variable potential from -2.0 to -1.6 V vs SCE during a 10 mV/s scan rate. The time of immersion was selected based on the results of the hydrogen evolution test.

Quasi-steady behavior in the H_2 evolution was observed after about 4 h immersion in the solution as will be discussed later. Under OCP conditions, the corrosion rate can be measured from the rate at which H_2 evolution occurs on the corroding surface [35]. The collection of hydrogen gas is widely used to evaluate Mg alloys corrosion rate [4,36-38]. The H_2 gas bubbles produced as a result of the dissolution of Mg are collected with an inverted funnel inside the solution and conveyed to a volumetric burette [35]. Therefore, the volumetric measurement of the evolved hydrogen gives good trend for measurement of the weight loss of the metal [39]. However, for low rates of corrosion, as in the case investigated in this study with relatively mild corrosivity, this technique tends

to underestimate corrosion rare [40]. Consequently, in this study, the volume of evolved hydrogen obtained from direct measurements was used to monitor and compare the activity of HPT processed samples with different numbers of turns during 24 h. In this experiment, the whole surface of disk-shaped extruded and HPT samples, with diameters of approximately 10 mm, were immersed in the solution with a volume per unit surface area of 100 $ml.cm^{-2}$.

The surfaces of the samples after 4 h exposure to the solution were observed using an optical microscope with images taken from different locations and then positioned together in order to form a complete image of the sample. This procedure was repeated for 10 and 24 h of immersion to provide a pictorial presentation of the corrosion process over the total exposure time. Ultimately, the corroded surfaces after 24 h exposure were examined and the morphology and composition of the surfaces were analyzed with scanning electrochemical microscopy and energy dispersive spectroscopy (EDS). In order to achieve reliable reproducibility of the measurements, all the electrochemical tests were conducted on three different samples.

Experimental Results

Effect of HPT Processing on Microstructural and Textural Evolution

EBSD analysis provides an overall evaluation of grain size and grain size

distribution during the HPT process. A summary of the analysis with examples of OIM maps are configured in Figure 8-1. All the data were obtained from the mid-radius of each disks including the unprocessed condition and after processing by HPT through one and five turns.

It is apparent from these results that processing by HPT reduces the grain size from an initial value of several microns to a final average value of ~700 nm after processing for five turns. It should be noted that further EBSD analysis with even more HPT turns was not possible due to the extreme deformation imposed on the samples after 10 and 20 turns. Thus, samples with high numbers of HPT turns hardly revealed any Kikuchi bands and consistently exhibited a low confidence index (CI) for visualization of the microstructure in the EBSD images.

Observations of the microstructural evolution during HPT processing revealed that the grain size distribution stretched over one order of magnitude of the grain size for all experimental conditions. Nevertheless, there is a gradual decrease in the average grain size values by increasing the number of HPT turns. These observations were extensively described for the same processed materials in earlier studies of the grain size evolution with bimodalities in the grain size distributions in ZK60 Mg alloys processed by HPT [18,27,28,41].

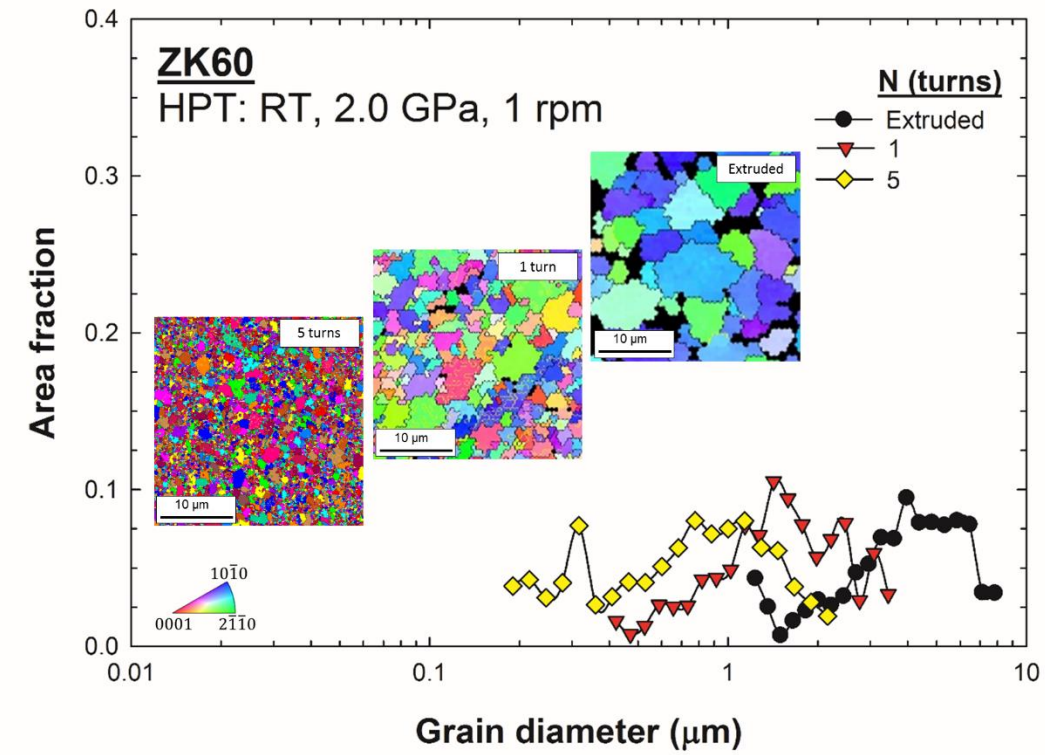

Figure 8-1. Grain size distributions and EBSD orientation micrographs taken from the mid-radius of the RD-TD planes of the extruded material and samples processed by one and five turns of HPT. The color coded triangle is reprsentative of the crystalograpic orentation of corresponding colors in the EBSD orentation micrographs.

In practice, the grain size and the texture both change with straining of the material. The pole figures obtained from <0001> crystallographic orientation are shown in Figure 8-2 for the extruded condition and after one and five turns. By increasing the number of HPT turns, a gradual change towards basal planes, {0001}, is evident with the c-axis parallel, or close to parallel, to the normal direction to the torsion axis or the surface exposed to the corrosive environment. This result is consistent with the earlier studies of the texture behavior of HPT processed ZK60 Mg alloy with XRD method [41].

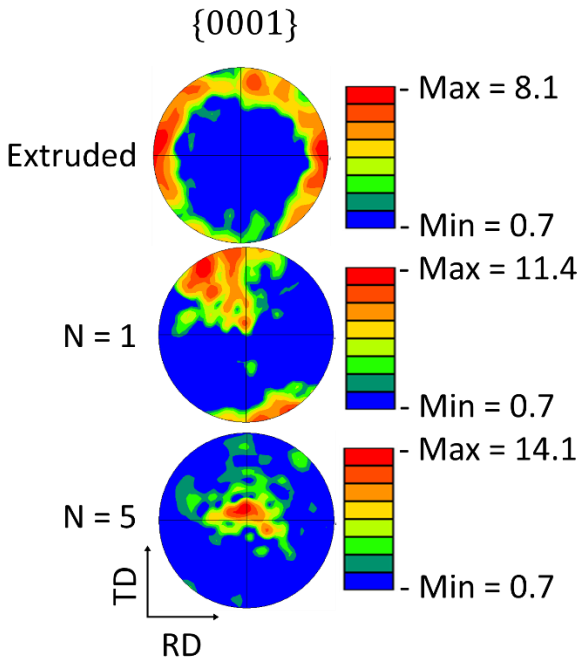

Figure 8-2.The pole figures of {0001} crystallographic orientation from the mid-radius of the RD-TD planes of the extruded, and HPT processed samples with one and five turns at 298 K.

Electrochemical Testing of HPT-Processed Materials

The potentiodynamic polarization curves of the extruded and HPT processed samples after ~4 h of immersion in a 0.1 M NaCl solution are shown in Figure 8-3. It is readily apparent that the stages of the cathodic reactions, with hydrogen evolution as the main reaction, are very similar for all samples up to and including 20 turns and thus there is no significant influence of the HPT process on the kinetics of the cathodic reactions at high cathodic overpotentials [43].

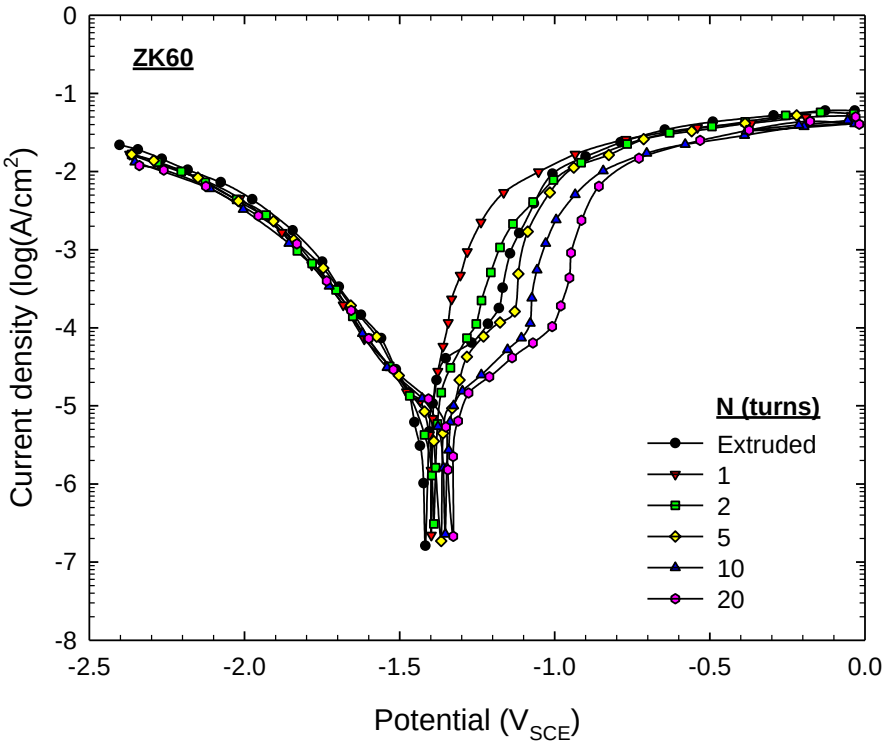

Figure 8-3.The Polarization curves of the ZK60 samples in 0.1 M NaCl solution, processed by extrusion and various numbers of HPT turns.

However, the E_{corr} values of the HPT processed samples are ~100-150 mV which is more noble than the extruded sample, presumably due to the formation of a nobler crystallographic texture towards the basal planes [5,8,11,44] after HPT processing. Nevertheless, E_{corr} does not change significantly by increasing the numbers of turns from 5 through to 20. The kinetics of the anodic dissolution of the HPT-processed samples showed inconsistent behavior because for one and two turns the anodic current increased with an increase of potential whereas for 5, 10 and 20 turns there were apparent pseudo passive window trends. This behavior is attributed to the formation of partially protective

corrosion products on the surface of disks [5,11,45].

This potential increased with the increase in the number of turns, showing an enhancement in the adhesion and protectiveness of the film formed on the surface of the ZK60 alloy by increasing numbers of turns during HPT. However, with the potential increment, the quasi-protective film is prone to lose its integrity and break down and subsequently it is expected that the current density starts to increase, thereby implying the free dissolution of Mg and the evolution of H_2 bubbles [39,43,46,47].

A reliable analysis of the corrosion of Mg and its alloys by conventional DC electrochemical methods, such as with polarization, requires both half-cell reactions are controlled by activation polarization [37]. In studies of the corrosion of Mg alloys, hydrogen evolution occurs through both anodic and cathodic polarizations which increase the ohmic potential and makes it difficult to compensate [36,48]. In addition, except in activation-controlled kinetics, polarization curves do not show linear behaviors which makes it more difficult to conduct and comprehend the analysis [49,50]. Furthermore, the products formed on the surface during corrosion may lead to significant deviations in the reactions from the OCP [39,50-52]. Thus, in studying the corrosion of Mg alloys, instant corrosion rate determinations using the DC electrochemical method is difficult and should be accompanied by an AC electrochemical technique and a non-electrochemical technique such as a hydrogen collection method [35,52,53].

The Nyquist spectra obtained from the EIS experiment for one of the samples of each group in a 0.1 M NaCl solution are shown in Figure 8-4. All EIS spectra contain one high and one medium frequency capacitance loop and one inductive loop at the low-frequency. Evidently modification of the impedance with increasing the turns of HPT can be attributed to the improvement and integrity of the $MgO/Mg(OH)_2$ oxide layer [52-55]. The corrosion of magnesium in an aqueous solution can be described by the following net reactions [46,51,56,57] shown in Eq. 1-4:

$$Mg \rightarrow Mg^{+}_{ads} + e^{-} \quad (1)$$

$$Mg \rightarrow Mg^{2+}_{ads} + 2e^{-} \quad (2)$$

$$Mg^{+}_{ads} + H_2O \rightarrow Mg^{2+} + OH^{-} + 1/2H_2 \quad (3)$$

$$Mg^{2+} + 2OH^{-} \rightarrow Mg(OH)_2 \quad (4)$$

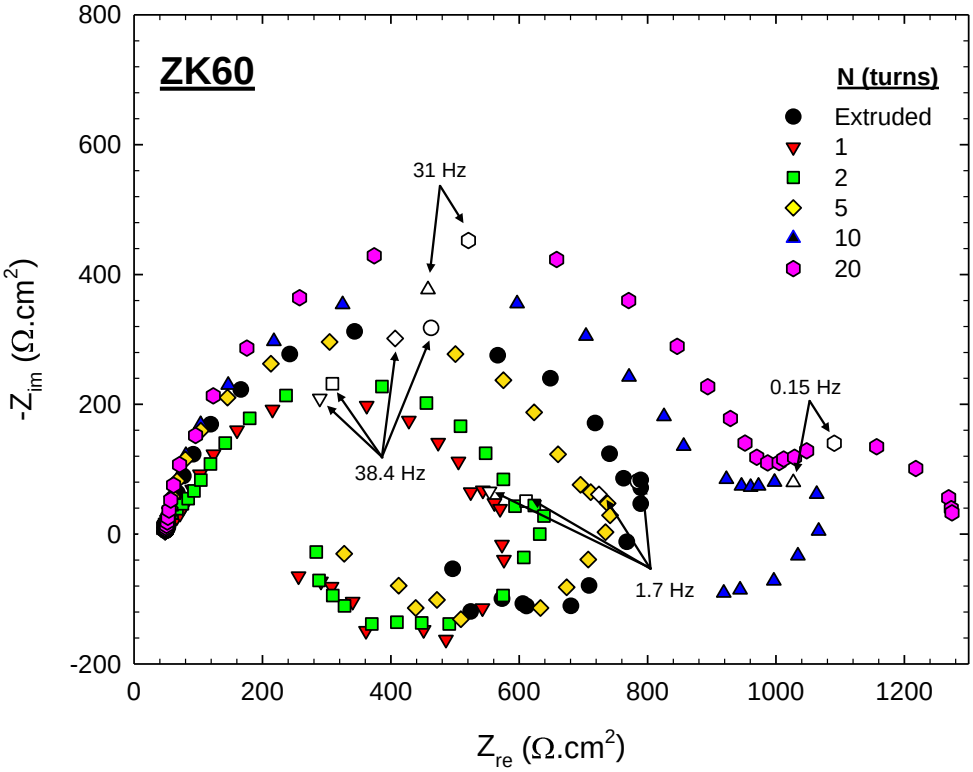

Figure 8-4. Nyquist plots of one of the ZK60 Mg samples in 0.1 M NaCl solution, processed by extrusion and various numbers of turns by HPT.

The relaxation processes of adsorbed species, $Mg(OH)_2$, cause the formation of the inductive loop at the low-frequency domain [51,53,55]. The mass-transport loop, second capacitance loop, in the medium-frequency range is attributed to the diffusion of Mg^{2+} through the porous $Mg(OH)_2$ corrosion product layer which is not compact but covers entirely the surface and allows easy penetration of aggressive ions [54,58]. Subsequently, the inner oxide layer composed of MgO is formed progressively in equilibrium as follows [54,56]:

$$Mg(OH)_2 \leftrightarrow MgO+H_2O \quad (5)$$

This appears in the high-frequency (HF) capacitive loop as a result of both charge

transfer and film effect [52,54,55,58,59].

Based on the described proposed mechanism which also observed in other studies [54,58,60,61], an equivalent electrical circuit, shown in Figure 8-5, is used to elaborate the interface interaction.

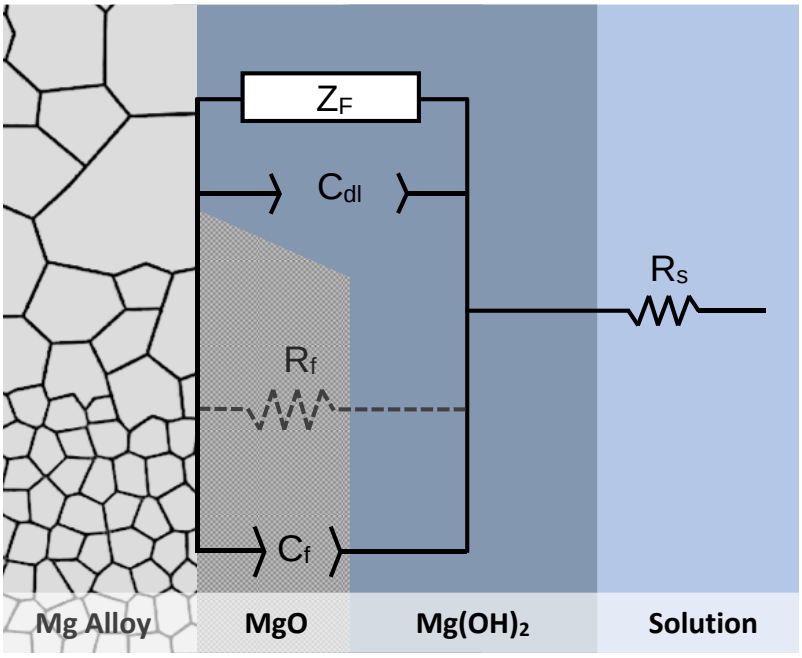

Figure 8-5. Equivalent circuit constructed based on the interface reactions observed in the EIS spectrum for the extruded and the HPT processed ZK60 samples in 0.1 M NaCl.

R_s corresponds to the solution resistance and was placed in series with all other elements. Since Mg dissolution mostly occurs at the film-free or porous areas [54,58], then a faradaic impedance, Z_F, in parallel with the double layer capacitance, C_d, ascribes production of Mg ions and the precipitation of a $Mg(OH)_2$ porous layer. In parallel, C_f and R_f are attributed to the MgO inner oxide film capacitance and resistance, which are assumed to be very protective compared to the outer $Mg(OH)_2$ layer [54]. R_f is depicted

by a dashed line since it has no sensitive impact on the low frequency faradaic impedance. Therefore, R_f can be placed equal to the high frequency impedance part of the Nyquist, $R_{HF} \simeq R_f$ [55,60].

The obtained Nyquist spectra are not perfect semicircles and cannot be used for direct determination of the capacitive behavior of the corroded surfaces. This imperfection in the Nyquist spectra is attributed to the electrode geometry, inhomogeneity in microstructure, reactivity and resistivity in length of the adsorptive and oxide layer. As a result, using a constant phase element (CPE) is a proper approach to the non-ideal capacitances [58, 62-65].

The capacitance of an oxide film can be graphically determined by extrapolating the high frequency real capacitance, $C_f \simeq C_{HF}$, using the Cole-Cole capacitance representation [52,66,67]. A complex capacitance can be calculated directly using Eq. 6:

$$C(\omega) = \frac{1}{j\omega(Z(\omega)-R_S)} \quad (6)$$

where $j^2 = -1$ and ω is angular frequency [66]. R_s can be accurately obtained by extrapolation of the Nyquist plots with Z_{re} axis at high-frequencies [68]. Figure 8-6 shows the complex capacitance plots obtained from the EIS data. Applying the HPT process changes the behavior of the oxide film formed on the samples. Evidently, 1 and 2 HPT processed samples are more responsive to higher frequencies compared to the other

samples, indicating CPE behavior along the surface due to the surface heterogeneity and geometrical effects [58]. The values of R_f and C_f obtained by the graphical method are given in Table 8-1. Although, this methodology yields a slight overestimation of the capacitance values [52,66,69], it provides a qualitive comparison. By applying the HPT processing, the film resistance increases in the order of 1 < 2 < 5 < Extruded < 10 < 20 HPT turns. However, the C_f values show a different trend. By applying HPT, C_f first decreased and then gradually increased by a number of HPT turns. Assuming that the oxide film thickness is proportional to the reciprocal of the capacitance ($1/C_f$) of the oxide film [66], the trend obtained implies that applying the HPT forms a thicker oxide film on the surface of the electrode; but it becomes thinner by increasing turns of HPT.

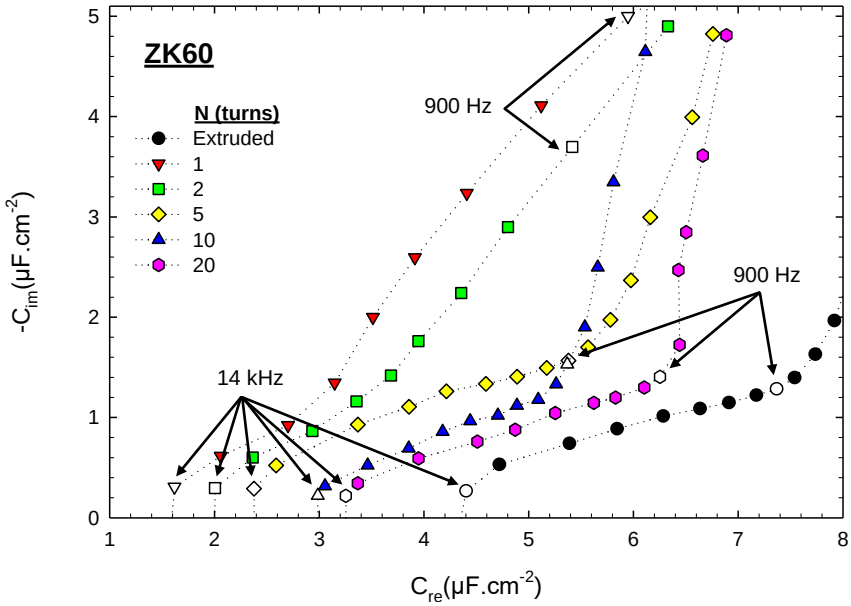

Figure 8-6. Cole-Cole plots corresponding to EIS data at high frequencies presented in Figure 8-4.

Table 8-1. graphically obtained value of EIS.

Sample	Extruded	**1**	**2**	**5**	**10**	**20**
R_f (Ωcm^2)	760	510	590	680	870	980
C_f ($\mu F cm^{-2}$)	4.2	1.6	1.9	2.3	2.9	3.2

It is hypothesized that the protective oxide film is not able to continuously cover the entire surface due to the small Pilling-Bedworth (PB < 1) ratio for MgO [37,52]. In addition, the presence of Cl^- ions in solution makes the surface susceptible to localized attack. Hence, despite the formation of a thicker oxide film on the HPT-processed samples with small numbers of turns compared to the other sample, this oxide film does not provide continuous coverage and resistance on the entire surface and leads to the formation of micro-galvanic cells between the covered and uncovered areas. Accordingly, the introduction of grain refinement through the initial turns of HPT generally reduces the corrosion resistance compared to the extruded sample. However, increasing the numbers of turns of HPT improves the corrosion resistance through the formation of a modified and integrated MgO film. This trend is consistent with increasing impedance of the oxide film and the pseudo-passive potential behavior observed at the polarization curves.

Electronic properties of the oxide film formed on Mg interface has significant role on its corrosion performance [70]. Charge carriers in the formed oxide film have different electrochemical potentials with respect to the solution [71], and this creates a space charge layer with a capacitance at Mg interface. The charge carrier density (N_q) of the oxide film can be extracted using Mott-Schottky equation:

$$\frac{1}{C^2} = \pm \frac{2}{\varepsilon \varepsilon_0 e N_q A^2} \left(V - V_{fb} - \frac{kT}{e}\right) \quad (7)$$

where ε is the dielectric constant of the corrosion products (for MgO this value is ~9.62),

ε_0 represents the permittivity of vacuum (8.854×10^{-14} F/cm), A is the area of the exposed surface, V is the applied potential, V_{fb} is the flat band potential, e is the charge of the electron (1.602×10^{-19} C), k is Boltzmann's constant (1.38×10^{-23} J/K), T is the absolute temperature (298 K) [73-75]. The interfacial capacitance, C, can be equaled to space charge capacitance of oxide film by neglecting capacitance of Helmholtz layer which is generally one order of magnitude higher than C_{ox} [55,60,70].

To ascertain the formation of a continuous oxide layer and make comparison with EIS data in OCP, prior to conducting the Mott-Schottky tests, samples were exposed in the 0.1 M NaCl solution for 4 h immersion. As discussed earlier, CPE was observed in the dielectric properties of the oxide film. As a result, capacitance and accounted charge carrier density may also vary with the frequency. Nonetheless, applying multi-frequency capacitance measurements at relatively high frequencies (f > 100Hz) and high scan rate (10 mV/s) and extrapolating equivalent film capacitance provide precise calculation for Mott-Schottky plot [72]. Therefore, EIS spectra were analyzed for certain steps of potential and C values were graphically estimated with the same procedure explained for calculating the C_f. Mott-Schottky plots were created by plotting C^{-2} versus potential changes as shown in Figure 8-7. All samples exhibit positive slopes over a range of scanning potential and it indicates characteristics of n-type semiconductors with dominant defects of oxygen vacancies and/or metal cation interstitials [76]. By further increasing the potential, as already shown [70,74], the strength of the oxide film was weakened by hydrogen ionization which generated magnesium vacancies and led to a p-

type semiconducting behavior. This behavior is consistent with the polarization curves where increasing turns of HPT forms a more resistive oxide film against an overpotential.

The donor densities of the oxide films, MgO, formed on the samples in the 0.1 M NaCl solution were calculated through slopes of the linear portions of the Mott-Schottky plots and substituting in in derivate format of Eq (7) as shown in Figure 8-8. The donor densities of the HPT-processed samples with one, two and five turns increase compared with the extruded sample whereas the donor densities of the HPT-processed samples with 10 and 20 turns are slightly less than for the extruded sample. This behavior corroborates the EIS results, although the thickness of oxide film decreased with increasing numbers of turns, but the oxide becomes more integrated and less defective. It is noteworthy to mention that a quantitative estimation of the capacitance and charge carrier densities in the Mott-Schottky test may be affected by the localized electronic states [77], potential scan rate, the CPE behavior of electrode and neglecting Helmholtz layer [52]; therefore, the presented data were implemented to provide a more qualitative comparison by keeping all the test parameter constant and evaluating the effect of number of HPT turns.

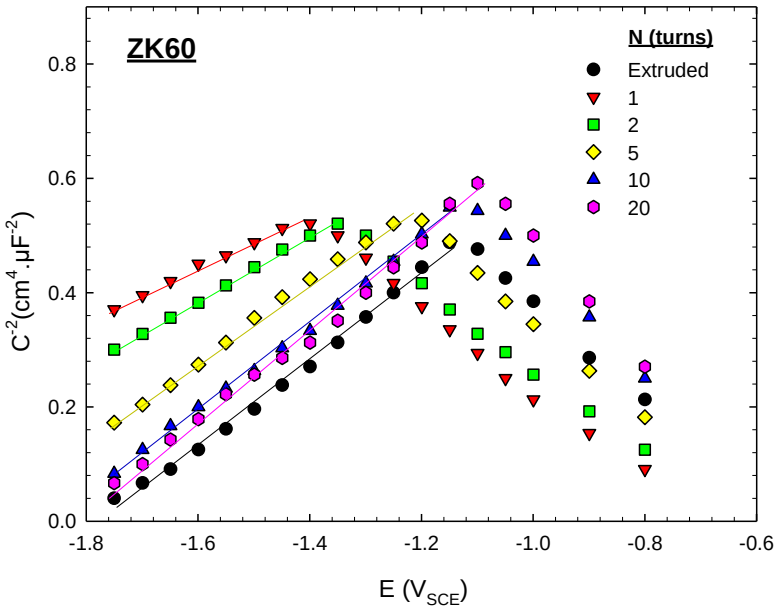

Figure 8-7. The Mott–Schottky plots for the ZK60 samples processed by extrusion and various numbers of turns by HPT, immersed in 0.1 M NaCl for 4 h.

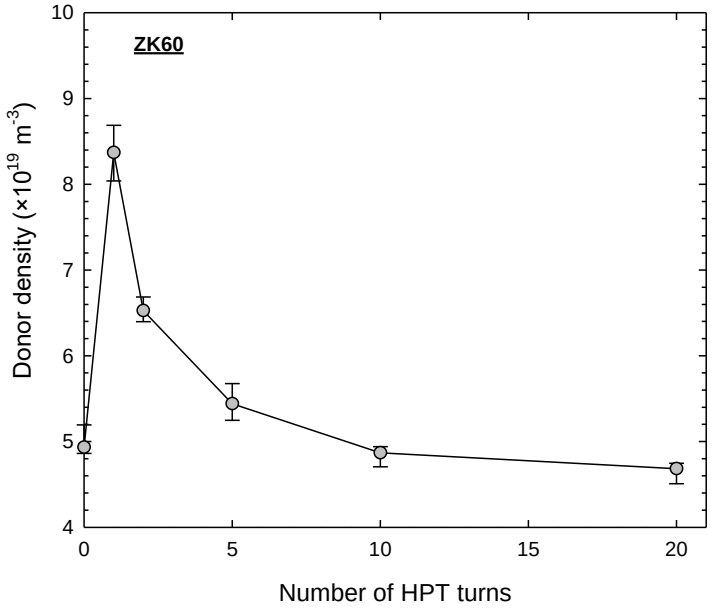

Figure 8-8. Donor density of the ZK60 Mg alloy processed by extrusion and various numbers of turns by HPT, immersed in 0.1 M NaCl for 4 h. In X axis, the 0 number of HPT turns represents the original extruded material with no HPT process.

Hydrogen Evolution Testing of HPT-Processed Materials

The results of the hydrogen evolution test are presented in Figure 8-9 for a 24 h immersion in the 0.1 M NaCl solution at room temperature. In general, hydrogen evolution from a corroding surface at its OCP implies an electrochemical activity of the surface [35,40]. The cumulative amount of the volume of hydrogen gas evolved from the surface of the samples varies significantly with the numbers of turns and the results demonstrate that HPT changes the activity of the ZK60 alloy. In all cases, the total evolved hydrogen increases within almost the first 4 h of exposure. This increment is significant for samples processed through one, two and five turns, with one representing the highest and five the lowest.

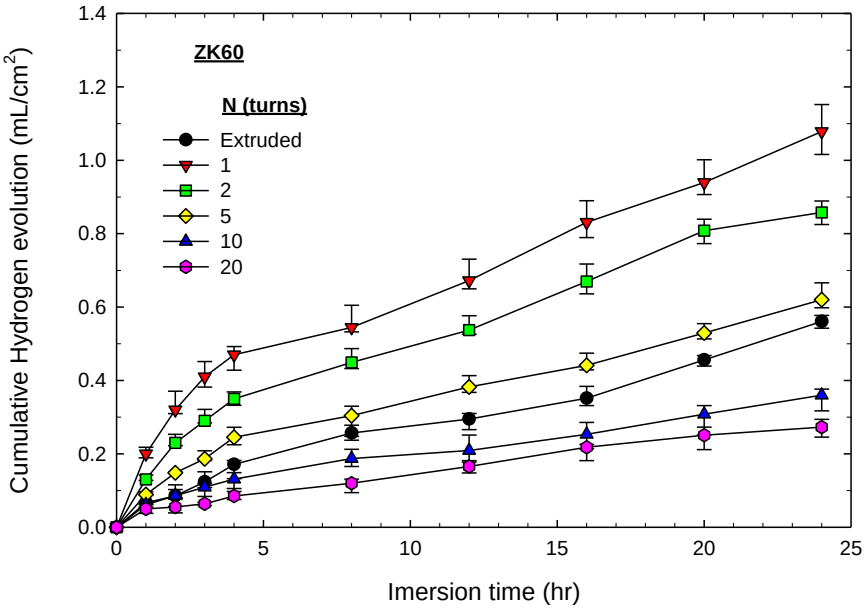

Figure 8-9. Cumulative hydrogen evolution for extruded and HPT proceeded samples immersed in 0.1 M NaCl solution for 24 h.

After around 4 h, the rate of hydrogen evolution decreases with a decrease in the slope of the lines, thereby indicating the formation of partially protective corrosion products on the surface which reduce active surface area and hinder the dissolution [52,54]. The hydrogen evolution on the samples processed through 10 and 20 turns is much lower compared to the other HPT-processed samples. After 24 h of immersion in the NaCl solution, the amount of hydrogen gas evolved on the surface of the HPT-processed sample after 20 turns was less than ~20% of that evolved on the HPT-processed surface for one turn, indicating a significant reduction in corrosion activity on that sample.

Post-Exposure Microstructural Observations

The corresponding images obtained at different times of immersion in 0.1 M NaCl solution are shown in Figure 8 10. The disks generally corroded steadily due to the existence of chloride ions in solution, but from the extruded sample to the sample processed with one turn there is a degradation of material even after only 4 h of exposure to the 0.1 M NaCl solution. The corrosion started generally from the periphery of the sample where there is maximum strain and consequently localized grain refinement as reported previously for this material by the co-authors of this study [27,30,41]. This trend can be observed in the higher magnification from a slice of disks in Figure 8-11. By increasing the numbers of turns, as demonstrated also in the results of the electrochemical

tests and the hydrogen evolution experiments, the corrosion is ameliorated. The surface of the HPT-processed sample with 20 turns was corroded more homogenously.

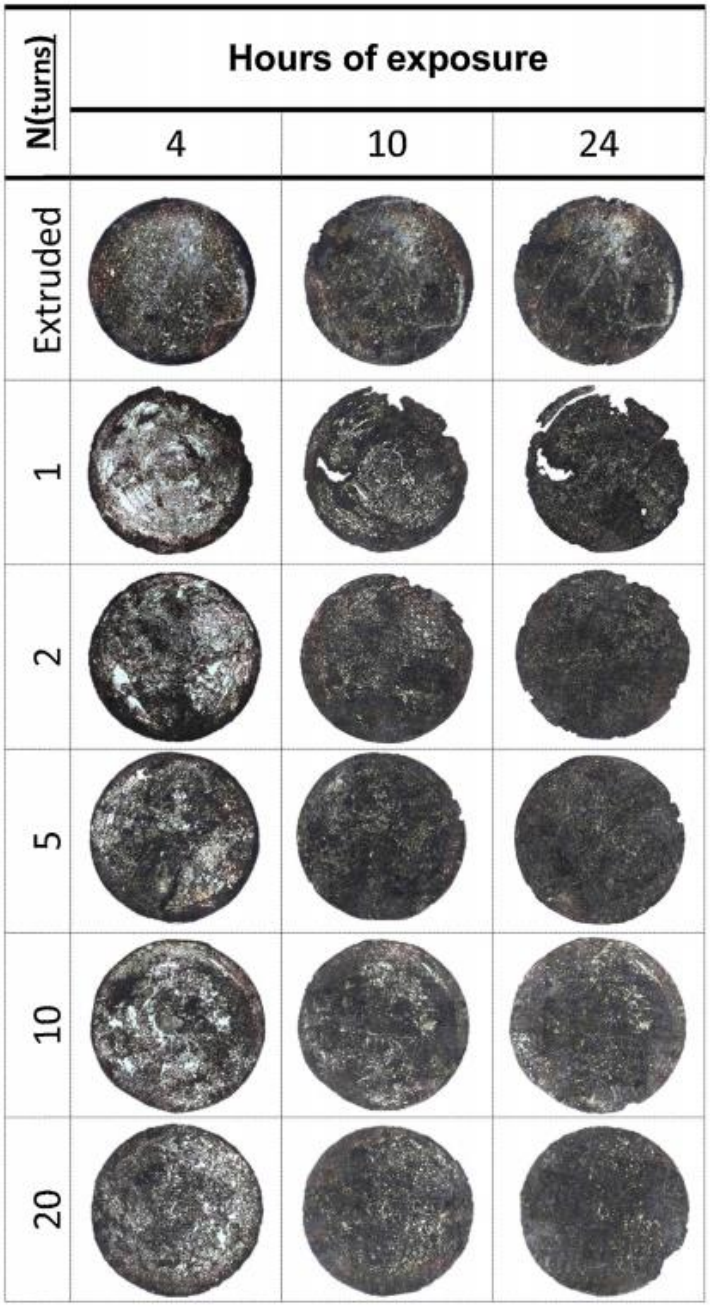

Figure 8-10. Cumulative The optical images of the corroded surfaces of the extruded as well as HPT proceeded ZK60 samples at different immersion time (the diameter of each disk is ~10 mm).

A drastic increase in corrosion activity of the samples within the first 4 h of immersion in solution and then a gradual increase after that time was also observed and this is also consistent with the results from the hydrogen evolution test. Nonetheless, by comparing images of the extruded disk with 4 h immersion in Figure 8-10 with different times of immersion for 10 and 24 h, it is concluded that the corrosion morphology and propagation path are not changed by the increasing time of immersion. By contrast, and for all HPT-processed samples, the morphology changes with time since more portions of the surface are covered by a corrosion product layer with darkish contract. This behavior is also apparent in Figure 8-9 since the extruded sample shows a relatively constant rate of hydrogen evolution.

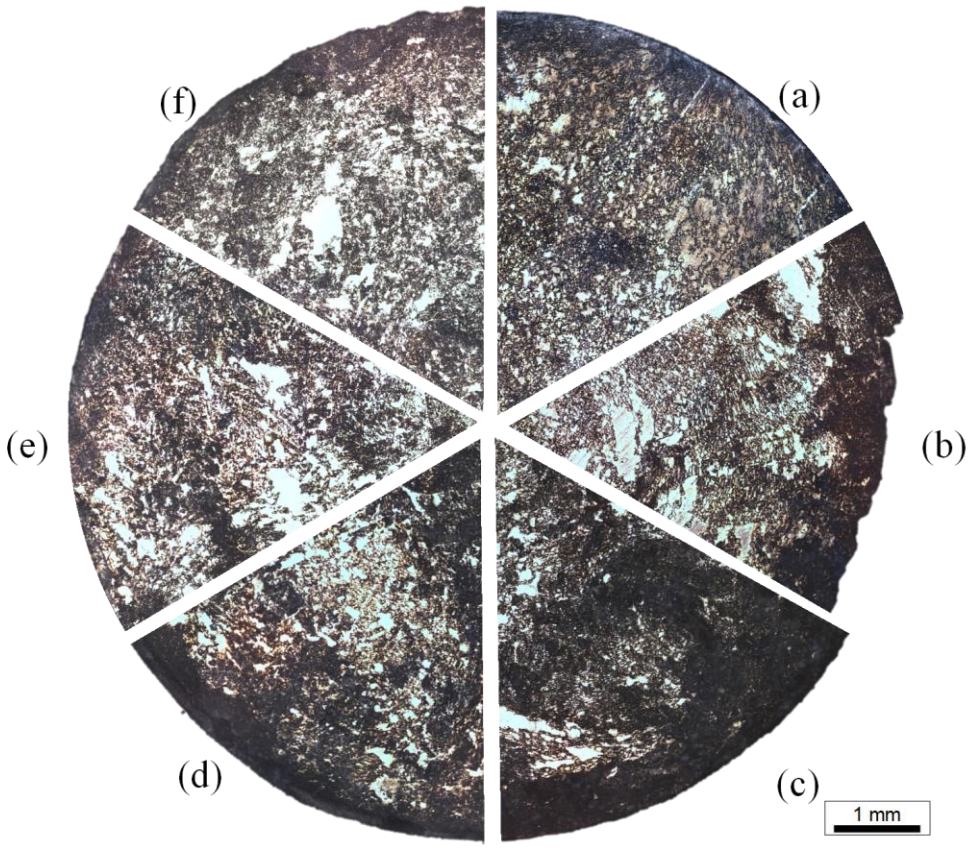

Figure 8-11. The micrographs from slice of the 4 h corroded surface of disks shown in Figure 10 for (a) extruded and processed by (b) 1, (c) 2, (d) 5, (e) 10 and (f) 20 turns of HPT.

Figure 8-12 gives the corresponding images obtained at the mid-radius of each sample shown in Figure 10 at a higher magnification after 4 h of immersion in the 0.1 M NaCl solution. Fundamental studies on the nature of the grain boundaries showed that, by comparison with the crystal interior, the grain boundaries have relatively wider distributions of interatomic spacing with reduced atomic density due to the misfit between adjacent crystals and therefore the grain boundaries are more active regions compare to within the grains [78-80]. Accordingly, it is expected that chloride ions initially selectively attack such active regions [13,81]. For the extruded sample with conventional grain size, it is reasonable to expect that the majority of corrosion pathways

are the grain boundaries, due to similarity and size of grains and boundaries between Figure 8-1 and Figure 8-12 for extruded samples. In the HPT-processed samples with 1, 2 and five turns, these paths expand but are not uniform due to incomplete grain refinement as shown in Figure 8-1 and were extensively discussed in a previous publication [27,29,41].

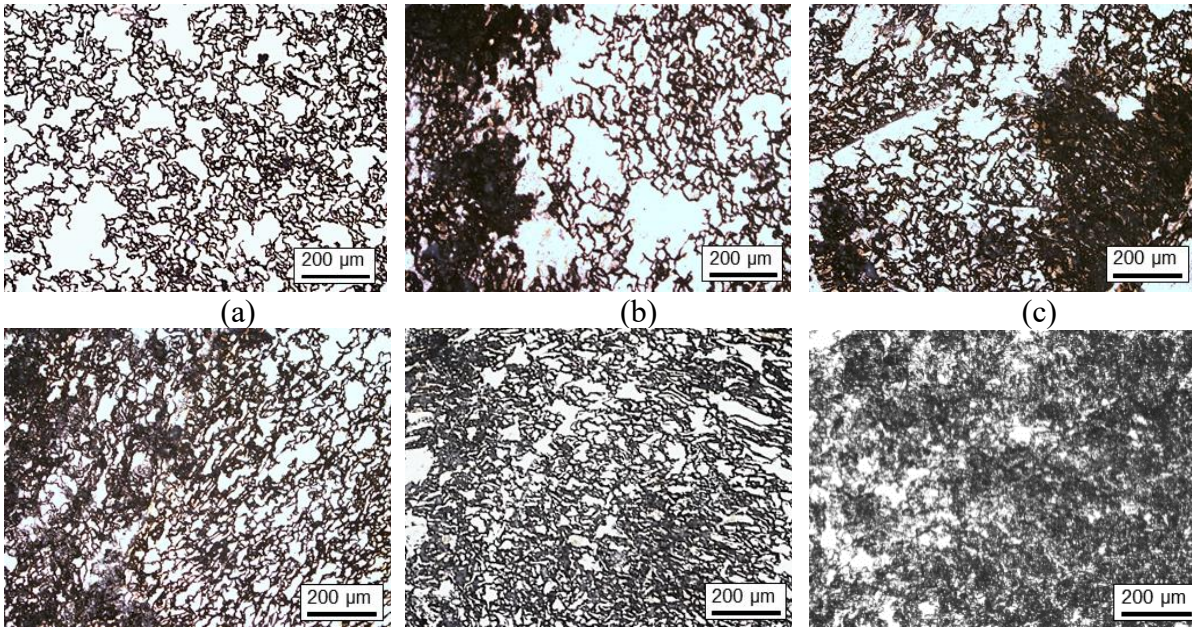

Figure 8-12. The micrographs of the corroded surfaces of ZK60 Mg alloy samples at exposed in 0.1 M NaCl for 4 h for (a) extruded and processed by (b) 1, (c) 2, (d) 5, (e) 10 and (f) 20 turns of HPT.

Consequently, a micro-galvanic corrosion between the interiors of the large grains and non-distorted areas as cathode with cluster of distorted grains with high boundary densities as anode can form [5,13]. Convection at the vicinity of this area, due to the copious hydrogen bubbling [43], can exacerbate corrosion. Therefore, at the early stages of HPT, partial grain refinement and the formation of an unintegrated and defective corrosion product film is barely beneficial and even accelerates the localized corrosion

compared to the extruded ZK60 alloy. However, by increasing the numbers of HPT turns, the corrosion performance of the samples is improved, and this can be attributed to the more uniform grain refinement and grain distribution in these samples compared to the other samples as shown in the electrochemical results and micrographs in Figure 8-10 and Figure 8-11. The uniform grain refinement in the HPT-processed samples with higher numbers of turns minimizes the occurrence of the micro-galvanic cells, enhances the stability of product film and ultimately leads to an improved corrosion behavior. Suffice to mention that, as Figure 8-11 shows and previously elaborated by authors [27], gradual grain refinement through HPT process is not homogenous along the radius of HPT disks for Mg alloys. Necklacelike configurations with small grains surrounds the larger grains [18], although this grain refinement evolution is not practically proportional with radius at all regions, but microstructure evolves and becomes gradually homogenous by increasing numbers of turns. In the test solution of this study, explained micro-galvanic current restrict to current flux between nearby anodes and cathodes, and galvanic effect between each point across whole area of diameter are not addressed.

The SEM micrographs in Figure 8-13 with the corresponding EDS results from marked points provided in Table 8-2 show the microscopic morphologies of the extruded and the HPT-processed ZK60 disks after 24 h immersion in the 0.1 M NaCl solution. The earlier observations in Figure 8-12 and deep concavity along this path at Figure 8-13 confirm that the dissolution mainly starts along this paths. The micrograph in Figure 8-13 (a) and corresponding EDS in Table 8-2 demonstrate no discernible thick precipitate

within the grain. However, Figure 8-13 (b) and the corresponding EDS data in Table 8-2 show that localized corrosion and precipitate was detected mostly in the vicinity of fine grains with the presence of more Cl, presumably as $MgCl_2$ [4], and this corroborates the catalytic effect of these corrosion precipitates product in the form of pitting of this region [43]. By increasing the numbers of HPT turns those corrosion path and morphology observed for extruded and early stages of HPT processed samples, seems to be disappeared. In addition, as the composition analysis at point C implies, those corrosion product precipitates layer has relatively more oxide and less Cl^- ion and consequently less defective sites than for the one turn HPT sample. It is noteworthy that in the early stages of HPT isolated precipitates in the refined grain zones are fragmented due to the internal stresses of vigorous dissolution and corrosion precipitates accumulation. Thus, during immersion a localized corrosion accelerated by these precipitate peeling-off and the consequent penetration of an active aggressive Cl^- ion. By increasing the numbers of turns, the covered surfaces become more integrated and refined and cracks disappear due to the homogenous formation of less defective corrosion products on uniformed grain refined substrate. The increasing R_f values is additional evidence of the higher protective properties of the oxide film after larger numbers of turns of HPT. It should be noted that in this study a 0.1 M Cl^- , with relatively high ohmic resistance, was used as the aggressive ion whereas earlier research involved more corrosive environments such as 0.62 M $[Cl]^-$ (3.5 wt.% NaCl) which may persistently attack the surface and break down and change the chemistry corrosion product [9,10,13,43]. On the other hand, using passivating rather than corrosive solutions such as a simulated body fluid leads to an

improvement in the protective oxide layer and corrosion behavior in each turn of the HPT process compared both to earlier turns and to the original extruded condition [22,23,82].

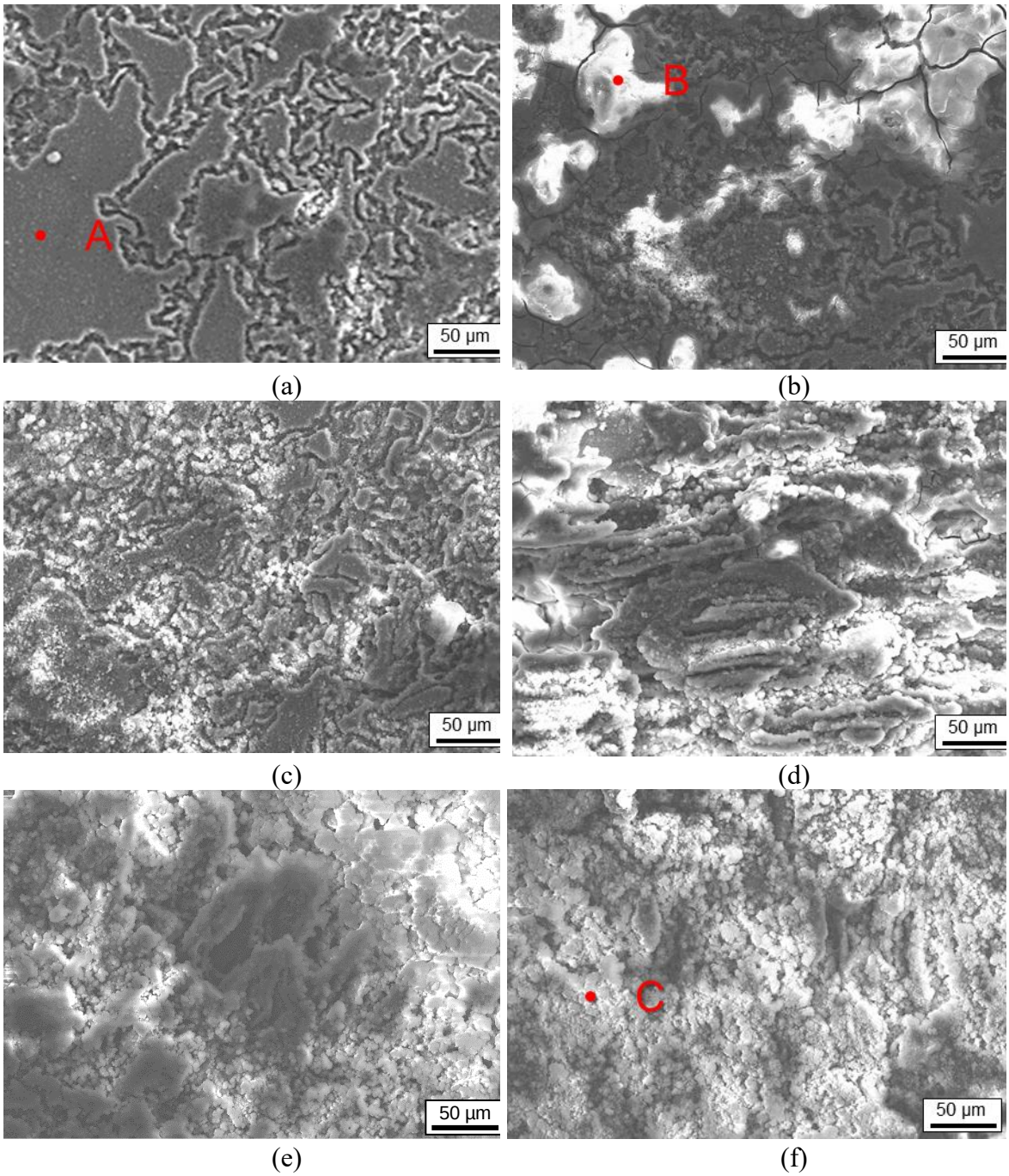

Figure 8-13. SEM of surface morphologies of the ZK60 disks after 24 h immersion in 0.1 M NaCl solution for samples of (a) extruded with point A for EDS analysis and processed by (b) one turn of HPT with point B for EDS analysis, (c) two turns of HPT with point, (d) five turns of HPT, (e) 10 turns of HPT and (f) 20 turns of HPT with point C for EDS analysis. The corresponding EDS results of point A, B and C are compared in Table 8-2.

Table 8-2. EDS results of corresponding areas in Figure 8-13

Element (wt.%)	A	B	C
Mg	81.1	28.1	58.2
Zn	3.2	2.3	1.0
O	14.5	57.7	39.1
Cl	0.2	11.3	0.9

Discussion

The poor corrosion resistance of Mg and its alloys mainly originates from two factors: first, the comparatively high electronegative potential of Mg which enables corrosion activity even without presence of oxygen. The second factor suggests that oxide/hydroxide layers that form on the surface of Mg are soluble in most aqueous environments and provide insufficient protective properties [1] and potentially accelerates corrosion [39,43,83]. The grain boundaries, inclusions and the defects are more active regions compared to the other grains and generally it is expected that the chloride ions will selectively attack these active regions first and accelerates dissolution [38-40,81].

The HPT processing imposes a torsional strain which varies across the disk radius. The equivalent von Mises strain describes the stain variation by number of turns of HPT, N.

$$\varepsilon_{eq} = \frac{2\pi N r}{h\sqrt{3}} \tag{8}$$

where r is the radius and h is the thickness of the disk. Following Eq. 8 implies that ε_{eq}

varies from zero at the center of the disk to a maximum at the edge [84,85]. It may be hypothesized that the significant increase in corrosion activity in the early stages of HPT processing originates from the variation of the imposed strain across each circular disk from zero at the center to a maximum at the periphery since this variation leads to an inhomogeneity in the refined grains [18,86]. Furthermore, this inhomogeneity in return causes the formation of isolated and broken surface precipitates on the HPT-processed samples which accelerate localized corrosion.

Partial grain refinement and non-protective corrosion product accumulation cannot be beneficial in enhancing the corrosion resistance of the extruded ZK60 alloy in the 0.1 M NaCl solution. However, by increasing the numbers of turns the corrosion properties of the samples are improved. This is attributed to the evolution of the microstructure into the more uniform grain refinement and distribution with fewer turns of HPT as shown in Figure 8-1. The uniformity of mechanical properties and texture as a result of the uniformity of microstructure of ZK60 with saturation in grain refinement at high numbers of turns of HPT was studied extensively in earlier investigations of the authors [27,41]. As described earlier, higher numbers of N results in saturation of grain refinement, refined grains distributed homogenously on entire of the surfaces and consequently it minimizes the occurrence of micro-galvanic cells and ultimately leads to an improved corrosion resistance on these samples. Furthermore, the appearance of a pseudo-passive potential in the potentiodynamic polarization corroborates this assumption. It was suggeted that increasing the numbers of turns increases the integrity

and protectivity of the surface film. Moreover, the inductive loop in the Nyquist spectra appears when the corrosion products are fragmented [21,87-89], and the dissolved Mg generates intermediate species which remain adsorbed but unstable on the surface. The shrinking inductive loop and appearance of a diffusion impedance through corrosion product in the Nyquist spectra also confirms this proposal [55,58,60]. In addition, as illustrated in the Mott-Schottky test in Figure 8-8 and the EDS results in Table 8-2, a preferable protective film with fewer defects was achieved in the oxide film by further homogenizing and refining the microstructure.

In the microscopic corrosion morphologies in Figure 8-13, islands of cracked corrosion products are gradually replaced with uniform compact oxide films with increasing numbers of HPT turns. Plastic deformation creates many lattice defects, interstitials and vacancies [21], and in addition more grain boundaries with lower atomic densities are produced compared to within the grains [75,76]. Recent studies show nano-sized second phase precipitation from the highly supersaturated Mg matrix [5,83,86] may form during the HPT process. These distributed defects, refined grains and precipitates potentially react with the solution and become oxidized more rapidly throughout the whole area of the disk simultaneously [9]. Thus, HPT samples with higher turns exhibit uniform corrosion because of the uniform distribution of grains, second phases and oxide film and as a result there is less occurrence of micro-galvanic cells.

Processing route is also another key factor affecting on corrosion response in addition to grain size and grain size distribution dependency [5]. The textural analysis with pole figures from the surfaces of the disks prepared for corrosion tests demonstrated an evolution of grain orientation at the surface of the disks from extruded materials with prismatic planes parallel to the surfaces to a final basal {0001} fiber texture with the c-axis parallel to the ND after processing by five turns of HPT. In Mg alloys, the basal planes have a slower oxidation rate compared to the prismatic planes due to their higher densities and order of atoms [44,91-93].

It should be noted that it is not possible to isolate the effect of texture and grain size on the overall corrosion behavior of the HPT-processed samples. Nevertheless, at high numbers of HPT turns with more uniformity, it is reasonable to assume that this change in crystal structure and orientation of the samples also plays a significant role in the observed results with the corrosion behavior of the samples improved after five turns.

Summary and Conclusions

The microstructural evolution and its influence on the electrochemical behavior of extruded and HPT-processed ZK60 alloy were investigated in this study. In the early stages of HPT, applying straining leads to an inhomogeneous grain refinement and decreases the corrosion resistance of this alloy. Applying more rotations improves the uniformity of the grains and the grain size distribution. The uniform and finely distributed grains can effectively decrease the corrosion activity through rapid formation of a smooth

oxide film at the grain boundaries and surface crystalline defects. Otherwise, grain refinement may cause inhomogeneities which will accelerate the dissolution process. In addition, an anisotropic texture was developed by increasing the numbers of turns and this could potentially improve the oxidation resistance of the disks. It should be emphasized that all experiments were conducted in a 0.1 M NaCl solution and, due to the nature of the Mg alloy oxide films, the results may vary in other environments.

References

[1] K. Gusieva, C.H.J. Davies, J.R. Scully, N. Birbilis, Corrosion of magnesium alloys: the role of alloying, Int. Mater. Rev. 60 (2015) 169–194.

[2] A. Atrens, S. Johnston, Z. Shi, M.S. Dargusch, Scripta Materialia Viewpoint - Understanding Mg corrosion in the body for biodegradable medical implants Sputter deposited alloys Ultra-high purity Mg, Scr. Mater. 154 (2018) 92–100.

[3] B.A. Atrens, G. Song, M. Liu, Z. Shi, F. Cao, M.S. Dargusch, Review of Recent Developments in the Field of Magnesium Corrosion, (2015).

[4] J. Chen, L. Tan, K. Yang, Effect of heat treatment on mechanical and biodegradable properties of an extruded ZK60 alloy, Bioact. Mater. 2 (2017) 19–26.

[5] D. Orlov, K.D. Ralston, N. Birbilis, Y. Estrin, Enhanced corrosion resistance of Mg alloy ZK60 after processing by integrated extrusion and equal channel angular pressing, Acta Mater. 59 (2011) 6176–6186.

[6] D. Song, A. Ma, J. Jiang, P. Lin, D. Yang, J. Fan, Corrosion behavior of equal-channel-angular-pressed pure magnesium in NaCl aqueous solution, Corros. Sci. 52 (2010) 481–490.

[7] D. Song, A.B. Ma, J.H. Jiang, P.H. Lin, D.H. Yang, J.F. Fan, Corrosion behaviour of bulk ultra-fine grained AZ91D magnesium alloy fabricated by equal-channel angular pressing, Corros. Sci. 53 (2011) 362–373.

[8] R. Xin, Y. Luo, A. Zuo, J. Gao, Q. Liu, Texture effect on corrosion behavior of AZ31 Mg alloy in simulated physiological environment, Mater. Lett. 72 (2012) 1–4.

[9] C.L.P. Silva, A.C. Oliveira, C.G.F. Costa, R.B. Figueiredo, M. deF. Leite, M.M. Pereira, V.F.C. Lins, T.G. Langdon, Effect of severe plastic deformation on the biocompatibility and corrosion rate of pure magnesium, J. Mater. Sci. 52 (2017) 5992–6003.

[10] D. Ahmadkhaniha, Y. Huang, M. Jaskari, A. Järvenpää, M.H. Sohi, C. Zanella, L.P. Karjalainen, T.G. Langdon, Effect of high-pressure torsion on microstructure, mechanical properties and corrosion resistance of cast pure Mg, J. Mater. Sci. 53 (2018) 16585–16597.

[11] C. By, N. Birbilis, Y. Estrin, Corrosion of Pure Mg as a Function of Grain Size and Processing Route, Adv. Eng. Mater. 10 (2008) 579–582.

[12] D. Song, C. Li, N. Liang, F. Yang, J. Jiang, J. Sun, G. Wu, A. Ma, X. Ma, Simultaneously improving corrosion resistance and mechanical properties of a magnesium alloy via equal-channel angular pressing and post water annealing, Mater. Des. 166 (2019) 107621.

[13] K.D. Ralston, N. Birbilis, C.H.J. Davies, Revealing the relationship between grain size and corrosion rate of metals, Scr. Mater. 63 (2010) 1201–1204.

[14] S. Gollapudi, Grain size distribution effects on the corrosion behaviour of materials, Corros. Sci. 62 (2012) 90–94.

[15] M. Hoseini, A. Shahryari, S. Omanovic, J.A. Szpunar, Comparative effect of grain size and texture on the corrosion behaviour of commercially pure titanium processed by equal channel angular pressing, Corros. Sci. 51 (2009) 3064–3067.

[16] H.S. Kim, W.J. Kim, Enhanced corrosion resistance of ultrafine-grained AZ61 alloy

containing very fine particles of $Mg_{17}Al_{12}$ phase, Corros. Sci. 75 (2013) 228–238.

[17] Y. Huang, R.B. Figueiredo, T. Baudin, F. Brisset, T.G. Langdon, Evolution of strength and homogeneity in a magnesium AZ31 alloy processed by high-pressure torsion at different temperatures, Adv. Eng. Mater. 14 (2012) 1018-1026.

[18] R.B. Figueiredo, T.G. Langdon, Processing Magnesium and Its Alloys by High-Pressure Torsion : An Overview, 1801039 (2018) 1–15.

[19] J. Jayaraj, S. Amruth Raj, A. Srinivasan, S. Ananthakumar, U.T.S. Pillai, N.G.K. Dhaipule, U.K. Mudali, Composite magnesium phosphate coatings for improved corrosion resistance of magnesium AZ31 alloy, Corros. Sci. 113 (2016) 104–115.

[20] S. Pawar, T.J.A. Slater, T.L. Burnett, X. Zhou, G.M. Scamans, Z. Fan, G.E. Thompson, P.J. Withers, Crystallographic effects on the corrosion of twin roll cast AZ31 Mg alloy sheet, Acta Mater. 133 (2017) 90–99.

[21] Q. Liu, Q.X, Ma, G.Q. Chen, X. Cao, S. Zhang, J.L. Pan, G. Zhang, Q.Y. Shi, Enhanced corrosion resistance of AZ91 magnesium alloy through refinement and homogenization of surface microstructure by friction stir processing, Corros. Sci. 138 (2018) 284–296.

[22] J.H. Gao, S.K. Guan, Z.W. Ren, Y.F. Sun, S.J. Zhu, B. Wang, Homogeneous corrosion of high pressure torsion treated Mg–Zn–Ca alloy in simulated body fluid, Mater. Lett. 65 (2011) 691-693.

[23] C.Z. Zhang, S.J. Zhu, L.G. Wang, R.M. Guo, G.C. Yue, S.K. Guan, Microstructures and degradation mechanism in simulated body fluid of biomedical Mg-Zn-Ca alloy processed by high pressure torsion, Mater. Des. 96 (2016) 54–62.

[24] B.C. Zhang, S. Guan, L. Wang, S. Zhu, J. Wang, R. Guo, Effect of Solution Pretreatment on Homogeneity and Corrosion Resistance of Biomedical Mg – Zn – Ca Alloy Processed by High Pressure Torsion, Adv. Eng. Mater. (2016) 1–11.

[25] X. Wang, M. Nie, C.T. Wang, S.C. Wang, N. Gao, Microhardness and corrosion properties of hypoeutectic Al-7Si alloy processed by high-pressure torsion, Mater. Des. 83 (2015) 193–202.

[26] K. Bryła, J. Morgiel, M. Faryna, K. Edalati, Z. Horita, Effect of high-pressure torsion on grain refinement, strength enhancement and uniform ductility of EZ magnesium alloy, Mater. Lett. 212 (2018) 323–326.

[27] S.A. Torbati-Sarraf, T.G. Langdon, Properties of a ZK60 magnesium alloy processed by high-pressure torsion, J. Alloy. Compd. 613. (2014) 357-363.

[28] S.A. Torbati-Sarraf, R. Alizadeh, R. Mahmudi, T.G. Langdon, Evaluating the flow properties of a magnesium ZK60 alloy processed by high-pressure torsion: A comparison of two different miniature testing techniques, Mater. Sci. Eng. A 708 (2017) 432–439.

[29] S. Sabbaghianrad, S.A. Torbati-Sarraf, T.G. Langdon, An investigation of the limits of grain refinement after processing by a combination of severe plastic deformation techniques: A comparison of Al and Mg alloys, Mater. Sci. Eng. A 712 (2018) 373–379.

[30] S.A. Torbati-Sarraf, S. Sabbaghianrad, T.G. Langdon, Microstructural properties, thermal stability and superplasticity of a ZK60 Mg alloy processed by high-pressure torsion, Lett. Mater. 5 (2015) 287–293.

[31] S.A. Torbati-Sarraf, S. Sabbaghianrad, T.G. Langdon, Using post-deformation annealing to optimize the properties of a ZK60 magnesium alloy processed by high-

pressure torsion, Adv. Eng. Mater. 20 (2017) 1-10.

[32] R.B. Figueiredo, P.R. Cetlin, T.G. Langdon TG, Using finite element modeling to examine the flow processes in quasi-constrained high-pressure torsion. Mater. Sci. Eng. A 528 (2011) 8198-8204.

[33] S.A. Torbati-Sarraf, S. Sabbaghianrad, R.B. Figueiredo, T.G. Langdon, Orientation imaging microscopy and microhardness in a ZK60 magnesium alloy processed by high-pressure torsion, J. Alloys Compd. 712 (2017) 185–193.

[34] C.L.P Silva, I.C. Tristão, S. Sabbaghianrad, S.A Torbati-Sarraf, R.B Figueiredo, T.G. Langdon, Microstructure and hardness evolution in magnesium processed by HPT, Mater. Res. 20 (2017) 2-7.

[35] D.S.J. G.L. Song, A. Atrens, An Hydrogen Evolution Method for the Estimation of the Corrosion Rate of Magnesium Alloys, Magnes. Technol. (2001) 565–572.

[36] S. Fajardo, G.S. Frankel, Gravimetric method for hydrogen evolution measurements on dissolving magnesium, J. Electrochem. Soc. 162 (2015) C693–C701.

[37] M. Esmaily, J.E. Svensson, S. Fajardo, N. Birbilis, G.S. Frankel, S. Virtanen, R. Arrabal, S. Thomas, L.G. Johansson, Fundamentals and advances in magnesium alloy corrosion, Prog. Mater. Sci. 89 (2017) 92–193.

[38] M. Liu, P. Schmutz, P.J. Uggowitzer, G. Song, A. Atrens, The influence of yttrium (Y) on the corrosion of Mg – Y binary alloys, Corros. Sci. 52 (2010) 3687–3701.

[39] G. Song, A. Atrens, Understanding magnesium corrosion. A framework for improved alloy performance, Adv. Eng. Mater. 5 (2003) 837–858.

[40] X. Mn, F. Cao, Z. Shi, G. Song, M. Liu, A. Atrens, B. Sem, Corrosion behaviour in

salt spray and in 3 . 5 % NaCl solution saturated with Mg $(OH)_2$ of as-cast and solution heat-treated binary Mg – X alloys : X = Mn, Sn, Ca, Zn, Al, Zr, Si, Sr , Corros. Sci. 76 (2013) 60–97.

[41] H.J. Lee, S.K. Lee, K.H. Jung, G.A. Lee, B. Ahn, M. Kawasaki, T.G. Langdon, Evolution in hardness and texture of a ZK60A magnesium alloy processed by high-pressure torsion, Mater. Sci. Eng. A 630 (2015) 90–98.

[42] Y. Huang, R.B. Figueiredo, T. Baudin, A.L. Helbert, F. Brisset, T.G. Langdon, Effect of temperature on the processing of a magnesium alloy by high-pressure torsion, J. Mater. Sci. 47 (2012) 7796–7806.

[43] S. Fajardo, C.F. Glover, G. Williams, G.S. Frankel, The Source of Anodic Hydrogen Evolution on Ultra High Purity Magnesium, Electrochim. Acta. 212 (2016) 510–521.

[44] K. Hagihara, M. Okubo, M. Yamasaki, T. Nakano, Crystal-orientation-dependent corrosion behaviour of single crystals of a pure Mg and Mg-Al and Mg-Cu solid solutions, Corros. Sci. 109 (2016) 68–85.

[45] Y. Song, E.H. Han, D. Shan, C.D. Yim, B.S. You, The effect of Zn concentration on the corrosion behavior of Mg-xZn alloys, Corros. Sci. 65 (2012) 322–330.

[46] G.L. Song, A. Atrens, Corrosion mechanisms of magnesium alloys, Adv. Eng. Mater. 1 (1999) 11–33.

[47] Z. Shi, M. Liu, A. Atrens, Measurement of the corrosion rate of magnesium alloys using Tafel extrapolation, Corros. Sci. 52 (2010) 579–588.

[48] G.S. Frankel, A. Samaniego, N. Birbilis, Evolution of hydrogen at dissolving magnesium surfaces, Corros. Sci. 70 (2013) 104–111.

[49] M. Curioni, F. Scenini, T. Monetta, F. Bellucci, Correlation between electrochemical impedance measurements and corrosion rate of magnesium investigated by real-time hydrogen measurement and optical imaging, Electrochim. Acta 166 (2015) 372–384.

[50] G. Song, A. Atrens, D. Stjohn, J. Nairn, Y. Li, The electrochemical corrosion of pure magnesium in 1 N NaCl, Corros. Sci. 39 (1997) 855–875.

[51] G. Song, A. Atrens, D.S. John, X. Wu, J. Nairn, The anodic dissolution of magnesium in chloride and sulphate solutions, Corros. Sci. 39 (1997) 1981–2004.

[52] N. Causse, S. Leleu, B. Rives, On the stability of the oxides film formed on a magnesium alloy containing rare-earth elements, Electrochim. Acta. 290 (2018) 586–594.

[53] A.D. King, N. Birbilis, J.R. Scully, Accurate Electrochemical Measurement of Magnesium Corrosion Rates ; a Combined Impedance , Mass-Loss and Hydrogen Collection Study, Electrochim. Acta. 121 (2014) 394–406.

[54] G. Baril, G. Galicia, C. Deslouis, N. Pébère, B. Tribollet, V. Vivier, An impedance investigation of the mechanism of pure magnesium corrosion in sodium sulfate solutions, J. Electrochem. Soc. 154 (2007) C108-C113.

[55] G. Baril, N. Pébère, The corrosion of pure magnesium in aerated and deaerated sodium sulphate solutions, Corros. Sci. 43 (2001) 471–484.

[56] J. Chen, J. Wang, E. Han, J. Dong, W. Ke, AC impedance spectroscopy study of the corrosion behavior of an AZ91 magnesium alloy in 0.1 M sodium sulfate solution, Electrochim. Acta. 52 (2007) 3299–3309.

[57] W. Davidson, J. Kleinberg, R.L. Petty, W. Davidson, The Anodic Oxidation of Magnesium Metal : Evidence for the Existence of Unipositive, J. Am. Chem. Soc. 2

(1954) 368.

[58] G. Galicia, N. Pébère, B. Tribollet, V. Vivier, Local and global electrochemical impedances applied to the corrosion behaviour of an AZ91 magnesium alloy, Corros. Sci. 51 (2009) 1789–1794.

[59] G.G. Perrault, The potential-pH diagram of the magnesium-water system, J. Electroanal. Chem. Interfacial Electrochem. 51 (1974) 107–119.

[60] G. Baril, C. Blanc, N. Pébère, AC Impedance Spectroscopy in Characterizing Time-Dependent Corrosion of AZ91 and AM50 Magnesium Alloys Characterization with Respect to Their Microstructures, J. Electrochem. Soc. 148 (2001) B489.

[61] B. Tribollet, G. Galicia, N. Pebere, V. Vivier, Corrosion Study of an AZ91 Magnesium alloy by EIS and LEIS, ECS Trans., ECS, 2006: pp. 157–168.

[62] G.J. Brug, A.L.G. van den Eeden, M. Sluyters-Rehbach, J.H. Sluyters, The analysis of electrode impedances complicated by the presence of a constant phase element, J. Electroanal. Chem. Interfacial Electrochem. 176 (1984) 275–295.

[63] M. Musiani, M.E. Orazem, N. Pébère, B. Tribollet, V. Vivier, Constant-Phase-Element Behavior Caused by Coupled Resistivity and Permittivity Distributions in Films, J. Electrochem. Soc. 158 (2011) C424.

[64] J.B. Jorcin, M.E. Orazem, N. Pébère, B. Tribollet, CPE analysis by local electrochemical impedance spectroscopy, Electrochim. Acta. 51 (2006) 1473–1479.

[65] C.H. Hsu, F. Mansfeld, Technical Note: Concerning the Conversion of the Constant Phase Element Parameter Y_0 into a Capacitance, Corrosion. 57 (2001) 747–748.

[66] M. Benoit, C. Bataillon, B. Gwinner, F. Miserque, M.E. Orazem, C.M. Sánchez-

sánchez, B. Tribollet, V. Vivier, Comparison of different methods for measuring the passive film thickness on metals, Electrochim. Acta. 201 (2016) 340–347.

[67] S. Chakri, I. Frateur, M.E. Orazem, E.M.M. Sutter, T.T.M. Tran, B. Tribollet, V. Vivier, Improved EIS Analysis of the Electrochemical behavior of carbon Steel in Alkaline solution, Electrochim. Acta. 246 (2017) 924–930.

[68] A. Son, N. Causse, M. Musiani, M.E. Orazem, N. Pébère, B. Tribollet, V. Vivier, Determination of water uptake in organic coatings deposited on 2024 aluminum alloy : Comparison between impedance measurements and gravimetry, Prog. Org. Coatings. 112 (2017) 93–100.

[69] A.K. Jonscher, Dielectric characterization of semiconductors, Solid. State. Electron. 33 (1990) 737–742.

[70] T. Zhang, Y. Shao, G. Meng, Y. Li, F. Wang, Effects of hydrogen on the corrosion of pure magnesium, 52 (2006) 1323–1328.

[71] D.D. Macdonald, The history of the point defect model for the passive state: a brief review of film growth aspects, Electrochim. Acta 56 (2011) 1761-1772.

[72] K. Darowicki, S. Krakowiak, P. Slepski, Selection of measurement frequency in Mott – Schottky analysis of passive layer on nickel, Electrochim. Acta. 51 (2006) 2204–2208.

[73] X. Liu, T. Zhang, Y. Shao, G. Meng, F. Wang, Effect of alternating voltage treatment on the corrosion resistance of pure magnesium, Corros. Sci. 51 (2009) 1772-1779.

[74] J. Chen, J. Wang, E. Han, J. Dong, W. Ke, States and transport of hydrogen in the corrosion process of an AZ91 magnesium alloy in aqueous solution, Corros. Sci. 50

(2008) 1292–1305.

[75] M.C.L. de Oliveira, V.S.M. Pereira, O.V. Correa, N.B. de Lima, R.A. Antunes, Correlation between the corrosion resistance and the semiconducting properties of the oxide film formed on AZ91D alloy after solution treatment, Corros. Sci. 69 (2013) 311-321.

[76] D.D. Macdonald, The point defect model for the passive state, J. Electrochem. Soc. 139 (1992) 3434-3449.

[77] M.H. Dean, U. Stimming, The electronic properties of disordered passive films, Corros. Sci. 29 (1989) 199–211.

[78] K.L. Merkle, D.J. Smith, Atomic structure of symmetric tilt grain boundaries in NiO, Phys. Rev. Lett. 59 (1987) 2887–2890.

[79] M. Wagner, Structure and thermodynamic properties of nanocrystalline metals, Am. Phys. Soc. 45 (1992) 635–640.

[80] V. Afshari, C. Dehghanian, Effects of grain size on the electrochemical corrosion behaviour of electrodeposited nanocrystalline Fe coatings in alkaline solution, Corros. Sci. 51 (2009) 1844–1849.

[81] Y.L. Cheng, T.W. Qin, H.M. Wang, Z. Zhang, Comparison of corrosion behaviors of AZ31, AZ91, AM60 and ZK60 magnesium alloys, Trans. Nonferrous Met. Soc. China (English ed.) 19 (2009) 517–524.

[82] C.L.P. Silva, R.B. Soares, P.R. Pereira, R.B. Figueiredo, V.F.C. Lins, T.G. Landgon, The effect of high-pressure torsion on microstructure, hardness and corrosion behavior for pure magnesium and different magnesium alloys, Adv. Eng. Mater.

[83] W. Liu, F. Cao, Y. Xia, L. Chang, J. Zhang, Localized Corrosion of Magnesium Alloys in NaCl Solutions Explored by Scanning Electrochemical Microscopy in Feedback Mode, Electrochim. Acta. 132 (2014) 377–388.

[84] E. Nationale, P. De Grenoble, Structure and deformation behavior of Armco iron subjected to severe plastic deformation, Acta Mater. 44 (1996) 4705–4712.

[85] F. Wetscher, A. Vorhauer, R. Stock, R. Pippan, Structural refinement of low alloyed steels during severe plastic deformation, Mater. Sci. Eng. A. 389 (2004) 809–816.

[86] K. Edalati, D. Akama, A. Nishio, S. Lee, Y. Yonenaga, J.M. Cubero-Sesin, Z. Horita, Influence of dislocation-solute atom interactions and stacking fault energy on grain size of single-phase alloys after severe plastic deformation using high-pressure torsion, Acta Mater. 69 (2014) 68–77.

[87] G. Song, Z. Xu, Crystal orientation and electrochemical corrosion of polycrystalline Mg, Corros. Sci. 63 (2012) 100–112.

[88] Y. Song, D. Shan, R. Chen, F. Zhang, E. Han, Biodegradable behaviors of AZ31 magnesium alloy in simulated body fluid, Mater. Sci. Eng. C 29 (2009) 1039–1045.

[89] J. Li, Q. Jiang, H. Sun, Y. Li, Effect of heat treatment on corrosion behavior of AZ63 magnesium alloy in 3.5 wt.% sodium chloride solution, Corros. Sci. 111 (2016) 288–301.

[90] B.B. Straumal, V. Pontikis, A.R. Kilmametov, A.A. Mazilkin, S.V. Dobatkin, B. Baretzky, Competition between precipitation and dissolution in Cu–Ag alloys under high pressure torsion, Acta Mater. 122 (2017) 60–71.

[91] L.G. Bland, K. Gusieva, J.R. Scully, Effect of crystallographic orientation on the corrosion of magnesium: comparison of film forming and bare crystal facets using

electrochemical impedance and raman spectroscopy, Electrochim. Acta 227 (2017) 136–151.

[92] X. Li, B. Jiang, J. He, J. Zhang, Z. Jiang, B. Liu, F. Pan, Improvement of planar isotropy, mechanical properties and corrosion resistance of extruded Mg-3Al-1Zn alloy sheet by special grain re-orientation, J. Alloys Compd. 72 (2017) 106–117.

[93] M. Liu, D. Qiu, M. Zhao, A. Atrens, The effect of crystallographic orientation on the active corrosion of pure magnesium, Scr. Mater. 58 (2008) 421–424.

CHAPTER 9

A comparative study of corrosion behavior of the AA6061-T6 bars, manufactured by the conventional extrusion and selective laser melting additive manufacturing in 0.5 M NaCl solution

Introduction

6XXX Al alloys has become widespread in transportation, semi-conductive and infrastructure due to reproducibility in production, heat treatability to gain high strength, formability and good corrosion performance [1–3]. Recent developments in additive manufacturing (AM) of metal part, including selective laser melting (SLM) which also termed powder bed fusion, have gained considerable attraction due to the ability to produce complex and near-net shaped components [4,5]. Improvement in design and performance and cost reduction, leads switching many industries, including Al alloys consumers to this technology. But reports on Al alloys parts manufactured by AM, with principally based on the compositions of wrought alloys, may lead to undesirable microstructures, reducing fatigue life and resulting in poor fracture toughness and mechanical properties [6–8]. This is attributed to light and poor flowability Al alloys powder along with relatively higher thermal conductivity compared to other candidate alloys for SLM which ultimately leads hot cracking, porosity and anisotropy in

microstructure [9–11]. Nonetheless, applying specific procedure for rapid cooling, post heat treatment and using ceramic particle as grain refiner and also reinforcement may produce desirable properties [9–14]. However, porosity, cellular structure, residual stress, non-equilibrium phases obtained through new manufacturing process can potentially influence on corrosion properties of AM Al alloy part [5]. Accordingly, a coherent literature and data of the corrosion is essential in the evaluation emerging AM metal parts, for which to find benefit over casting or wrought metal part.

In this study, corrosion properties of AA6061 alloy was studied in 0.5 M NaCl solution and AM manufacturing process were compared with conventional AAA6061-T6 wrought alloy.

Experimental Procedures

Corrosion performance of additive manufactured AA6061 (AM) fabricated through selective laser melting process was studied and compared with the extruded AA6061-T6 (EX). The AM contained the same composition as the EX counterpart, with the addition of 1 wt.% TiB2 powder as the grain refiner. TiB2 was added to reach similar mechanical properties of in the AM compared to the EX. AM bars with the length of 100 mm and the dimeter of 10 mm were printed vertically. Dimensions are shown in Figure 9-1.

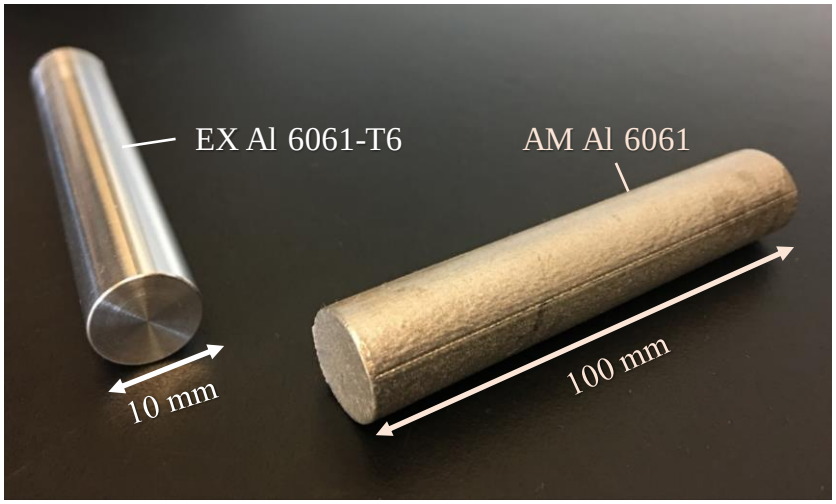

Figure 9-1. Presentation of Extruded and Additive manufactured AA6061 materials used in this study.

Each bar was cut and mounted in cold high shrinkage epoxy. In order to eliminate the influence of anisotropic texture and microstructure along the length and periphery of the bar, which is common in 3D printed objects [15-18], all samples were cut and obtained from the middle of the length. Mounted samples were polished with SiC papers, up to 1200 grade, then cleaned with distilled water and ethanol, and dried immediately with the air. The circumference of each round sample, both EX and AM, were epoxy coated, leaving a 7 mm×7 mm rectangle area as the exposed area, as shown in Figure 9-2. In order to ascertain reproducibility of results, three identical samples were prepared simultaneously and kept in desiccator.

24 h after preparation, samples were immersed in 0.5 M NaCl neutral solution. A SCE continuously recorded the open circuit potential of all samples during 9 days of exposure. EIS with ±10 mV sinusoidal perturbation over the frequency range from 10^5 Hz to 10^{-2} Hz was also conducted at the free potential of the samples in various intervals.

Linear polarization resistance (LPR) was also performed by applying a potential of -15 mV to +15 mV versus E_{ocp} with swiping rate of 0.17 mV/s and measuring the current. In all measurements, a platinum gauze was used as the counter electrode.

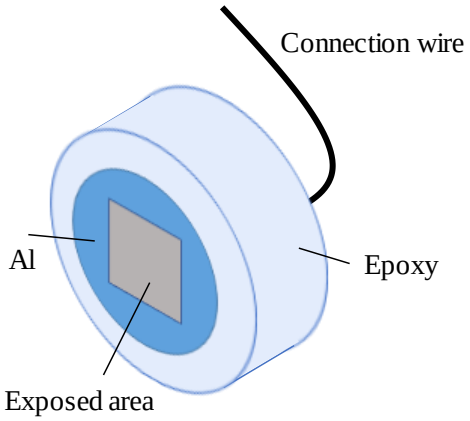

Figure 9-2. Schematic illustration of one of the samples for the electrochemical test.

All electrochemical tests were carried out on stationary electrodes at room temperature. To maintain the concertation and the pH of the solution, every day, 50% of the solution was replaced with fresh saline solution. Microstructure of samples were revealed by etching in 5 % v/v of HBF_4 in distillated water with applying 0.1 $mA.cm^{-2}$ anodic potential. Post-corrosion morphology of the corroded surfaces was examined using scanning electron microscopy after nine days immersion in 0.5 M NaCl solution.

Result and discussion

Metallographic images of AM and EX AA6061 are shown in Figure 9-3 in

different magnifications. Large porosities due to lack of fusion is apartment for AM samples. These pores mainly arise incomplete particle consolidation and/or the entrapment of gases/shrinkage during rapid solidification [8,10,19]. However, EX manufactured samples shows consolidated surfaces with uniform distribution of Al/Si/Mg second particles along whole surface due to T6 heat treatment. Dissolution path mainly started from grain boundaries which corroborates intergranular corrosion (IGC) Al-Mg-Si alloys including AA6061 [2,3,20].

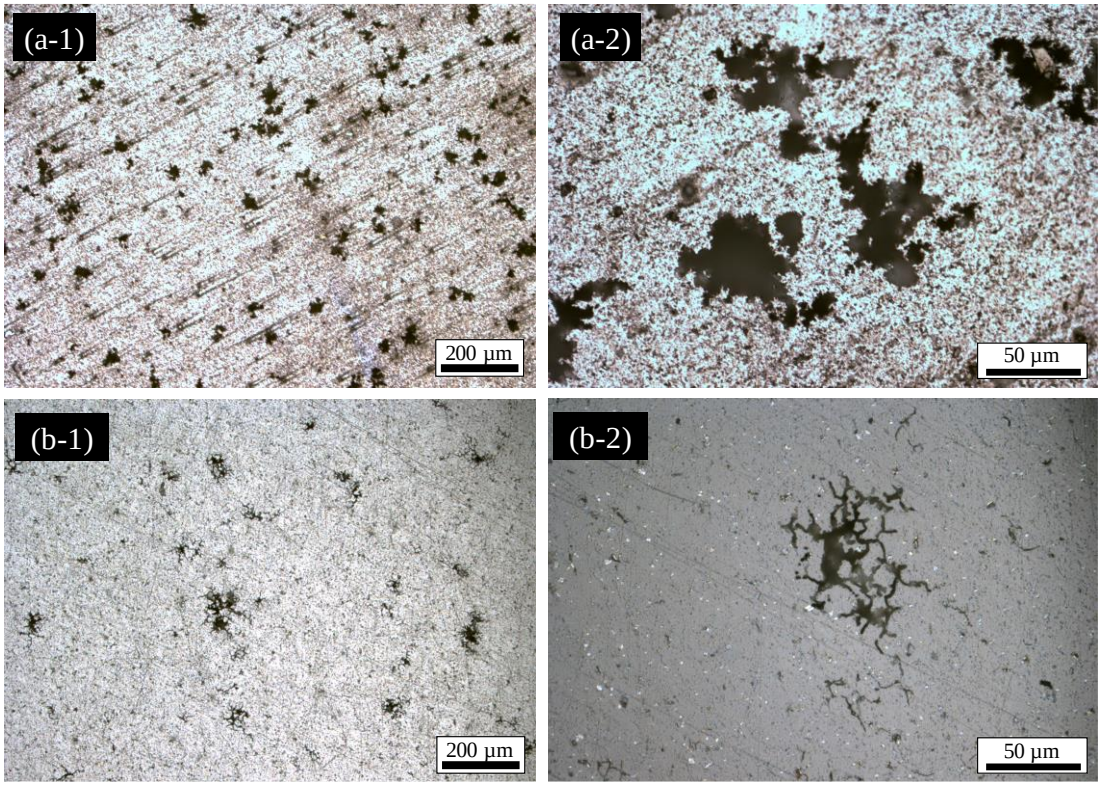

Figure 9-3. optical micrograph from microstructure of (a) AM and (b) EX AA6061 in different magnifications.

Polarization resistances, R_p, obtain from the LPR test for 9 days experiment are

shown in Figure 9-4. AM samples showed higher polarization resistance and subsequently higher corrosion resistance at early stages of exposure compared to the EX samples. However, after two days of immersion, the Rp values started to decrease, drastically, and continued to decline to the end of the immersion time. The Rp values for the AM samples was continuously less than those for the EX samples after two days of immersion in the solution. for the EX sample, the Rp values at first of day of immersion gently deceased, but in contrast to the AM samples, they started to increase after the first day, showing an enhancement in their corrosion resistance. Rapid declining the Rp at the early stage of immersion was attributed to the dissolution and water-uptake and change in stoichiometry of the air-formed Al oxide film [21].

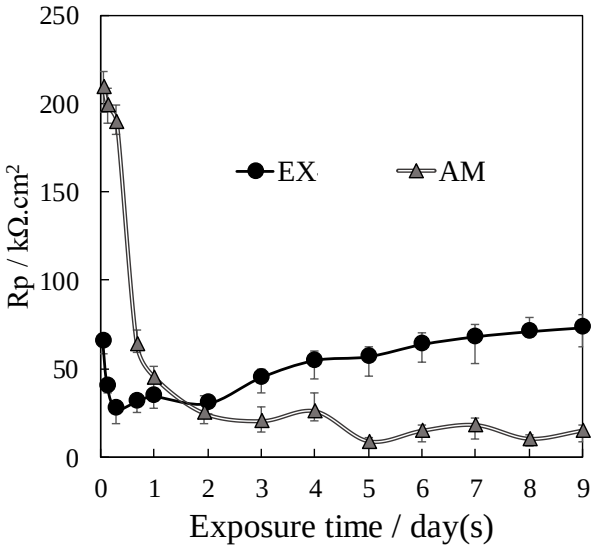

Figure 9-4. *Evaluation of polarization resistances, Rp, with respect to the immersion time for EX and AM 6061 samples.*

EIS results obtained at different immersion time for sample in each group are presented in Figure 9-5. In order to decrease noise to signal ratio and obtained realistic behavior of the surface, solution resistance was corrected for the impedance modulus and

phase angle as following [22]:

$$|Z|_{adj} = \sqrt{(Z_{re} - R_s)^2 + Z_{im}^2} \quad (1)$$

$$\varphi_{adj} = \tan^{-1}\left(\frac{-Z_{im}}{Z_{re} - R_s}\right) \quad (2)$$

Generally, results showed higher impedances for EX sample compared to the AM sample, particularly at the long-term immersion, i.e. more than two days.

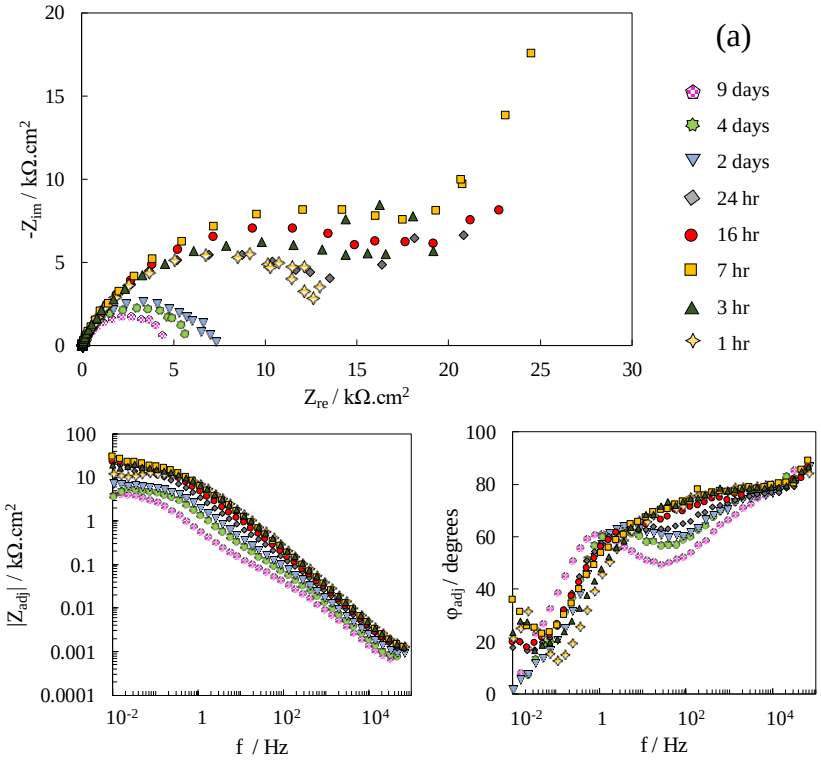

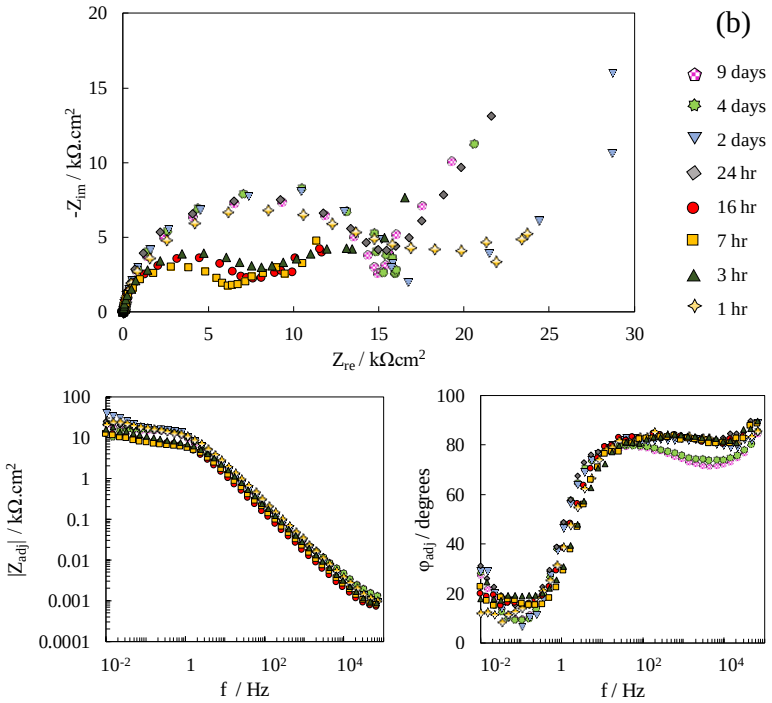

Figure 9-5.EIS results of one of (a) AM and (b) EX samples at different immersion times in 0.5 M NaCl solution.

Nyquist plots indicated depressed hierarchical semicircles and phase angle. Accordingly, different distributed time constants can be proposed for the surface reactions of the samples in 0.5 M NaCl solution. Frequency dispersion above 10^4 Hz are mainly due to the distribution of the current and the potential on the surface, which are the function of the surface geometry [23-25]. Frequencies within the ~10^4 to 10 Hz attribute to the electrochemical response of the oxide/solution, whereas the frequencies lower than 10 Hz are corresponded to the faradaic reaction which takes place at the metal/hydroxide-solution at the bottom of the porosities [26-28]. As schematically depicted in Figure 9-6. R_{ox} and Q_{ox} are resistance and dielectric properties of the oxide film on the surface. Due to observed frequency dispersion and the phase angles, constant

phase element in this range is assigned to indicate the distribution of time constants in length and along the oxide film surface due to thickens variation and water-uptake of the oxide film [21,29–33].

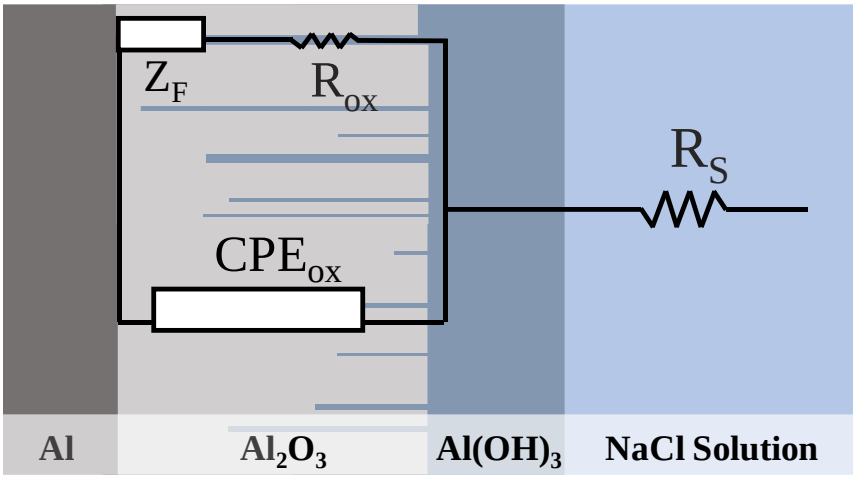

Figure 9-6. Schematic repristinating of equivalent circuit for corrosion mechanism of AA6061 in 0.5 M NaCl.

Z_F corresponds to the faradaic reaction including oxidation of the Al at the interface which contains a paralleled double layer dielectric and charge transfer resistance part. Oxidation of Al to Al^{3+} follows by this chemical reaction:

$$Al^{3+} + 3OH^- \rightarrow Al(OH)_3 \quad (3)$$

As a result, formation of adsorptive $Al(OH)_3$, at the surface, which is partially protective [34,35], causes sporadic points at low frequencies and subsequently. Nonetheless, oxide film properties are graphically comparable at frequencies more than ~10 Hz. As can be seen in Figure 9-5, phase angles for AM sample surface are very responsive to frequency changes, which implies higher contribution of charge carriers to

transport within oxide film in the applied over potential field compared to the EX sample. In contrast, oxide film for EX, is relatively independent to frequency changes, which shows less defective and diffusive dielectric properties of the oxide film to polarization in the EX sample compared to the AM sample. However, after 4 days of immersion, frequency dispersion can be seen in the oxide films in both AM and EX samples. In order to interpret the role of oxide film on the mechanism of corrosion in each immersion time, the values of the R_{ox} (Figure 9-5) were graphically obtained by extrapolation of the high frequency depressed semicircle. Subsequently, charge transfer resistance values were estimated through $R_{ct}= (R_p) -(R_{ox})$ [36]. Average values from three different measurement for each sample are listed in . For both samples, the charge transfer which governs kinetic of oxidation/reduction, had the most contribution to polarization resistance. However, this value was dependent to the accessible surface area, porosities and ohmic drop due to thickness of the oxide film. At early stage of immersion, the oxide film resistance for AM sample was close to charge transfer and increased by time of exposure. This behavior was attributed to the local dissolution of the air-formed oxide film and the formation of a porous path to the surface of the sample. The film resistance increased due to the oxidation and deposition of further Al oxide/hydroxide. However, at the same time the porosities on the oxide film increased. After certain amount of time, (i.e. 2 days) when amount of porosities became sufficiently deep to reach the substrate, the corrosion activity was accelerated, and the R_{ox} and R_{ct} declined drastically. The charge transfer originated from intrinsic properties of the substrate and its microstructure. At the early stage of corrosion, the superior corrosion performance of the AM samples was due to the

formation of a more integrated oxide film in the air compared to the EX sample, because of higher rate of oxidation of substrate in the AM sample compared to the EX sample. This observation was also shown in the polarization resistance values in Figure 9-4. However, the ultimate values of charger transfer and polarization resistance for EX sample are higher than it AM counterpart.

Table 9-1. polarization, oxide film and charge transfer resistances obtained from LPR and EIS tests.

Sample	Exposure time	Rp ($k\Omega.cm^2$)	R_{ox} ($k\Omega.cm^2$)	R_{ct} ($k\Omega.cm^2$)
AM	1 h	210.3	14.8	191.5
	3 h	199.2	19.7	179.5
	7 h	189.1	20.0	169.1
	16 h	63.5	17.1	46.4
	1 day	45.2	13.9	31.3
	2 days	24.9	7.2	17.1
	4 days	25.8	5.5	20.3
	9 days	15.2	4.5	10.7
EX	1 h	65.7	17.1	48.6
	3 h	40.1	8.2	31.9
	7 h	27.2	6.3	20.9
	16 h	31.8	7.9	23.9
	1 day	35.1	17.0	18.1
	2 days	40.7	18.1	22.6
	4 days	54.2	17.2	37.0
	9 days	76.5	16.9	59.6

Scanning electrical post corrosion microscopic observation of the AM and EX samples are shown in Figure 9-7. In large pitting zones (Figure 9-7a-1 and b-1), oxide film cracked and exfoliated for the AM sample. In contrast, this region was more integrated for the EX sample. Higher rate of direct dissolution of substrate of the AM

sample compared to the EX sample is attributed fragmentation of oxide film and lower charge transfer resistance for this sample. Similarly, in the regions were the oxide film still partially existed (Figure 9-7 a-2 and b-2), the galvanic corrosion due to the preferential dissolution in vicinity of the second phases [2,3,20], severely cracked the oxide film for the AM sample compared to the EX counterpart.

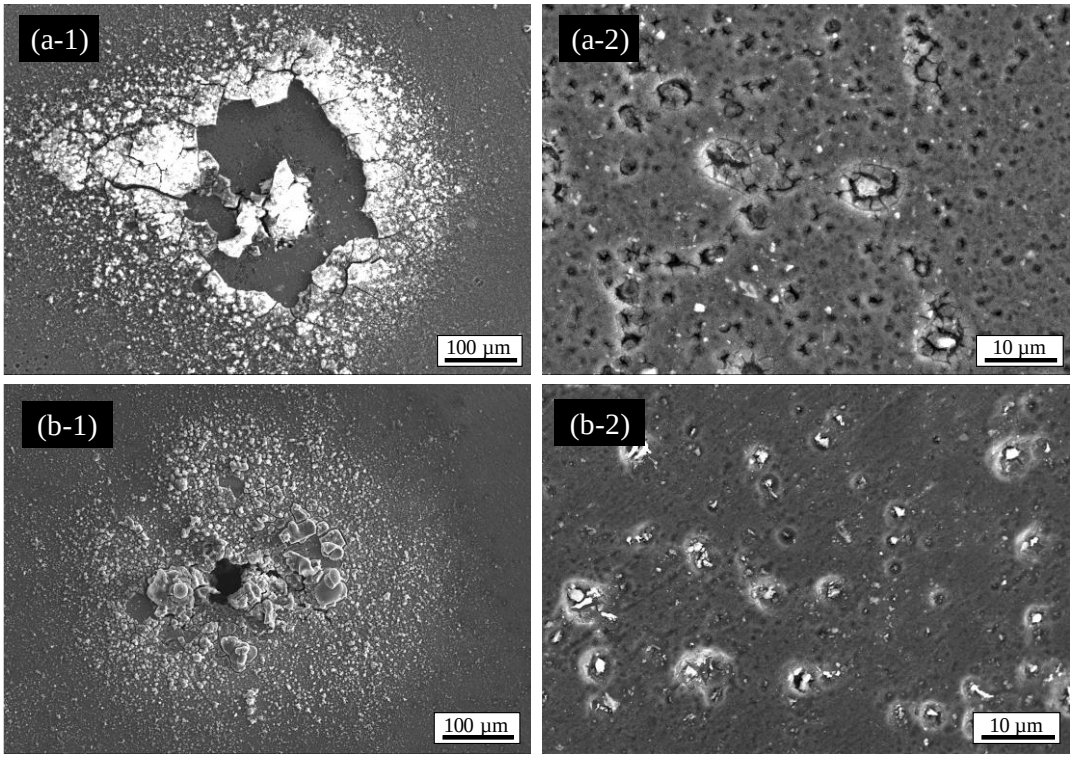

Figure 9-7. Scanning electrical micrographs of pits in the (a-1) AM and (b-1) EX samples and the morphology of the surface of the (a-2) AM and (b-2) EX samples after 9 days immersion at the OCP in 0.5 M NaCl solution.

Conclusion

Corrosion performance and the morphology of the additively manufactured Al-6061 and extruded AA6061-T6 were examined during 9 days of immersion in 0.5 M

NaCl solution. At early stage of corrosion, the AM sample showed superior performance compared to its extruded counterpart, due to the presence of the air-formed oxide film on those samples. By passing the time and contribution of the substrate to the charge transfer, corrosion resistance of the AM declined continuously, but increased gently for EX samples. Active substrate due to intrinsic defective microstructure of and higher susceptibility to galvanic corrosion because of incorporation of the grain refiners in the AM compared to the EX sample were hypothesized to be the reasons for such observations.

References

[1] H.P.G. W. B. Jepson, The Corrosion of Light Metals, John Wiley and Sons, 1967.

[2] W.J. Liang, P.A. Rometsch, L.F. Cao, N. Birbilis, General aspects related to the corrosion of 6xxx series aluminium alloys : Exploring the influence of Mg / Si ratio and Cu, Corros. Sci. 76 (2013) 119–128.

[3] Y. Zou, Q. Liu, Z. Jia, Y. Xing, L. Ding, X. Wang, The intergranular corrosion behavior of 6000-series alloys with different Mg / Si and Cu content, Appl. Surf. Sci. 405 (2017) 489–496.

[4] E.O. Olakanmi, R.F. Cochrane, K.W. Dalgarno, A review on selective laser sintering / melting (SLS / SLM) of aluminium alloy powders : Processing , microstructure , and properties, J. Prog. Mater. Sci. 74 (2015) 401–477.

[5] G. Sander, J. Tan, P. Balan, O. Gharbi, D.R. Feenstra, L. Singer, S. Thomas,

Corrosion of additively manufactured alloys : A review, (n.d.).

[6] T. Kimura, T. Nakamoto, Microstructures and mechanical properties of A356 (AlSi7Mg0 . 3) aluminum alloy fabricated by selective laser melting, JMADE. 89 (2016) 1294–1301.

[7] J.H. Martin, B.D. Yahata, J.M. Hundley, J.A. Mayer, T.A. Schaedler, T.M. Pollock, 3D printing of high-strength aluminium alloys, Nat. Publ. Gr. 549 (2017) 365–369.

[8] E. Louvis, P. Fox, C.J. Sutcliffe, Selective laser melting of aluminium components, J. Mater. Process. Tech. 211 (2011) 275–284.

[9] K.G. Prashanth, S. Scudino, H.J. Klauss, K.B. Surreddi, L. Löber, Z. Wang, A.K. Chaubey, U. Kühn, J. Eckert, Microstructure and mechanical properties of Al – 12Si produced by selective laser melting : Effect of heat treatment, Mater. Sci. Eng. A. 590 (2014) 153–160.

[10] N.T. Aboulkhair, N.M. Everitt, I. Ashcroft, C. Tuck, Reducing porosity in AlSi10Mg parts processed by selective laser melting, Addit. Manuf. 1–4 (2014) 77–86.

[11] C. Galy, E. Le Guen, E. Lacoste, C. Arvieu, Main defects observed in aluminum alloy parts produced by SLM : From causes to consequences, Addit. Manuf. 22 (2018) 165–175.

[12] M.N. Gussev, N. Sridharan, M. Norfolk, K.A. Terrani, S.S. Babu, Effect of post weld heat treatment on the 6061 aluminum alloy produced by ultrasonic additive manufacturing ☆, Mater. Sci. Eng. A. 684 (2017) 606–616.

[13] J.R. Croteau, S. Grif, M.D. Rossell, C. Leinenbach, C. Kenel, V. Jansen, D.N. Seidman, D.C. Dunand, N.Q. Vo, Microstructure and mechanical properties of Al-Mg-Zr

alloys processed by selective laser melting, Acta Mater. 153 (2018) 35–44.

[14] K.G. Prashanth, S. Scudino, J. Eckert, Defining the tensile properties of Al-12Si parts produced by selective laser melting, Acta Mater. 126 (2017) 25–35.

[15] B. Ahuja, B. Schaub, a round robin study for laser beam melting in a metal powder bed, South African J. Ind. Eng. August. 27 (2016) 30–42.

[16] G. Nicoletto, Microstructure and directional fatigue behavior of Inconel 718 produced by selective laser melting modeling of a b high pressure turbine airplane gas turbine engine, Procedia Struct. Integr. 2 (2016) 2381–2388.

[17] Y. Li, D. Gu, Parametric analysis of thermal behavior during selective laser melting additive manufacturing of aluminum alloy powder, Mater. Des. 63 (2014) 856–867.

[18] P. Mahoney, C.J. Smith, J. Donoghue, I. Todd, Additive manufacturing titanium components with isotropic or graded properties by hybrid electron beam melting / hot isostatic pressing powder processing, Nature. (2019) 1–11. doi:10.1038/s41598-019-40722-3.

[19] H. Gong, K. Rafi, H. Gu, T. Starr, B. Stucker, Analysis of defect generation in Ti – 6Al – 4V parts made using powder bed fusion additive manufacturing processes ☪, Addit. Manuf. 1–4 (2014) 87–98.

[20] T.D. Burleigh, E. Ludwiczak, R.A. Petri, Intergranular Corrosion of an Aluminum-Magnesium-Silicon-Copper Alloy, (1995) 50–55.

[21] A. Son, N. Causse, M. Musiani, M.E. Orazem, N. Pébère, B. Tribollet, V. Vivier, Determination of water uptake in organic coatings deposited on 2024 aluminium alloy : Comparison between impedance measurements and gravimetry, Prog. Org. Coatings. 112

(2017) 93–100.

[22] M.E. Orazem, N. Pébère, B. Tribollet, J.E. Soc, P. B-b, M.E. Orazem, N. Pébère, B. Tribollet, Enhanced Graphical Representation of Electrochemical Impedance Data service Enhanced Graphical Representation of Electrochemical, 153 (2006) 128–136.

[23] P. Córdoba-torres, T.J. Mesquita, R.P. Nogueira, Influence of geometry-induced current and potential distributions on the characterization of constant-phase element behavior, Electrochim. Acta. 87 (2013) 676–685.

[24] S. Cattarin, M. Musiani, B. Tribollet, V. Vivier, Impedance of passive oxide films with graded thickness : Influence of the electrode and cell geometry, 54 (2009) 6963–6970.

[25] T.T.M. Tran, B. Tribollet, E.M.M. Sutter, New insights into the cathodic dissolution of aluminium using electrochemical methods, Electrochim. Acta. 216 (2016) 58–67.

[26] H. Krawiec, V. Vignal, H. Amar, P. Peyre, Electrochim. Acta Local electrochemical impedance spectroscopy study of the influence of ageing in air and laser shock processing on the micro-electrochemical behaviour of AA2050-T8 aluminium alloy, Electrochim. Acta. 56 (2011) 9581–9587.

[27] Y. Huang, H. Shih, J. Daugherty, F. Mansfeld, Evaluation of the properties of anodized aluminum 6061 subjected to thermal cycling treatment using electrochemical impedance spectroscopy (EIS), Corros. Sci. 51 (2009) 2493–2501.

[28] Y. Huang, H. Shih, H. Huang, J. Daugherty, S. Wu, S. Ramanathan, C. Chang, F. Mansfeld, Evaluation of the corrosion resistance of anodized aluminum 6061 using electrochemical impedance spectroscopy (EIS), Corros. Sci. 50 (2008) 3569–3575.

[29] S. Cattarin, N. Comisso, M. Musiani, B. Tribollet, Electrodes Coated by Passive Oxide Films with a Thickness Profile : Modeling and Measurement of the Impedance Response, (2008) 543–549.

[30] B. Hirschorn, M.E. Orazem, B. Tribollet, V. Vivier, I. Frateur, M. Musiani, L. Interfaces, U.P.R. Cnrs, U. Pierre, Constant-Phase-Element Behavior Caused by Resistivity, (2010) 458–463.

[31] B. Hirschorn, M.E. Orazem, B. Tribollet, V. Vivier, I. Frateur, M. Musiani, Determination of effective capacitance and film thickness from constant-phase-element parameters, Electrochim. Acta. 55 (2010) 6218–6227.

[32] M. Curie, EIS Technique in Passivity Studies : Determination of the Dielectric Properties of Passive Films, Elsevier Inc., 2017. d

[33] Y.M. Chen, A.S. Nguyen, M.E. Orazem, B. Tribollet, N. Pébère, M. Musiani, V. Vivier, Identification of Resistivity Distributions in Dielectric Layers by Measurement Model Analysis of Impedance Spectroscopy, Electrochim. Acta. 219 (2016) 312–320.

[34] V. Shrivastava, G. Kumar, I.B. Singh, Heat treatment effect on the microstructure and corrosion behavior of Al-6061 alloy with influence of a -nanoalumina reinforcement in 3 . 5 % NaCl solution, J. Alloys Compd. 775 (2019) 628–638.

[35] B. Zaid, D. Saidi, A. Benzaid, S. Hadji, Effects of pH and chloride concentration on pitting corrosion of AA6061 aluminum alloy, 50 (2008) 1841–1847.

[36] U. Trdan, J. Grum, Evaluation of corrosion resistance of AA6082-T651 aluminum alloy after laser shock peening by means of cyclic polarization and ElS methods, 59 (2012) 324–333.

CHAPTER 10

Overall conclusions

Electrochemical tests for corrosion evaluation under controlled laboratory conditions should potentially estimate long-term behavior examined part under actual service environments. Appropriate simulating environment is required to obtained reliable and meaningful data for forecasting remaining lifetime or service time. As the name of corrosion implies, this phenomenon is an unstable and very sensitive thermodynamic system which changes unsteadily by changing time, environment and testing parameters.Knowing and finding possible errors in system, accurate sample preparation with relevant geometry, giving a proper time for aging the system, choosing appropriate measurement intervals, immersion time and test parameter, e.g., scan rate, are crucial to obtain reliable and reproducible data. Phases, grains, grain boundaries, texture and all the metallurgical parameters influence corroding system depending on the environment and testing parameters. It was shown that even without addition or removing of certain element to/from an alloy, corrosion performance can be changed by manufacturing, heat-treatment, or preparation procedure. Consequently, other than composition, depending on service environment and application, manufacturing/microstructural modifications should be considered in a material design and selection for a corrosion sensitive system.

Recommendations for Future Research

Although in all of the studies, surface and morphology of the corroded system were examined under scanning electron microscope, however, stoichiometry and composition of the compound and surface may vary due to exposing to air and any other condition other that actual examining environment. In-site characterization techniques can provide near real phenomenon qualitative and quantitative data rather than electrochemical data. For example, potential and work function differences between phases can be measured with Kelvin probe. Combing this measurement with scanning electrochemical microscopy (SECM) provides pictorial micro and nano scale distribution of heterogeneity along the corroding surface. Accordingly, the most vulnerable phase to corrosion can be characterized.

Global, electrochemical measurement can provide relatively accurate estimation of ion release to the environment through current measurement and Farday's law. However, in some corroding systems, which species have more than one valance, e.g Mg^{+} and Mg^{2+}, or when species release to solution without electrochemical reaction, e.g., grain dropping in intergranular corrosion of Al, electrochemical measurement may underestimate the corroding system. In this case, direct measurement of cations and anions through atomic adsorption spectroscopy (AAS) and coupled plasma mass spectroscopy (ICP) can help accurately understanding a corroding system.